Numerical Modelling of Parametric Resonance of a Heaving Point Absorber Wave Energy Converter

---

Kevin R. Tarrant

Department of Mechanical & Manufacturing Engineering

Parsons Building

Trinity College

Dublin 2

Ireland

March 2015

A thesis submitted to the University of Dublin in partial fulfillment of the requirements for the degree of Ph.D.

Declaration

I declare that this thesis has not been submitted as an exercise for a degree at this or any other university and it is entirely my own work.

I agree to deposit this thesis in the University's open access institutional repository or allow the library to do so on my behalf, subject to Irish Copyright Legislation and Trinity College Library conditions of use and acknowledgement.

Kevin R. Tarrant, March 2015

Abstract

It is known that free floating objects such as a wave energy converter may experience a phenomenon known as parametric resonance when the incident wave has a frequency approximately twice the roll or pitch natural frequency. This can result in large amplitude motion in the roll and/or pitch modes. While classic linear theory has proven sufficient for describing small motions due to small amplitude waves, a point absorber wave energy converter is often designed to operate in resonant conditions, and therefore, exhibits significant nonlinear responses. In this study, a time domain nonlinear numerical model is further developed for describing the dynamic stability of point absorbers. The pressure of the incident wave is integrated over the instantaneous wetted surface to obtain the nonlinear Froude-Krylov excitation forces and the nonlinear hydrostatic restoring forces, while first order diffraction-radiation forces are computed by a linear potential flow formulation. A numerical benchmark study for the simulation of parametric resonance of a specific wave energy converter—the Wavebob—has been implemented and validated against experimental results. The implemented model has shown good accuracy in reproducing both the onset and steady state response of parametric resonance, both in the vertical and horizontal planes. Limits of stability in the roll and pitch modes were numerically computed for a range of power-take-off (PTO) damping coefficients in regular waves. The appearance of the unstable areas resembles the first Mathieu type unstable zone and reveal that the roll and pitch modes become more unstable as the PTO damping is increased. Numerical simulations in irregular long crested waves, where the roll is not directly excited, show that there is always some degree of parametric roll response due to the wave spectrum containing energy at twice the roll natural frequency.

Acknowledgments

There are several people I would like to thank, who, in some way or another, have contributed to the work which was carried out in presenting this thesis.

Firstly, I would like to sincerely thank my supervisor Dr. Craig Meskell whose help and guidance over the years has been invaluable, not just from an educational standpoint but also in assisting me to seek out that faint light at the end of the tunnel.

Thank you to everyone involved in the Wavebob team at the time, in particular, Thomas Soulard, Elva Bannon, Jochem Weber, Carlos Villegas, Peter Arnold, Chris Signorelli, Andrew Parish, Joe Murtagh and Cian Murtagh. The help and support I received during my time working with these people paved the way for much of the work in this thesis.

I would also like to express my gratitude to Professor Claudio Rodríguez for sharing his expertise and never failing to reply to my questions on all things hydrodynamics and parametric resonance related.

A special thanks to William Dick whose vision to design a unique device that would float in the ocean, and transform the up and down motion of sea waves into electricity brought about the creation of the Wavebob.

To my friends, housemates, Bob Dylan and fellow Ph.D. colleagues for providing me with the well needed distractions throughout the years.

Finally, I would like to thank my parents. Words cannot express the encouragement and support they have provided me with during the years.

Contents

List of Figures

List of Tables

Nomenclature

B_{PTO}	PTO damping coefficient
C_d	Drag coefficient
E_k	Kinetic energy in a regular wave
E_p	Potential energy in a regular wave
$\mathbf{F}$	General force vector
$\mathbf{F}_{FK}$	Linear Froude-Krylov excitation force
$\mathbf{F}_{FK_d}$	Nonlinear Froude-Krylov dynamic excitation force
$\mathbf{F}_{FK_s}$	Nonlinear Froude-Krylov hydrostatic restoring force
$\mathbf{F}_{PTO}$	PTO force
$\mathbf{F}_d$	Linear diffraction excitation force
$\mathbf{F}_e$	Total linear wave excitation force
$\mathbf{F}_{hs}$	Linear hydrostatic restoring force
$\mathbf{F}_m$	Component of total hydrostatic force due to the mass of the body
$\mathbf{F}_{moor}$	Linear mooring force
$\mathbf{F}_r$	Linear radiation force
$\mathbf{F}_w$	Inertia force of a body
GM_L	Longitudinal metacentric height
GM_T	Transverse metacentric height
H	Wave height
H_s	Significant wave height
H/λ	Wave steepness
I_{jk}	Moments of inertia about axis j when rotated about axis k
K_{FK_j}	Froude-Krylov excitation force impulse response function in mode j
K_{d_j}	Diffraction excitation force impulse response function in mode j

$K_{r_{jk}}$	Linear radiation force impulse response function in mode j due to an oscillation in mode k
M	Inertia matrix
P	Power in a wave
S_b	Mean submerged surface of a body
$S_b(t)$	Time varying submerged surface of a body
S_w	Waterplane area of a body
$S_{J\zeta}(\omega)$	Wave amplitude spectral ordinate for JONSWAP spectrum
$S_\alpha(\omega)$	Wave slope spectral ordinate
$S_\zeta(\omega)$	Wave amplitude spectral ordinate
T	Wave period
T_p	Wave peak period
W_{jk}	Waterplane area moments of inertia with relation to horizontal x and y axes $(j, k = 1, 2)$
$Z(\omega)$	Radiation impedance matrix
$a_{(j\ k)}$	Infinite frequency added mass in mode j due to an oscillation in mode k
$a(\infty)$	Infinite frequency added mass matrix
$a(\omega)$	Frequency dependent added mass coefficients
$b_{(j\ k)}$	Radiation damping in mode j due to an oscillation in mode k
b_w	Width of a wave crest
$b(\omega)$	Frequency dependent radiation damping coefficients
$c_{(j\ k)}$	Element jk of matrix of hydrostatic coefficients
$\mathbf{f}$	External forces per unit volume
$\mathbf{g}$	Acceleration due to gravity
h	Water depth
i	$\sqrt{-1}$
k	Wave number
k_{moor}	Linear mooring stiffness coefficient
m	Mass
m_o	Variance of an irregular wave
m_t	Combined mass of torus and FNT

$\mathbf{n}$	Outward unit normal vector of a point on a solid boundary
p	Total fluid pressure at a point under a regular wave
p_d	Dynamic pressure
p_o	Atmospheric pressure
p_s	Hydrostatic pressure
$\mathbf{r}_g^k$	Position vector of centre of gravity in a general coordinate frame k
$\mathbf{r}_m^k$	Position vector of point of attachment of mooring line to the body in a general coordinate frame k
t	Time
$\mathbf{u}(\mathbf{x}, t)$	Fluid velocity at a fixed point in space with coordinates $\mathbf{x} = (x_1, x_2, x_3)$
(u_1, u_2, u_3)	Components of fluid particle velocity vector
$\mathbf{v}$	Velocity vector of a point on a solid boundary
v_n	Outward normal velocity of a point on a solid boundary
x	Wave propagation direction coordinate
(x_b, y_b, z_b)	Coordinates of centre of buoyancy of a body
(x_g, y_g, z_g)	Coordinates of centre of gravity of a body
y	Horizontal coordinate perpendicular to the wave propagation
z	Vertical direction coordinate; zero at undisturbed water surface, positive to the outside of the fluid
Δl	Change in length of mooring line
θ	Phase angle
Φ	Total velocity potential (incident + radiation + diffraction potential)
α	Wave slope: the gradient of the surface profile
δ_{jk}	Kronecker delta function
ζ	Damping ratio
ζ_o	Wave amplitude
ζ_w	Instantaneous depression of the water surface above the mean water level
λ	Wavelength
ξ_1	Surge motion
ξ_2	Sway motion
ξ_3	Heave motion

ξ_4	Roll angular motion
ξ_5	Pitch angular motion
ξ_6	Yaw angular motion
ξ_{4_o}	Initial roll angle
ξ_{5_o}	Initial pitch angle
$(\xi_3 - \xi_9)$	Relative heave displacement
$\xi_{j_{rms}}$	Root mean square of displacement in degree of freedom j
ρ	Density of water
ϕ	General velocity potential
ϕ_d	Diffraction velocity potential
ϕ_i	Incident wave velocity potential
ϕ_r	Radiation velocity potential
ω	Angular frequency of vibration
ω_e	Wave excitation frequency
ω_n	Natural frequency of vibration
ω_p	Peak angular frequency
ω_4	Roll natural frequency
ω_5	Pitch natural frequency
φ	Complex coefficient of proportionality
$\forall$	Displacement volume of a body

Abbreviations

BEM	Boundary element methods
$CA-OE$	Coordinated Action on Ocean Energy
CFD	Computational fluid dynamics
EC	European Commission
ECN	École Centrale de Nantes
EU	European Union
FNT	Float-neck-tank
FK	Froude-Krylov

IEA	International Energy Agency
$IEA-OES$	Implementing Agreement on Ocean Energy
IRF	Impulse Response Function
$JONSWAP$	Joint North Sea Wave Project
OB	Oscillating body
OTD	Overtopping device
OWC	Oscillating water column
PTO	Power take off
$RANS$	Reynolds averaged Navier-Stokes
RAO	Response amplitude operator
SWL	Still water level
WEC	Wave energy converter
$WERATLAS$	European Wave Energy Atlas

Subscripts

A	Associated with the torus
B	Associated with the FNT

Operators

$\mathcal{F}$	Fourier transform
∇	Gradient operator
$*$	Convolution operator
$\dot{x}$	First derivative of x
$\ddot{x}$	Second derivative of x
$\hat{x}$	Complex amplitude of x
x^T	Transpose of x
$\Re$	Real part of a complex number
$\mathbb{R}$	Set of real numbers

Chapter 1

Introduction

The availability of inexpensive energy in useful forms has been one of the most important and contentious issues for mankind throughout history. Energy resources have become a decisive element in defining the politics, economics and diplomacy of countries and is an issue which has a profound impact on society in several aspects. The world demand for energy is expected to increase by as much as 41% between 2012 and 2035 [1], with population and economic growth being the main drivers of global energy demand. The result of this extraordinary demand for energy is that present methods of energy production may not be able to meet future world requirements. To date, most primary energy consumption has been provided by fossil fuels. Yet fossil fuels are finite resources and they can also irreparably harm the environment. Action is needed to limit carbon dioxide and other greenhouse gases emitted through fossil fuel use. Greenhouse gases are warming the Earth and causing changes in the global climate with increasingly severe human, economic and environmental impacts. As the source of more than two thirds of global greenhouse gas emissions [2], the energy sector is crucial to tackling climate change.
In 2009, a climate and energy package was adopted in the European Union (EU), and became a binding legislation known as the 20-20-20 targets [3]. Some of the targets outlined to tackle climate change by 2020 include:

- a reduction in EU greenhouse gas emissions of at least 20% below 1990 levels;
- at least 20% of gross energy consumption to come from renewable energy;
- a saving of 20% in energy consumption through efficiency.

A further incentive for certain regions in the world to develop renewable energy applica-

tions is their dependance on imports of fossil fuels from other countries. The EU imported 53.8% of it's energy in 2011 [4]. In the same year, Ireland relied upon imported energy to satisfy 88.9% of it's total energy requirement [4].

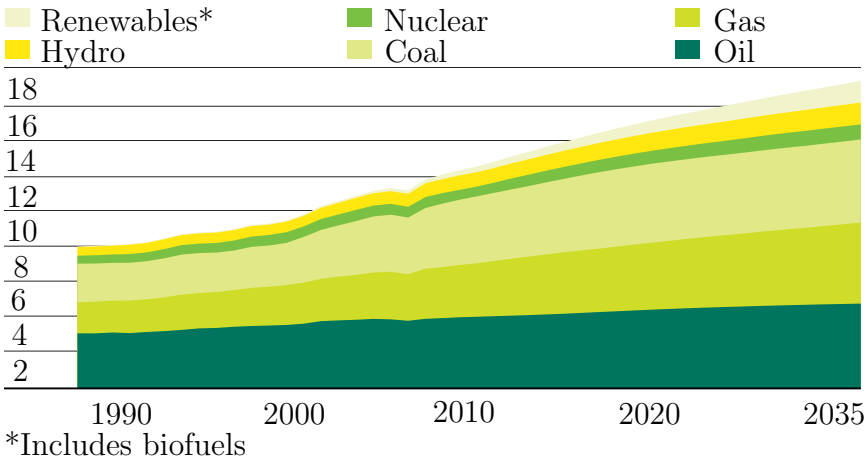

Figure 1.1: Global energy consumption by fuel (billion tonnes of oil equivalent) [5]

These demands have shifted opinion towards the imperative of addressing climate change by developing sustainable energy resources. Renewable energy comes from energy sources that are continuously replenished by nature. The main sources of renewable energy are the wind, the sun (direct solar energy), moving water (hydropower, wave and tidal energy), heat below the surface of the earth (geothermal energy) and biomass (wood, biodegradable waste and energy crops). While individually each can provide only a small percentage of the total requirements, together their output can supply considerable energy. As can be seen in Fig. 1.1, it is predicted that renewables are to be the fastest growing class of energy fuel, growing at an average of 6.4% a year on a global basis between 2012 and 2035 [1].

One renewable energy source, which has remained relatively untapped to date, is ocean wave energy. To reach the ambitious renewable energy targets set by the EU, ocean energy could make a valuable contribution to reach these goals. However, ocean wave energy is still a relatively immature technology when compared to other renewable energy sources, and still faces several engineering challenges, including; high costs, survivability, and the issue of excessive oscillations due to a phenomenon known as parametric resonance in the case of point absorber type wave energy converters.

1.1 Objectives & Overview

The work described in this study will concentrate on a number of objectives:

- To further develop a seven degree of freedom time domain nonlinear numerical model for simulating the dynamic behaviour of the Wavebob two body heaving point absorber. The goal is for the numerical model to be able to predict parametric resonance which is a nonlinear phenomenon whereby the point absorber reaches large roll and pitch angles when the incident wave has a frequency approximately twice the roll and/or pitch natural frequency.

- To implement the numerical model and to compare the results with experimental tank test data of a 1-17th scale model of the Wavebob.

- To investigate the phenomenon of parametric resonance for the Wavebob in regular and irregular waves, and to see what influence the relative heave motion and power take off (PTO) damping coefficient have on parametric resonance.

- To formulate limits of stability for the roll and pitch modes in regular waves based on numerical simulations.

The thesis is organised as follows:
Chapter two reviews the state of the art in wave energy conversion and wave energy conversion technologies. A review on the various methods of numerical modelling of wave energy converters in the literature is provided, along with a mathematical explanation of parametric resonance and the differences it has with normal resonance.
Chapter three provides a procedure for the mathematical modelling of the fluid structure interactions of floating bodies in waves. The final part of the chapter focuses on the specific theory used for the numerical modelling of the 7 degree of freedom model used in this study.
Chapter four describes the geometric and system parameters of the 1-17th scale Wavebob model.
Chapter five details the steps involved in implementing the nonlinear numerical model and also provides validation of the algorithms used in the numerical model.

Chapter six presents the results from the numerical simulations in regular waves, with comparisons between numerical and experimental results also being provided. This chapter also presents a detailed analysis of the nonlinear behaviour of parametric resonance, and determines the influence of PTO damping and relative heave on the occurrence of parametric motion.

Chapter seven investigates the response of the the numerical model in irregular long crested waves.

Chapter eight summarises the various observations of the study and presents the conclusions drawn. Possible opportunities to carry out further work are also discussed.

Chapter 2

Literature review

2.1 The wave energy resource

Wave energy is derived from the winds as they blow across the oceans, and as with the wind, it varies considerably on various temporal and spatial scales. The assessment of the wave energy resource is therefore an essential aspect for assessing the viability of wave energy projects, and determining the likely cost of energy at a given location. In Europe, one of the databases dedicated specifically to the wave climate as a resource for energy extraction is the *European Wave Energy Resource Atlas* (WERATLAS) [6], which has been funded by the European Commission. It characterises wave climate and wave energy statistics at various locations off the Atlantic and Mediterranean coasts of Europe, based on data from numerical wind-wave modelling, and in-situ and satellite altimeter measurements.

As is the case for most forms of renewables, wave energy is unevenly distributed over the globe. A map showing the global distribution of annual average wave energy transport is shown in Fig. 2.1. The resource is strongest in the regions between 30° and 60° on both the northern and southern hemispheres, induced by the prevailing western winds (westerlies) blowing in these regions. Particularly high resources are located along the Western European coast, off the coasts of Canada and the USA, and the southern coasts of Australia and South America.

Wave energy is considered to be the most concentrated form of renewable energy, with energy fluxes of 4-11 kW/m width of incoming wave along the European Mediterranean coast, 25 kW/m off the southern Atlantic coast of Europe, and up to 75 kW/m off the

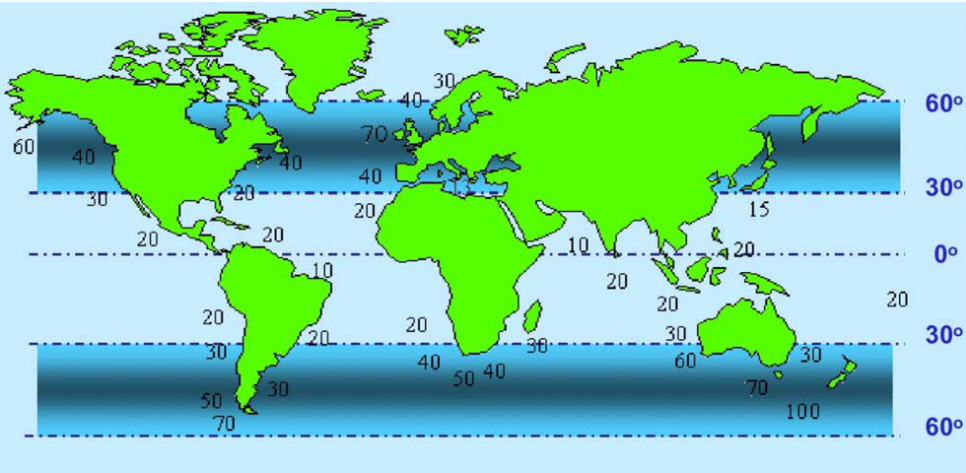

Figure 2.1: Approximate global distribution of time-averaged wave power given as kW/m of wave crest length [7]

coast of Ireland and Scotland. Resource studies assign available wave power resources of around 290 GW for the area of the north-eastern Atlantic (including the North Sea) and around 30 GW for the Mediterranean [8].

2.2 Sea states and their energy

Ocean wave energy can be considered as a concentrated form of solar energy, since the waves are derived from winds, which in turn are generated by the differential solar heating of the Earth. Wind energy is imparted to the sea surface through shear stresses and pressure fluctuations, resulting in wind waves which are disturbances in the ocean that transmit energy from one place to another. As the wind gains strength, the ocean surface develops gradually, from flat and smooth, through growing levels of roughness. First, ripples form, which then gradually build up to form larger waves. Once created, wind waves can travel thousands of kilometres with little energy losses, unless they encounter head winds. The amount of energy flux between the wind and ocean surface, and hence the size of the resulting waves, depends on the wind speed, wind duration, and the distance over which the wind is blowing—called the fetch.

Waves are energy in motion, and they transmit energy by means of cyclic movement through matter. The medium itself (the water) does not actually travel in the direction of the energy that is passing through it. The water particles simply oscillate in a circular

orbital motion, transmitting energy from one particle to another, as rollers in a conveyor belt do—they rotate in order to move the belt forward, but they themselves do not move forward in the process.

The waves which influence the behaviour of wave energy converters (WECs) are generally irregular and more or less random in nature. No two waves have exactly the same height and they travel across the surface at different speeds and in different directions. However, it is beneficial to discuss the characteristics of WECs subject to ideal regular waves. Such waves never occur in the real ocean environment—although they can be produced accurately in laboratory towing tanks—and form the basis of the initial design and development stage of a WEC. Of equal importance is the fact that the theory of irregular waves is based on the assumption that they can be represented by superposition of a suitable assembly of regular waves. The energy associated with a train of regular waves includes equal contributions from potential energy E_p and kinetic energy E_k. From linear wave theory, this is expressed as

$$E = E_p + E_k = \frac{\rho g H^2 \lambda b_w}{8} \tag{2.1}$$

where b_w is the width of the wave crest, ρ is the density of water, λ is the wavelength and g is the gravitational constant. The potential energy is exhibited by the wave height H, whereas the kinetic energy is dependent on the motions of the particles. The energy calculated is associated with the total fluid motion and this relates to water that (averaged over time) remains at the same location. An expression relevant for the energy that is carried forward (transfer of energy) is the energy flux, or wave power. For deep regular waves, this is written as:

$$P = \frac{\rho g^2 H^2 T}{64\pi} \tag{2.2}$$

The power contained in a wave is therefore proportional to its period, T, and the square of its wave height, H.

As alluded to above, a real sea state is a superposition of multiple, single frequency sinusoidal components, and can therefore be described by a wave energy spectrum which describes how energy is distributed over a range of frequencies. In terms of wave height, the significant wave height H_s is used which is the mean value of the highest one-third waves of many measurements. The most commonly used wave spectra to describe random

seas are the JONSWAP and Bretschneider spectrum. A comparison of these two spectra is given in Fig. 2.2. These wave spectra are widely used to analyse the response of WECs under random sea excitation during numerical and physical testing. This will be discussed further in Chapter 7.

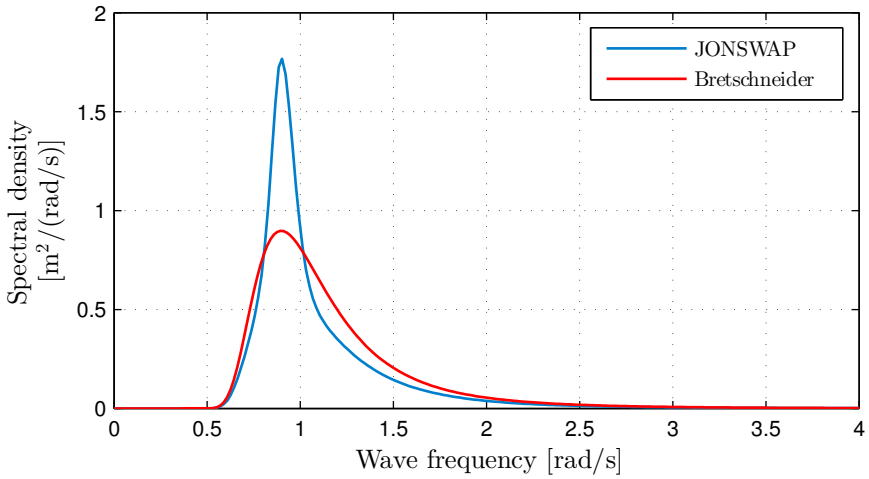

Figure 2.2: Comparison of JONSWAP and Bretschneider spectrum ($H_s = 3m$, $T_p = 7s$)

2.3 History of wave energy conversion

The fascination for capturing ocean energy can be traced back as far as the 18th century, when the first patent for the design of a wave machine to capture ocean energy was granted to Monsieur Girard and his son in 1799. Their idea was to use the heave motion of a docked ship to rock long wooden beams, acting as levers, to drive pumps, saws and other machinery. In the late 1940s, the Japanese wave power pioneer Yoshio Masuda started to test and develop a wide range of wave energy devices. He developed a navigation buoy powered by wave energy, equipped with an air turbine, which later promoted the construction of a floating barge, named Kaimei, which housed several oscillating water columns (OWC) equipped with different types of air turbines. Leishman & Scobie [9] documented a comprehensive study of the development of wave powered devices from the first British patent in 1855, up to 1973, when there were already 340 patents.

The oil crises of the 1970s highlighted the vulnerability in the world's energy utilisation pattern, and provided the impetus for modern research into harnessing energy from waves. Stephen Salter—one of the pioneers of modern wave energy—was part of the Wave Power

Group at the University of Edinburgh which was founded in 1974. Salter published a paper in 1974 in the journal *Nature* [10], which brought the idea of wave energy extraction to the attention of the scientific community. Large government funded research and development (R&D) programmes were started during the the late 1970s in the UK, Sweden, Norway, Denmark and Ireland which aimed at developing industrially exploitable wave power conversion technologies.

During the early 1980s, when the petroleum price declined, wave energy funding was drastically reduced. More recently, due to the growing awareness of forthcoming shortages of fossil fuels, coupled with the pressure to honour greenhouse gas emission limits (e.g. Kyoto protocol & EU Emissions Trading System [11]), much attention has reverted back to wave energy R&D. This progression has been boosted by the involvement of the European Commission (EC), who have contributed greatly in raising the profile of wave energy as an economically viable green energy source. The EC has promoted collaboration between leading organisations and institutes via the formation of the European Thematic Network [12] and a Coordinated Action in Ocean Energy (CA-OE). The Thematic Network aims to raise the profile and level of expertise of the wave energy sector, while the members of the CA-OE share a common interest in the mutual benefit of cooperation, promotion and exchange of experience within the field.

The Implementing Agreement on Ocean Energy Systems (IEA-OES) is an intergovernmental collaboration between 19 countries which was initiated in 2001. The IEA-OES operates under a framework established by the International Energy Agency (IEA). The role of the IEA-OES is to provide an authoritative international voice for ocean energy, and to accelerate the viability, uptake, and acceptance of ocean energy systems. This is achieved by connecting organisations within the ocean energy sector, educating people globally on the nature of ocean energy systems, and to inspire governments, corporations and individuals to become involved with the development of ocean energy systems. The IEA-OES Annual Report [13] contains a survey of the ongoing activities in wave energy worldwide.

EU funded programmes have provided over €80 million since 2002 to support R&D technologies that harness energy from the seas and oceans [14]. It has made contributions towards developing particular technologies, such as shoreline OWCs at Pico in

the Azores [15], the Wave Dragon [7], and the Seawave Slot-Cone Generator [16]. The EC funded MARINET project provides access to infrastructures and test facilities across Europe, with the aim of accelerating the development and commercial deployment of the technologies.

2.4 Wave energy converter technologies

In the last few years, considerable efforts and advances have been made worldwide in exploiting the energy of ocean waves with positive steps towards commercial viability being taken. The more advanced device developers, such as Pelamis and Aquamarine Power's Oyster, are now progressing beyond single unit demonstration devices and are proceeding to array development and multi-megawatt projects. The backing of major utility companies is now manifesting itself through partnerships within the development process, unlocking further investment and, in some cases, international co-operation. An overview of wave energy converter technologies is provided in the literature by Drew et al. [17]

Using waves as a source of renewable energy offers significant advantages over other methods of energy generation. Wave energy has the highest energy density among renewable energy sources, has high availability and has good predictability. However, it is important to understand the difficulties which wave power developments face. Due to the nature of sea waves, a WEC has to operate under a wide range of excitation frequencies and amplitudes. It also has to be capable of withstanding extreme weather conditions. There are also challenges in efficiently coupling the irregular, low frequency motion of sea waves with an electrical generator. From an economic point of view, there is an inherent compromise between cost and survivability, as a larger device may be more likely to survive the harsh ocean environment, but would be more costly. The main disadvantage of wave power is its variability. There is great variation in power levels with the passage of each wave, which poses problems when connecting to the national grid, as some sort of storage system is required to balance energy requirements during peak daily times. Nevertheless, several configurations of WECs have been proposed and tested over the years, varying greatly in both design and technology.

The phenomenon of primary conversion of wave energy can be described by a wave force acting on a moveable absorbing member (e.g a floating buoy or oscillating water), which acts against a fixed point (land or sea-based structure), or against another moveable, but force-resisting structure. The wave force results in oscillatory motion of the absorbing member, and the product of the wave force and the corresponding motion represents absorbed (primary converted) wave energy. A secondary energy conversion is usually obtained by means of hydraulic machinery, or some sort of a turbine, which delivers energy through a rotating shaft. An electric generator is then used to convert the mechanical energy into electrical energy. The fundamental device design of a WEC will be dependent on the location of the device and the intended resource characteristics. There are many ways of classifying the different types of WECs, for instance, according the their location or principles of operation.

Classification according to installation site:

Shoreline devices:

These devices lie on the bottom or on very shallow waters ($<$ 10m), commonly integrated into coastal structures, such as breakwaters of rocky cliffs, which has the advantage of easier maintenance and installation. In addition, these devices do not require deep water moorings or long lengths of underwater electric cable due to their close proximity to the utility network. Shoreline devices have a reduced likelihood of being damaged in storm conditions due to the attenuation of waves as they travel through shallow water. The less energetic wave climate (typically 20 kW/m) at the shoreline can be partly compensated by natural energy concentrated locations ("hot spots"), due to refraction or reflection. By nature of their location, the development of this class of devices for mass production may be hindered due to their impact on coastal landscapes and environments.

Nearshore devices:

Near shore devices are deployed at moderate water depths (10-20m), at distances up to 500 m from the shore. With many of the advantages of shoreline devices, they exploit higher power wave resources. Due to the intermediate water depths in this region, the WECs that occupy it tend to be mounted on the seabed, allowing for full exploitation

of the wave—a capability that is lost to floating devices. Other advantages of nearshore devices are that the largest waves are limited in height, owing to wave breaking, and there is also less directional spread of longer and medium period waves than that in deep water. Like shoreline devices, a disadvantage is that shallow water leads to waves with reduced power, limiting the harvesting potential. In addition, in tidal regions, the mean water level can vary by several metres twice a day, meaning that the bottom mounted devices may be exposed above the waterline during this time which is not their intended purpose.

Offshore devices:
Offshore devices are usually floating or submerged devices in deep waters (> 50m), moored to the sea floor. This class of device exploits the more powerful wave regimes available in deep water before energy dissipation mechanisms have had a significant effect. Reliability and survivability are the biggest challenges these kinds of devices are facing, due to the extreme harshness of the sea environment. Mooring systems must be designed carefully to prevent the device from drifting and/or avoid overturning, while at the same time not to significantly change the frequency response of the device. Offshore devices require long electrical cables to connect to the utility network on land, and are likely to occur as large multi-device wave power plants (wave farms).

Classification according to principle of operation:
Oscillating Water Column:
The oscillating water column (OWC) comprises a partially submerged concrete or steel structure, open below the water surface, inside which air is trapped above the water free surface, as shown in Fig. 2.3. The oscillating motion of the free surface, produced by the incident waves through an underwater opening, alternatively pressurises and depressurises the air inside the structure, generating a reciprocating flow through a turbine that drives an electrical generator. Because of this bidirectional air flow, the turbine must be designed to rotate in only one direction, independent of the direction of air flow. The axial-flow Wells turbine is generally used for this purpose. OWC devices can be contained within a fixed structure at the shoreline, located near shore as a bottom mounted structure, or can be moored in deeper water as a floating system.

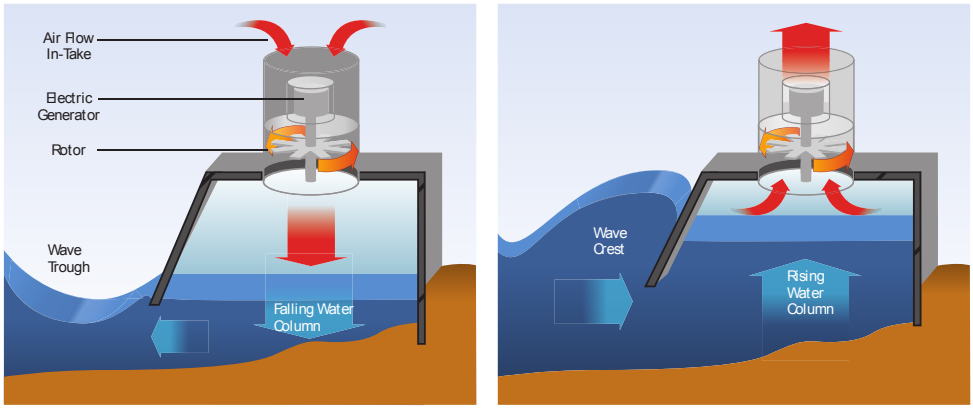

Figure 2.3: Oscillating water column device [18]

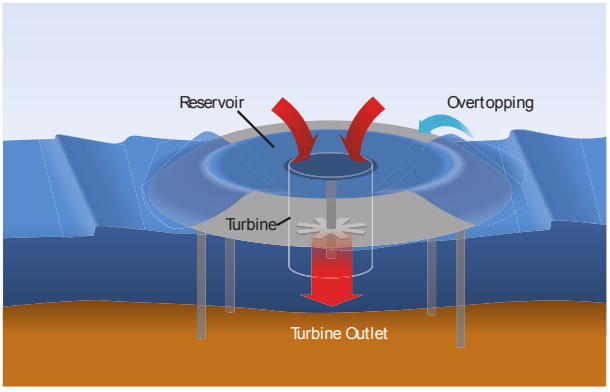

Figure 2.4: Overtopping device [18]

Overtopping Device:

An overtopping device (OTD) works by physically capturing the water from waves. The design of the device is such that it causes waves to break across the device, by over spilling into a reservoir, where it is stored at a level higher than the average free surface level of the surrounding sea. The potential energy of the stored water is converted into useful energy through a low-head hydraulic turbine. The overtopping WEC can be placed on the shoreline or nearshore, but are more commonly placed at a nearshore location. An example of an overtopping device is shown in Fig. 2.4. The OTD may be slack moored or fixed to the ocean bottom, and needs to be able to adjust to different wave heights.

Oscillating Body Systems:

The oscillating body (OB) wave energy conversion devices use the incident wave motion to induce relative oscillatory motion between bodies; these motions are then used to drive the power take off (PTO) system. They may occupy a variety of ocean depths ranging from shallow to very deep, depending on the WEC design and the type of mooring used. The simplest OB device is the single body heaving buoy, which reacts against a fixed frame of reference (the sea bottom or a bottom-fixed structure). An OB reacting against the seabed is shown in Fig. 2.5. This concept may raise difficulties due to the distance between the free surface and the sea bottom. More commonly, axi-symmetric surface flotation devices (buoys) use buoyant forces to induce heaving motion relative to a secondary body, in which the energy is converted from the relative motion between the two bodies oscillating with different phases. Generically, these devices are referred to as "point absorbers", because they are non-directional, and they can receive incoming waves from any incident angle.

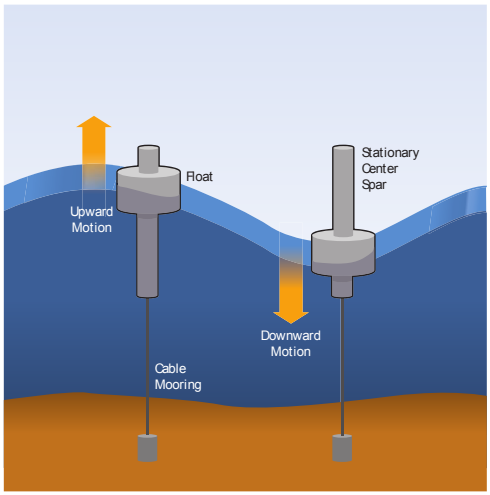

Figure 2.5: Oscillating body system [18]

There are other floating oscillating body systems in which the energy conversion is based on relative rotation (mostly pitch) rather than translation. This is the case of the nodding Duck (created by Stephen Salter [10]) which is a cam-like floater oscillating in pitch. Another variation of floating surface device uses angularly articulating (pitching) buoyant cylinders linked together, which lie parallel to the predominant wave direction (attenuators). The wave induced, alternating rotational motion of the joints can be resisted by

hydraulic rams, which pump high pressure hydraulic fluid through a motor, or by a direct drive PTO system, to generate electricity.

Some OB devices are fully submerged, and rely on the oscillating hydrodynamic pressure caused by passing waves to extract the wave energy. They consist of a seabed fixed air-filled cylindrical chamber with a moveable upper cylinder. As a wave crest passes over the device, the water pressure above the device compresses the air within the cylinder, moving the upper cylinder down. As a wave trough passes over, the water pressure on the device reduces and the upper cylinder rises. This motion is resisted by a linear electrical generator, with the interior air pressure acting as a spring.

Lastly, there are bottom-hinged, oscillating wave surge converters, which are positioned with their main axes perpendicular to the wave direction (terminators). As waves approach more shallow water, the circular movement of water particles becomes more elliptic, and water movement closer to the seabed becomes a back and forth motion. Oscillating wave surge converters use this oscillating surge motion to extract energy. They are generally fixed to the seabed relatively close to shore, in shallow to moderate water depths.

The devices outlined above are based on a whole range of different technologies. Even within the category of point absorbers, several ideas and concepts have been launched, involving a variety of engineering disciplines. Hence, wave energy research is spread over many different areas of expertise. This study focuses on some specific hydrodynamic design aspects, and attempts to highlight some important phenomena that need to be taken into account in the design process of a specific type of WEC—a heaving point absorber system.

2.5 Point absorbers

According to Falnes and Budal [19], a point absorber is a wave power absorber whose horizontal extension is very small compared to the wavelength. Such a device may oscillate with amplitudes significantly larger than the amplitude of the incident wave, for instance by resonant tuning, that is, if the natural frequency of the point absorber is equal to the frequency of the wave. A point absorber exposed to an ocean wave is forced to oscillate, and therefore creates its own wave which radiates away from the device. The resulting combined wave has a smaller amplitude, and hence smaller power content, than the incident wave. According to the principle of conservation of energy, the reduction of the amplitude must be equal to the energy absorbed by the point absorber. An oscillating system therefore has to be able to create waves that can interfere destructively with the incident wave. This leads to the thesis stated by Falnes and Budal in 1978: "In order for an oscillating system to be a good wave absorber it should be a good wave generator" [19]. Hence, in order to absorb wave energy, it is necessary to displace water in an oscillatory manner with the correct amplitude and phase. As depicted in Fig. 2.6, a point absorber oscillating in heave only, generates a symmetric wave (Fig. 2.6 (b)). The wave radiated towards left, and the resulting wave transmitted towards right, both have amplitude equal to half of the amplitude of the incident wave. Since the wave energy is proportional to the square of the wave amplitude, this means that 25% of the wave energy is reflected towards left, and 25% of it transmitted towards right. The remaining 50% is absorbed by the WEC [20]. A point absorber oscillating in pitch only, on the other hand, generates an antisymmetric wave (Fig. 2.6 (c)). The linear superposition of Fig. 2.6 (a) and Fig. 2.6 (c) results again in a theoretical power absorption of 50%. A point absorber extracting wave energy from oscillations in a single degree of freedom can therefore never absorb more than 50% of the incident wave energy. However, a device oscillating in heave and pitch can theoretically absorb 100% of the incoming wave energy, as shown by Fig. 2.6 (d), which is the linear superposition of Fig. 2.6 (a), (b) and (c).

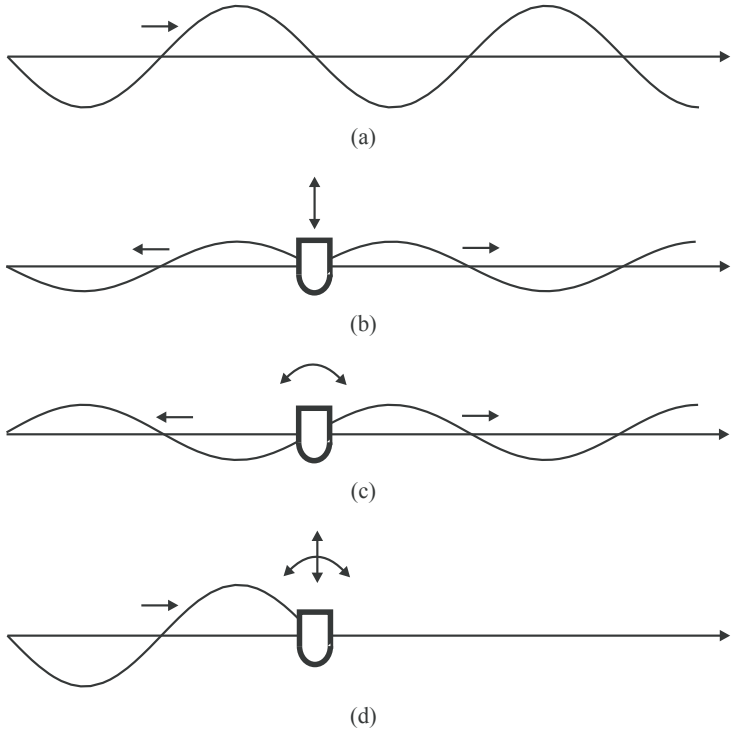

Figure 2.6: Two dimensional wave interference. (a) Undisturbed incident wave (b) symmetric wave generated by heaving oscillation (c) antisymmetric wave generated by pitching oscillation (d) superposition of (a), (b) and (c) resulting in complete absorption of the incident wave system [20]

2.5.1 The Wavebob point absorber

The WEC designed by Wavebob is an axi-symmetric, self-reacting point absorber that primarily operates in the heave mode. It consists of two concentric floating buoys: a torus and a float-neck-tank (FNT). Fig. 2.7 shows a 1:4 scale Wavebob model at sea. A catenary mooring system is generally used for this type of WEC to prevent the device from drifting. The principle of operation of the device can be explained by referring to the schematic cross-section the Wavebob in Fig. 2.8. In this figure, the torus can be clearly seen as the outer floating body while the FNT is the surface piercing body positioned inside the torus with a small gap, called a moonpool, separating the two bodies. The PTO system can be seen attached to the top of the structure. To maximize the relative motion, the FNT is designed to have a low natural frequency, so that the FNT response will be phase shifted from that of the free surface as much as possible. The torus on the other hand is designed to maximize wave following behaviour, by employing a small mass and a high buoyancy stiffness. This results in both buoys responding with different amplitudes and

phases when excited by ocean waves, thus creating relative motion between them. The torus and FNT are linked via the PTO unit, which transforms the available energy from relative motion to useful electrical power. The PTO is effectively a damper, tending to reduce the relative motion thus changing the response of the overall system. If a high damping force is applied, both bodies will tend to oscillate without relative motion as if they were a single body. Developing a PTO system for WECs is a huge challenge as it must accommodate both power absorption and survival of extreme waves. The design of a PTO system is beyond the scope of this study.

Figure 2.7: 1:4 scale Wavebob model at sea [21]

2.6 Numerical modelling of wave energy converters

At the design stage of a WEC, a reliable numerical model is an invaluable tool. Such a model allows for not only fundamental design changes (e.g. parameter optimisation), but also for the optimisation of different configurations of WEC. In particular, at an early design stage of the device, the numerical model can allow low cost assessments to be made in a time efficient manner, without the need for expensive experimental tank testing. When the numerical model gives satisfactory results, a physical model can then be tested to validate the numerical simulations and to investigate phenomena which are not evident through computational simulations. A numerical model is not only useful in the design stage, but also for ongoing development, and for implementation of control

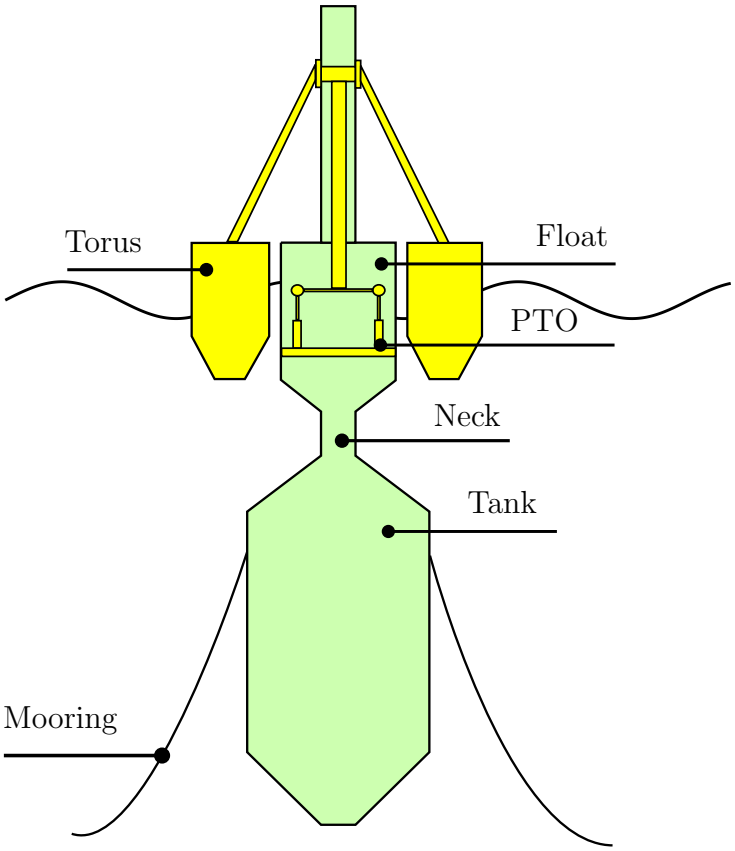

Figure 2.8: Schematic cross-section of the Wavebob wave energy converter

strategies to optimise the performance of the device.

While there are numerous methods for the modelling of WECs, one of the initial steps in developing any type of WEC numerical model is to solve the governing equations for fluid flow, notably the continuity equation and the conservation of momentum. The continuity equation ensures that mass is conserved while the conservation of momentum classifies the problem into either viscous or inviscid flow.

Viscous flow models based on the Navier-Stokes equations have the capabilities of predicting viscous effects of boundary layer separation, turbulence, and wave breaking, which can be important in the modelling of WECs. In these models, the free surface is usually predicted using a "numerical wave tank", employing methods such as the Volume-of-Fluid method and the Marker-and-Cell method. A review of these techniques for tracking the free surface is given by Lin and Liu [22].

There are a range of numerical methods which can be used in turbulent flow modelling in Computational Fluid Dynamics (CFD), including direct numerical simulations, large eddy

simulations and detached eddy simulations. The most widely used CFD method for the hydrodynamic modelling of WECs is the Reynolds-Averaged Navier-Stokes (RANS) due to their reduced computational requirements. Particular applications of RANS methods to WECs were carried out by Agamloh et al. [23], who used RANS to study the power capturing efficiency of a single degree of freedom heaving buoy WEC, while Yu and Li [24] obtained good comparisons with experimental heave free decay tests of a two-body floating point absorber type WEC using RANS. Schmitt et al. [25] applied the RANS method to study the hydrodynamic loading of a bottom hinged, oscillating wave surge converter, using comparisons with experimental results to validate the method.

Although methods using the Navier-Stokes equations are still deemed to be too computationally expensive in the analysis of WECs, it is however a very active area of research at the moment. Schmitt et al. [26] outlines some of the challenges and advantages in the application of CFD methods in the design process of a WEC.

This thesis focuses on numerical models involving inviscid, irrotational flows using Boundary Element Methods (BEM). The BEM procedure solves linear partial differential equations which have been formulated in boundary integral form. The velocity potential of the boundary value problem is solved by discretising the boundary surface and applying suitable boundary conditions to the domain. There are a number of BEM commercial software packages for the analysis of wave structure interactions such as WAMIT and MOSES. An in depth review into the theory of BEM is provided by Lee and Newman [27].

Numerical models based upon BEM are usually calculated in the frequency domain. Frequency domain based representations are utilised due to their simplicity and computational efficiency. However, one must be aware of both the assumptions and limitations with which linear frequency domain models are based upon. Frequency domain solutions are based on linear theory, which assumes small amplitude waves and that the body response due to wave excitation is proportional to the wave amplitude. Due to the assumption of linearity, the principle of superposition is applicable so that the total velocity potential can be obtained as the sum of a radiation problem and an excitation problem. Besides having the advantage of being computationally efficient, an in-depth knowledge of the underlying physics of the device is not required; just the general geometry and mass properties are needed. Frequency domain analysis therefore provides a good first

step in the design process of mooring configurations, PTO systems, system parameters (natural frequencies etc.) and also to define rough estimates of power output. Bosma et al. [28] applied a frequency domain approach to a generic two-body point absorber to obtain preliminary performance results. De Backer et al. [29] assessed the performance of an array of closely spaced point absorbers in the frequency domain in order to optimise certain PTO parameters.

While classic linear theory has proven sufficient for describing small motions due to small amplitude waves, WECs are often subject to many nonlinearities, such as those from PTO systems, complex mooring arrangements and nonlinear responses due to large amplitude motions. In this case, the linear model will not be able to accurately represent the actual system dynamics. As a result, time domain models of WECs are often employed to take these nonlinear characteristics into account. A common approach to time domain modelling is the use of hybrid frequency-time domain models, which are time domain models based upon frequency domain solutions. Examples of hybrid frequency-time domain methods for modelling floating bodies are given by Gilloteaux et al. [30] and Guerinel et al. [31]. The hydrodynamic coefficients are first calculated in the frequency domain, and then transformed into time domain responses via the inverse Fourier transform. The advantage of this method is that nonlinearities can be added as additional forces. Hals et al. [32] used a hybrid frequency-time domain model to study the dynamics of a two-body WEC, consisting of a semi-submersible platform and a single buoy, both restricted to move in the heave mode only. The hydrodynamic excitation and radiation forces, as well as the hydrostatic stiffness forces were assumed to be linear, while the forces due to the viscous damping of the pontoon and the hydraulic PTO were implemented using a nonlinear approach.

Further examples of hybrid frequency-time domain models are provided by Gilloteaux et al. [33], Babarit et al. [34] and Rogne [35] in which it is assumed in these works that the dominant forces are the Froude-Krylov excitation forces and the hydrostatic restoring forces. These forces are considered using a nonlinear approach by integrating the hydrodynamic and hydrostatic pressure over the instantaneous wetted surface of the body, instead of on the mean wetted surface, as is done in linear modelling. The diffraction and radiation force are modelled using a linear approach in these works. Nonlinear radiation

and diffraction forces are considered by Lin and Yue [36], where the instantaneous body boundary conditions are satisfied on the instantaneous wetted surface of the moving body, while the free surface boundary conditions are linearised. This approach is known as the exact body approach. Another approach, known as the weak scatter formulation, involves solving the free surface boundary conditions on the exact wetted surface, rather than on the mean wetted surface. Bretl [37] used this method on a data buoy which uses relative motion to a planar pendulum to extract energy.

Time domain models of offshore structures based on frequency domain data are usually constructed using the Cummins equation [38]. This results in a vector integro-differential equation involving convolution terms. The main drawback to this method is that the calculation of the convolution terms is computationally demanding, especially when a small time step is used and/or the system has a large number of degrees of freedom. Based upon the linearity of the convolution operation, there are different approaches which can be used to replace the convolution terms, for example, using system identification techniques. Taghipour et al. [39] compare some of these different techniques in terms of complexity and performance, by comparing results from time domain response simulations of a container vessel.

A higher level approximation has been used by Gilloteaux [40], who developed the convolution terms up to second order by including the quadratic terms of Bernoulli's equation, while a Taylor series expansion of the time derivative of the total potential was used for a more precise solution. Merigaud et al. [41] applied the same approach to a spherical wave energy absorber and concluded that the inclusion of such nonlinearities in the diffraction and radiation convolutions was not beneficial, in terms of increased accuracy of motion response, when taking into account the additional computational complexity. He showed that the dominant nonlinear force was the Froude-Krylov excitation force and the nonlinear hydrostatic restoring force.

When choosing a suitable numerical model, it is important to have a good understanding of the underlying physics of the interaction between the WEC and the fluid, and in particular, if there are certain phenomenon which should be captured in the model. The hybrid frequency-time domain BEM is used in the current work as it has been observed from experiments in regular waves, that a point absorber is often subject to large amplitude

motions due to the phenomenon of parametric resonance, where the roll/pitch motions are amplified under certain wave conditions. This phenomenon cannot be captured using a linear frequency domain model, as in such a model, the roll mode is uncoupled from the surge, heave and pitch modes, and the wetted surface is assumed to be constant, due to the underlying assumption of small amplitude waves. Therefore, a fully coupled nonlinear model is required, where it is necessary to integrate the hydrodynamic and hydrostatic pressure on the instantaneous wetted surface of the body to obtain an accurate solution. The governing equations of the fluid mechanics used in the numerical model in this study will be presented in Chapter 3.

2.7 Resonance and parametric resonance

Oscillations are called forced if an oscillator is subjected to an external periodic influence, whose effect on the system can be expressed by a separate term, a given periodic function of the time, in the differential equation of motion describing the system. After a transient process is over, the forced oscillations become stationary and acquire the period of the external influence (the steady-state forced oscillations). When the frequency of the external force is close to the natural frequency of the oscillator, the amplitude of steady-state forced oscillations can reach significant values. This phenomenon is called resonance.
Consider the mass, spring, damper system subjected to a harmonic force where the equation of motion is

$$m\ddot{x} + b\dot{x} + kx = F_o \cos(\omega t) \tag{2.3}$$

where m is the mass of the system, b is the linear damping coefficient, k is the linear stiffness coefficient and F_o is the amplitude of the forcing function. The solution of Eqn. 2.3 consists of two parts:

• The particular solution which is harmonic of the form

$$x_p(t) = X \cos(\omega t - \theta) \tag{2.4}$$

where X and θ denote the amplitude and phase angle of the response respectively. By substituting Eqn. 2.4 into Eqn. 2.3 and manipulating, we get

$$X = \frac{F_o}{\left[(k - m\omega^2)^2 + b^2\omega^2\right]^{1/2}} \tag{2.5}$$

and

$$\theta = \tan^{-1}\left(\frac{b\omega}{k - m\omega^2}\right) \tag{2.6}$$

• The homogenous solution is assumed to be of the form

$$x_h(t) = Ce^{st} \tag{2.7}$$

where C and s are undetermined constants. Be inserting Eqn. 2.7 into Eqn. 2.3 and letting $F_o\cos(\omega t) = 0$, we get after manipulation

$$x_h(t) = C_1 e^{(-\zeta+\sqrt{\zeta^2-1})\omega_n t} + C_2 e^{(-\zeta-\sqrt{\zeta^2-1})\omega_n t} \tag{2.8}$$

where C_1 and C_2 are determined from initial conditions and ζ is the damping ratio. The total solution to Eqn. 2.3 is then given by $x(t) = x_p(t) + x_h(t)$. Thus

$$x(t) = X\cos(\omega t - \theta) + Ae^{\left(-\frac{b}{2m}+\sqrt{(\frac{b}{2m})^2-\frac{k}{m}}\right)t} + Be^{\left(-\frac{b}{2m}-\sqrt{(\frac{b}{2m})^2-\frac{k}{m}}\right)t} \tag{2.9}$$

where A and B are determined by initial conditions and X and θ are given in Eqn. 2.5 and Eqn. 2.6 respectively. The homogenous solution $x_h(t)$ dies away to practically zero for all cases ($\zeta < 1, \zeta = 1, \zeta > 1$). Thus, this part of the solution is termed the transient part. What's left ($x_p(t)$) is the long-term behaviour of the system, termed the steady-state part ($x_{ss}(t)$).

$$x_{ss}(t) = x_p(t) = X\cos(\omega t - \theta) \tag{2.10}$$

Fig. 2.9 illustrates how the response of the system represented in Eqn. 2.3 varies with frequency. The phenomenon of resonance is clearly demonstrated when $\omega = \omega_n$. It can be seen that without damping ($\zeta = 0$), the amplitude approaches infinity at resonance, i.e., the oscillations are unbounded. In the real case, there will be some level of damping in the system, and the oscillations will be reduced at resonance, as shown in Fig. 2.9 for the cases when $\zeta > 0$. It should be noted that the frequency response in Fig. 2.9 is for a linear system. By adding a nonlinearity to the system, the frequency response can be altered significantly. The single degree of freedom Duffing equation, with a nonlinear cubic stiffness, is a commonly used equation for studying nonlinear behaviour. The Duffing equation with linear damping can be expressed as

$$m\ddot{x} + b\dot{x} + kx + k_3x^3 = F_o\cos(\omega t) \tag{2.11}$$

The frequency response for this system differs from the linear case in that the resonance frequency shifts up for a hardening system ($k_3 > 0$), and shifts down for a softening system ($k_3 < 0$), with respect to the linear case ($k_3 = 0$). The effect of increasing the amplitude of the excitation, is instead, to bend the curves away from the linear case as illustrated in Fig. 2.10, which illustrates the case of a hardening system. Such an effect gives rise to hysteresis in the nonlinear system. Another way to excite a system involves

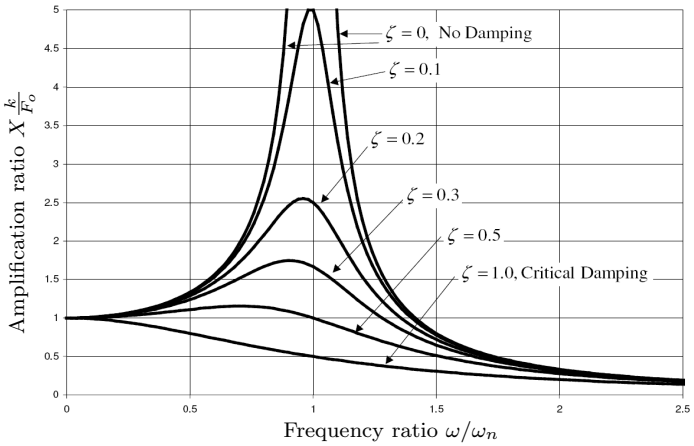

Figure 2.9: Variation of amplitude with frequency ratio for harmonically excited motion [42]

a periodic variation of some parameter of the system. Such a system is called a parametrically excited system; hence the system is mathematically described by differential equations with time-varying coefficients. When the amplitude of oscillation caused by the periodic modulation of some parameter increases steadily, the phenomenon is described as parametric resonance. In this situation, equilibrium becomes unstable and the system performs oscillations whose amplitude progressively increases. The final state of the system depends on the level of damping in the system. The causes and characteristics of parametric resonance are considerably different from those of the resonance occurring when a system responds to a periodic external force. Specifically, the resonant relationship between the frequency of modulation of the parameter and the mean natural frequency of the system is different from the relationship between the driving frequency and the natural frequency for the usual resonance in forced oscillations. The strongest parametric oscillations are excited when the frequency of parametric modulation is twice the natural frequency of the system. However, if there is damping in the system, the amplitude of

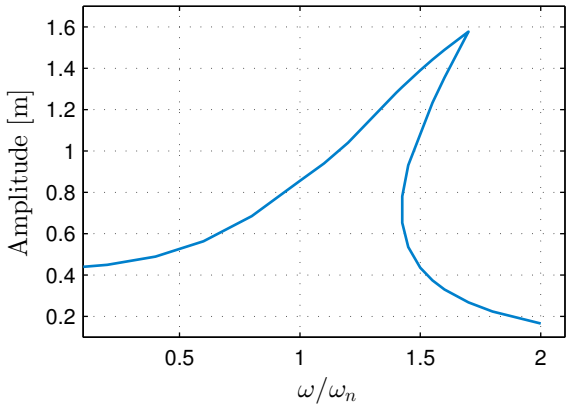

Figure 2.10: Frequency response of the duffing equation

modulation of the parameter must exceed a certain damping threshold value in order to cause parametric resonance. Also, in a parametrically excited system, there does not need to be an external force to excite the system. A predominant example in the literature of parametrically excited systems is provided by use of the Mathieu equation. Mathieu's equation is a second order linear nonautonomous ordinary differential equation which can be expressed as

$$m\frac{d^2x}{dt^2} + b\frac{dx}{dt} + k(t)x = 0 \tag{2.12}$$

where x is the state, $m > 0$ is the mass of system and $b > 0$ is a constant damping parameter. A time-varying harmonic restoring coefficient is expressed as $k(t) = k + a\cos(\omega t)$ with $k > 0$, $a > 0$ and $\omega > 0$ constant. By dividing by the mass m, this can be expressed as

$$\frac{d^2x}{dt^2} + \gamma\frac{dx}{dt} + (\omega_n^2 + \beta\cos(\omega t))x = 0 \tag{2.13}$$

where ω_n is the natural frequency of the system and

$$\begin{aligned} \gamma &= \frac{b}{m} = 2\zeta\omega_n \\ \beta &= \omega_n^2\left(\frac{a}{k}\right) \end{aligned} \tag{2.14}$$

with ζ representing the damping ratio. Using the change of variable $\tau = \omega t$ and dividing all terms by ω^2 gives

$$\frac{d^2x}{d\tau^2} + \mu\frac{dx}{d\tau} + (\delta + \epsilon\cos(\tau))\,x = 0 \tag{2.15}$$

where

$$\begin{aligned} \mu &= 2\zeta \left(\frac{\omega_n}{\omega}\right) \\ \epsilon &= \beta/\omega^2 \\ \delta &= \omega_n^2/\omega^2 \end{aligned} \tag{2.16}$$

The Mathieu equation cannot be solved analytically in terms of standard functions as one of the coefficients is time-dependent. However, the stability of the system can be studied for different values of the parameters δ and ϵ resulting in stable and unstable regions. Fig. 2.11 shows an example of the stability regions for the Mathieu equation. The curves in the $\delta - \epsilon$ plane represent stability changes, and are called transition curves. The regions enclosed by the transition curves define a region of instability, called a tongue. The different points on the δ axis where a tongue of stability emanates can be calculated using different techniques, such as the regular perturbation method, two variable expansion method, Floquet theory or harmonic balance [43], resulting in

$$\delta = \frac{n^2}{4} \qquad n = 0, 1, 2, 3, ... \tag{2.17}$$

The $n = 0$ case is an exception, as only one transition curve emanates from it. Transition curves for the Mathieu equation can be derived for each value of n as illustrated in Fig. 2.11 (for $n = 0, 1, 2$ and 3). The shaded regions in Fig. 2.11 represent unstable or unbounded solutions while the unshaded regions represent stable or bounded solutions. An example of the transition curve for $n = 1$ is [43]

$$\delta = \frac{1}{4} \pm \frac{\sqrt{\epsilon^2 - \mu^2}}{2} + O(\epsilon^2) \tag{2.18}$$

This predicts that for a given damping coefficient μ, there is a minimum value of ϵ which is required for instability to occur. When there is no damping, the $n = 1$ tongue emanates from the δ axis. Examples of a bounded solution and an unbounded solution to the Mathieu equation without damping can be seen in Fig. 2.12 and 2.13 respectively. It can be seen that the amplitude of the oscillation remains within a certain interval for the bounded solution, whereas the oscillations diverge in the case of the unbounded solution, which is further illustrated in the phase plane diagram in Fig. 2.13(b). The red marker in the phase diagram illustrates the initial condition of the system.

From Eqn. 2.17 it can be seen that the region of instability for $n = 1$ corresponds to a value of $\delta = 1/4$. This relates to a frequency tuning factor (ω_n/ω) of 1/2, so the excitation frequency is twice the natural frequency of the system. The motion belonging to this zone is commonly referred to as the principal parametric resonance [44]. It will be shown in Chapter 6 that the Wavebob is prone to parametric resonance in this zone of instability, when the wave excitation frequency is twice the roll/pitch natural frequency.

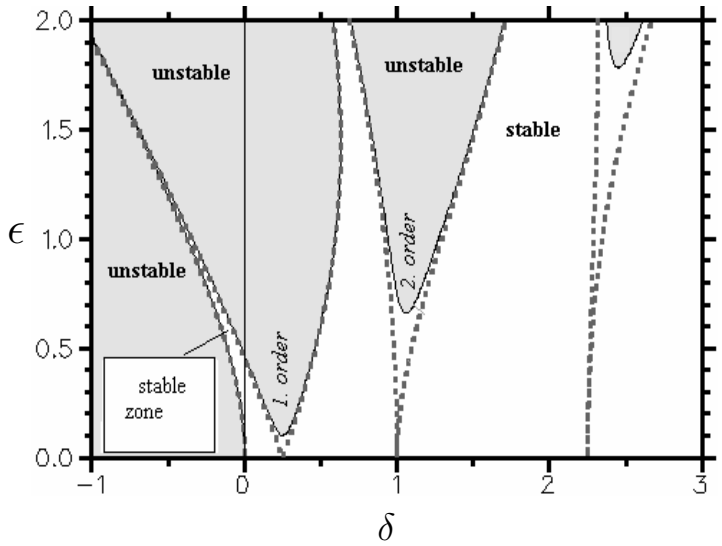

Figure 2.11: Mathieu stability diagram for $n = 0$, 1, 2 and 3. The transition curves divide the $\delta - \epsilon$ plane into stable (unshaded) and unstable (shaded) regions. The dashed transition curves are for a system with no damping while the solid transition curves have damping in the system [45]

2.7.1 Parametric resonance of offshore structures

It is well known that floating structures can be subject to nonlinear unstable motions when heave resonance produces large heave motions, even with small wave excitation. The excitation energy input to the heave or pitch mode may be transferred into the roll motion, due to nonlinear coupling among these modes. This can result in large amplitude roll motions, as well as large heave and pitch motions due to parametric resonance.

Early studies into the field of parametric resonance of offshore structures focused on the parametric roll of ships, due to accidents involving loss of cargo to container ships as a result of large roll angles due to parametric roll [46]. Numerous mathematical models for describing the dynamics of parametric roll of ships have been proposed over the years, the

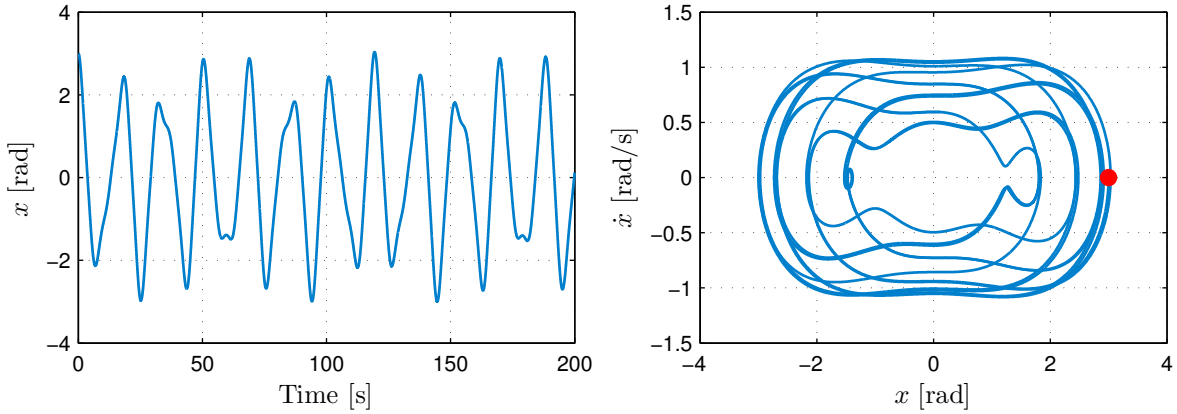

(a) Bounded solution to the Mathieu equation (b) Phase plane plot

Figure 2.12: Bounded solution to Mathieu equation for $\delta = 0.1$, $\epsilon = 0.19$ and $\mu = 0$

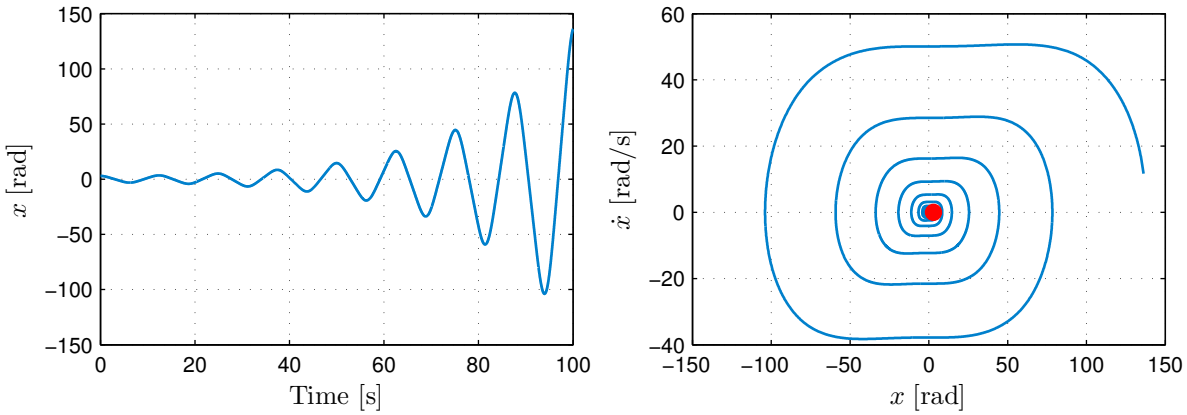

(a) Unbounded solution to the Mathieu equation (b) Phase plane plot

Figure 2.13: Unbounded solution to Mathieu equation for $\delta = 0.16$, $\epsilon = 0.19$ and $\mu = 0$

most common method based on a Mathieu-type (or Mathieu-Duffing type) 1 degree of freedom roll equation, to describe the onset of heavy roll motion in regular, longitudinal seas. Examples can be found in Shin et al. [44] and Umeda et al. [47].

It is widely believed that one of the main factors driving parametric resonance in ships is due to the time varying waterplane area, when a wave crest or trough is amidships, as illustrated in Fig. 2.14, an effect which is accentuated for ships with large bow flare and stern overhang. This may not, however, be the case for parametric resonance of point absorbers, which are characterised by a large draught in comparison to the diameter of the body at the water surface. There is little work published in the literature on parametric resonance of point absorbers, however, insight into the physics behind parametric motion

of such devices may be gained by observing parametric instabilities of spar platforms and vertical cylinders, which have similar geometric properties to point absorbers.

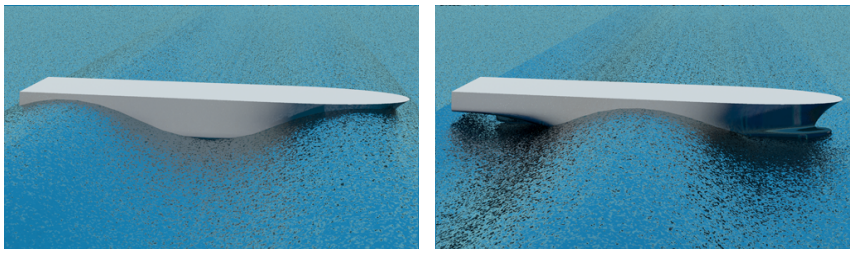

(a) Wave trough (b) Wave crest

Figure 2.14: Variation in wetted surface of a ship due to a wave trough (a) and a wave crest (b) [48]

Investigations into the occurrence of parametric resonance of spar platforms have been published [49–51] in which the unstable motions were attributed to Mathieu type instabilities, associated with sinusoidal variations of the metacentric height appearing in the roll/pitch hydrostatic restoring force. Depending on the values of the coefficients in the Mathieu equation, the solution yields either a bounded or unbounded solution. It was assumed in each of these works that the variation in submerged volume and wave passage effects are not important in the analysis of parametric motion. Neves et al. [52] demonstrated analytically, that in the case of structures with vertical walls, simple harmonic parametric excitation does not come from pure hydrostatic terms as in the case of ships, but instead from wave passage effects only. They showed that the hydrostatic contribution to parametric excitation of roll (or pitch) due to heave is composed of a bi-harmonic and a time independent term. Liu et al. [53] and Li et al. [54] present numerical examples of parametric instabilities of spar platforms with their models focusing on heave-pitch coupling.

This current work investigates a different occurrence of parametric resonance than that which occurs in ships or spars, namely one that occurs in point absorbers, involving relative motion between two floating bodies which are connected by a PTO. It is not clear what the effect of the relative motion and the level of PTO damping has on parametric resonance. The aim of the current work is to to clarify these issues by implementing a nonlinear model to the Wavebob in order to predict the motions of the device in the time domain.

Chapter 3

Theoretical Modelling Of Floating Bodies

3.1 Basic definitions

This chapter summarises the underlying mathematical theory used for the numerical modelling of floating bodies. The content for a large part of this chapter is drawn from the books of Newman [55], Falnes [56] and Cruz [57], while other sources are also used where referenced. A Cartesian coordinate system is adopted which is fixed in space, with the x-y plane lying parallel with the quiescent free surface ($z = 0$), the positive x axis is in the direction of wave propagation and the z axis is positive upward. Fig. 3.1 illustrates this system for a floating body. The motion of a rigid floating body is described by the vector $\boldsymbol{\xi}$ with components ξ_j, where j=(1,2...6). The motion vector is characterised by three translations in the direction of the x, y and z axes, known as surge ($j = 1$), sway ($j = 2$) and heave ($j = 3$) respectively. The rotational motions about the x, y and z axes are known as roll ($j = 4$), pitch ($j = 5$) and yaw ($j = 6$) respectively.

3.2 Governing equations of fluid mechanics

The velocity of the moving fluid at a fixed location with coordinates $\mathbf{x} = [x_1, x_2, x_3]$ at time t is given by

$$\mathbf{u}(\mathbf{x}, t) = [u_1(\mathbf{x}, t), u_2(\mathbf{x}, t), u_3(\mathbf{x}, t)] \tag{3.1}$$

To describe the flow past a floating body, it is necessary to solve the continuity equation and Navier-Stokes equation. The continuity equation relies on the fundamental concept of

conservation of mass. The continuity equation states that the rate at which mass enters a system is equal to the rate at which mass leaves the same system. The continuity equation can be expressed in differential form as

$$\frac{\partial \rho}{\partial t} + \nabla \cdot (\rho \mathbf{u}) = 0 \tag{3.2}$$

For the flow velocities involved in this analysis, the fluid can be considered incompressible so that the density ρ can be assumed constant in space and time. Thus, Eqn. 3.2 can be simplified to the continuity equation for incompressible flows which can be written as

$$\nabla \cdot \mathbf{u} = \frac{\partial u_1}{\partial x} + \frac{\partial u_2}{\partial y} + \frac{\partial u_3}{\partial z} = 0 \tag{3.3}$$

The conservation of momentum for a viscous flow is described by the Navier-Stokes equations. In this analysis, the effect of viscosity is neglected and the fluid is said to be an ideal fluid. When viscosity is disregarded, the Navier-Stokes equation is known as the Euler equation, which is expressed as

$$\rho(\frac{\partial \mathbf{u}}{\partial t} + \mathbf{u} \cdot \nabla \mathbf{u}) = \mathbf{f} - \nabla p \tag{3.4}$$

where $\mathbf{f}$ are the external forces per unit volume and p is the pressure. Gravity is the only external force considered in this analysis such that

$$\mathbf{f} = -\rho g \mathbf{k} \tag{3.5}$$

where $\mathbf{k}$ is the unit vector in the upward direction and g is assumed constant.

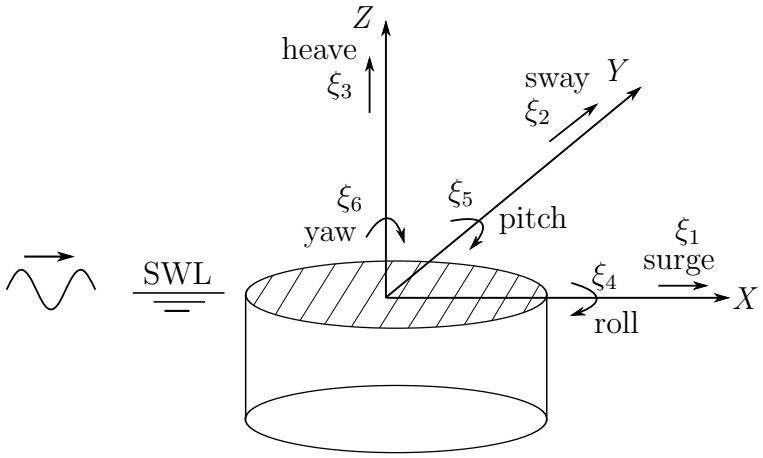

Figure 3.1: Translational and rotational modes of motion for a floating body with a wave propagating in the positive x direction

3.3 Formulation of the boundary value problem

The fluid is also assumed to be homogenous and with an irrotational flow. In the case of irrotational flow, where the vorticiy is equal to zero ($\nabla \times \mathbf{u} = 0$), the velocity can be written as the gradient of a scalar function ϕ called the *velocity potential* such that

$$\mathbf{u} = \nabla\phi = \frac{\partial\phi}{\partial x}\mathbf{i} + \frac{\partial\phi}{\partial y}\mathbf{j} + \frac{\partial\phi}{\partial z}\mathbf{k} \tag{3.6}$$

The advantage of using the velocity potential is that it greatly simplifies the analysis of the flow. Instead of dealing with the three velocity components, requiring three equations to be solved, only a single equation needs to be solved for the flow field. Once ϕ is known, the velocity components can be obtained directly from Eqn. 3.6 . Substituting Eqn. 3.6 into Eqn. 3.3 leads to the familiar Laplace equation

$$\nabla^2\phi = \frac{\partial^2\phi}{\partial x^2} + \frac{\partial^2\phi}{\partial y^2} + \frac{\partial^2\phi}{\partial z^2} = 0 \tag{3.7}$$

The Laplace equation is the governing second order differential equation for the fluid motion under a periodic water wave, which holds throughout the domain. The Laplace equation can be solved subject to appropriate boundary conditions to find the velocity potential and thus the velocities. The pressure in the fluid can be found by inserting Eqn. 3.6 into Eqn. 3.4 and integrating, resulting in

$$\frac{p}{\rho} + \frac{\partial\phi}{\partial t} + \frac{1}{2}(\nabla\phi)^2 + gz = C \tag{3.8}$$

where C a constant of integration. Eqn. 3.8 is known as the Bernoulli equation. For the case of when the fluid is not in motion (ϕ = constant and $\mathbf{u} = 0$) we get

$$p = -\rho g z + \rho C \tag{3.9}$$

For the particular case at the still water level ($z = 0$), we have $p = p_o$, where p_o is atmospheric pressure. This gives $C = p_0/\rho$, so that the relative pressure can be computed from

$$p - p_0 = -\rho\frac{\partial\phi}{\partial t} - \frac{1}{2}\rho(\nabla\phi)^2 - \rho g z \tag{3.10}$$

3.3.1 Boundary conditions

In order to solve Eqn. 3.7 and Eqn. 3.10, the velocity potential must satisfy appropriate boundary conditions to describe a particular physical situation. We consider a fluid unbounded in the x-y plane, but with boundary conditions to be met on the free surface, on the seabed, and on the wetted surface of the floating body. The boundary conditions are of kinematic and dynamic nature.

3.3.1.1 Boundary conditions on a solid boundary

At a solid boundary, a no normal-flux condition is applied as no fluid can go through nor come out of the solid boundary. This implies that the normal component of the fluid velocity is equal to that of the velocity of the boundary itself. This kinematic boundary condition can be expressed as

$$\frac{\partial \phi}{\partial n} = \mathbf{v} \cdot \mathbf{n} = v_n \qquad \text{on } S_b \tag{3.11}$$

where $\mathbf{v}$ is the velocity of the considered point on the body surface S_b, and $\mathbf{n}$ is the unit normal vector at the considered point. The dot product of the vectors $\mathbf{v}$ and $\mathbf{n}$ results in the normal velocity component v_n at the surface of the body.
A kinematic condition is also applied on the impermeable seabed. If we assume that the seabed is stationary ($v_n = 0$) and that the level of the surface is horizontal so that it is at a fixed depth h below the still water level, we can write

$$\frac{\partial \phi}{\partial z} = 0 \qquad \text{for } z = -h \tag{3.12}$$

3.3.1.2 Boundary conditions on the free surface

The free surface can be described by the function $F(x, y, z, t) = z - \zeta_w(x, y, t) = 0$, where $\zeta_w(x, y, t)$ is the displacement of the free surface about the horizontal plane. The kinematic boundary condition states that a fluid particle on the free surface is assumed to stay on the free surface, such that $DF/Dt = 0$, where D/Dt is the total derivative. This results in

$$\frac{\partial \phi}{\partial z} = \frac{\partial \zeta_w}{\partial t} + \frac{\partial \phi}{\partial x}\frac{\partial \zeta_w}{\partial x} + \frac{\partial \phi}{\partial y}\frac{\partial \zeta_w}{\partial y} \qquad \text{for } z = \zeta_w(x, y, t) \tag{3.13}$$

A dynamic boundary condition on the free surface relies on the assumption that the water pressure on the free surface equals atmospheric pressure. By applying Eqn. 3.10 at the free surface we get

$$g\zeta_w + \frac{\partial \phi}{\partial t} + \frac{1}{2}(\nabla\phi)^2 = 0 \qquad \text{for } z = \zeta_w(x, y, t) \tag{3.14}$$

3.3.2 Linearisation of the boundary conditions

The Laplace equation in Eqn. 3.7 cannot be solved analytically due to the nonlinearity of the free surface boundary conditions and the fact that the free surface $\zeta_w(x, y, t)$ is initially an unknown function. To circumvent this problem, we apply a linearisation procedure, known as Airy theory, which assumes that the wave height is small relative to the wavelength and to the water depth ($H/\lambda \ll 1$ and $H/h \ll 1$). With these assumptions, the nonlinear terms in the free surface equations of Eqn. 3.13 and Eqn. 3.14 are small and can be neglected. By taking a Taylor series expansion of ϕ about $z = 0$, so as to calculate the value of ϕ at $z = \zeta_w(x, y, t)$, Andersen et al. [58] show that the terms containing ϕ are to be evaluated at $z = 0$ instead of at $z = \zeta_w(x, y, t)$ upon being linearised.
By applying this linearisation, Eqn. 3.13 and Eqn. 3.14 become (respectively)

$$\frac{\partial \phi}{\partial z} = \frac{\partial \zeta_w}{\partial t} \qquad \text{for } z = 0 \tag{3.15}$$

$$g\zeta_w + \frac{\partial \phi}{\partial t} = 0 \qquad \text{for } z = 0 \tag{3.16}$$

To reduce the mathematical complexity of the problem, ζ_w is eliminated from Eqn. 3.16 and Eqn. 3.15 by taking the partial time derivative of Eqn. 3.16, and inserting it into Eqn. 3.15. This gives the combined surface boundary condition as

$$\frac{\partial \phi}{\partial z} + \frac{1}{g}\frac{\partial^2 \phi}{\partial t^2} = 0 \qquad \text{for } z = 0 \tag{3.17}$$

3.3.3 Plane progressive waves

Since the Laplace equation (Eqn. 3.7) to be solved is linear, and hence superposition is valid, there are several solutions for the velocity potential that satisfy the Laplace equation in the case of a horizontally unbounded fluid in the absence of a floating body, subjected

to the boundary conditions Eqn. 3.12 and Eqn. 3.17. Once such solution [59] is that of a plane progressive wave for which the solution can be expressed as

$$\phi = \frac{\zeta_o g}{\omega} \frac{\cosh(k(z+h))}{\cosh(kh)} \sin(kx - \omega t) \tag{3.18}$$

where ζ_o is the wave amplitude, $\omega = 2\pi/T$ is the wave field's angular frequency, $k = 2\pi/\lambda$ is the wavenumber, λ is the wavelength and h is the water depth. The potential in Eqn. 3.18 describes waves propagating along the positive x-axis. By combining the free surface boundary condition in Eqn. 3.17 with the velocity potential in Eqn. 3.18, we get

$$\omega^2 = gk \tanh(kh) \tag{3.19}$$

Eqn. 3.19 is known as the *dispersion relationship* relating the wavenumber to the angular frequency. In the case of deep water, Eqn. 3.18 is simplified to:

$$\phi = \frac{g\zeta_o}{\omega} e^{kz} \sin(kx - \omega t) \tag{3.20}$$

and the dispersion relation becomes

$$k = \frac{\omega^2}{g} \tag{3.21}$$

The associated water surface displacement is obtained by combining Eqn. 3.16 and Eqn. 3.20 as

$$\zeta_w(x, y, t) = \zeta_o \cos(kx - \omega t) \tag{3.22}$$

3.4 Wave body interactions

We now consider the forces experienced by a rigid body floating in the fluid subject to waves, and also the forces exerted on the fluid by the body. As stated in Section 3.1, the motion of a floating body can be described by six components corresponding to

$$\boldsymbol{\xi} = (\xi_1, \xi_2, \xi_3, \xi_4, \xi_5, \xi_6) \tag{3.23}$$

where $j = 1, 2$ and 3 are the translational degrees of freedom corresponding to surge, sway and heave respectively and $j = 4, 5$ and 6 are the rotational degrees of freedom corresponding to roll, pitch and yaw respectively. A normal vector $\mathbf{n}$ at a particular

surface element dS on the wetted body surface S_b, as shown in Fig. 3.2, is defined having components

$$\mathbf{n} = \begin{bmatrix} n_x \\ n_y \\ n_z \\ (s \times n)_x \\ (s \times n)_y \\ (s \times n)_z \end{bmatrix} = \begin{bmatrix} n_1 \\ n_2 \\ n_3 \\ n_4 \\ n_5 \\ n_6 \end{bmatrix} \tag{3.24}$$

where $\mathbf{s}$ is the position vector of the surface element dS in the reference coordinate frame. The components of $\mathbf{n}$ written in the form $n_1, n_2 ... n_6$ is convenient when expressing the forces and moments on the body in component form. A generalised force vector is defined having six components

$$\mathbf{F} = (F_1, F_2, F_3, F_4, F_5, F_6) \tag{3.25}$$

where F_1, F_2 and F_3 correspond to forces along the x, y and z axes respectively and F_4, F_5 and F_6 correspond to moments about the x, y and z axes respectively. The forces and moments acting on the body can be calculated from an integration of the pressure p over the submerged surface S_b of the body. For component j $(j = 1, 2, ...6)$ we have

$$F_j = -\iint_{S_b} p n_j \; dS \tag{3.26}$$

By substituting Eqn. 3.10 into Eqn. 3.26 we get

$$F_j = \iint_{S_b} \left[\rho \left(\frac{\partial \phi}{\partial t} + gz \right) \right] n_j \; dS \tag{3.27}$$

where atmospheric pressure p_0 is taken as zero in Eqn. 3.10 and second order terms assumed small enough to be neglected. Eqn. 3.27 can be re-written in order to separate the integrals as

$$F_j = \iint_{S_b} \rho \frac{\partial \phi}{\partial t} \; n_j \; dS + \iint_{S_b} \rho g z \; n_j \; dS \tag{3.28}$$

where the first integrals in Eqn. 3.28 corresponds to the hydrodynamic forces and moments, while the second integrals corresponds to the hydrostatic forces and moments acting on the body.

The use of complex amplitudes will be used throughout this chapter. The use of a complex representation when dealing with sinusoidal oscillations is as a matter of mathematical convenience. One such advantage is that differentiation with respect to time is represented by multiplying with $i\omega$, where i is the imaginary unit ($i = \sqrt{-1}$). For example, the hydrodynamic pressure term $-\rho(\partial\phi/\partial t)$ in Bernoulli's equation (Eqn. 3.10) can be expressed in terms of complex amplitudes as

$$\hat{p} = -i\omega\rho\hat{\phi} \tag{3.29}$$

Therefore the first integral in Eqn. 3.28 can be expressed in complex notation by inserting Eqn. 3.29 into Eqn. 3.26 as

$$\hat{F}_j = i\omega\rho \iint_{S_b} \hat{\phi} n_j \, dS \tag{3.30}$$

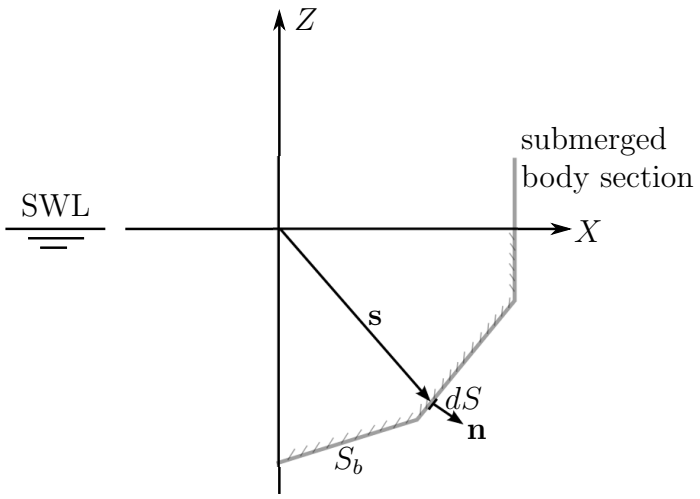

Figure 3.2: Submerged body section S_b in water. Vector $\mathbf{s}$ is the position vector of element dS with unit normal vector $\mathbf{n}$

3.4.1 The total potential

Due to the linear nature of the Laplace equation, it is possible to sum multiple potential functions to obtain the total potential representative of the complete flow field. Each sub-component of the total potential must also satisfy the appropriate boundary conditions. For wave body interactions, the problem is commonly divided into two sub-problems. The first is a radiation problem representing the forced oscillation of the body with harmonic motion in the absence of waves. The second is the excitation problem whereby the body is

subjected to regular incident waves whilst being restrained from oscillating. The velocity potentials for the radiation and excitation are represented by ϕ_r and ϕ_e respectively. The excitation problem can be split into two constituent parts, the incident velocity potential ϕ_i representing the incident waves undisturbed by the body, and the diffraction velocity potential ϕ_d representing the change in the incident wave field due to the presence of the body when it is motionless. Thus the total potential can be written as:

$$\Phi(x, y, z, t) = \Re[\{\hat{\phi}_i(x, y, z) + \hat{\phi}_r(x, y, z) + \hat{\phi}_d(x, y, z)\}e^{i\omega t}] \tag{3.31}$$

in which the space and time dependent potential $\Phi(x, y, z, t)$ is written in terms of a separate space dependent complex amplitude $\hat{\phi}(x, y, z)$ multiplied by an oscillatory time dependent term.

3.4.2 The radiation force

The body undergoes a forced harmonic motion in originally still water. Due to this forced motion, a radiated wave ϕ_r is generated. Taking the hydrodynamic part of Eqn. 3.28, the radiation force for component j $(j = 1, 2, ..., 6)$ can be written

$$F_{r_j} = \rho \iint_{S_b} \frac{\partial \phi_r}{\partial t} n_j \, dS \tag{3.32}$$

In terms of complex amplitudes, Eqn. 3.32 can be written

$$\hat{F}_{r_j} = i\omega\rho \iint_{S_b} \hat{\phi}_r n_j \, dS \tag{3.33}$$

The radiated wave ϕ_r which is generated, is a superposition of radiated waves caused by each of the six oscillation modes. The radiation potential can therefore be decomposed as

$$\hat{\phi}_r = \sum_{j=1}^{6} \varphi_j \hat{\dot{\xi}}_j \tag{3.34}$$

where $\varphi_j(x, y, z)$ is a complex coefficient of proportionality. The complex amplitude $\hat{\phi}_r$ of the radiated velocity potential must satisfy the body boundary condition Eqn. 3.11 such that

$$\frac{\partial \hat{\phi}_r}{\partial n} = \sum_{j=1}^{6} \hat{\dot{\xi}}_j n_j \qquad \text{on } S_b \tag{3.35}$$

Similarly, the coefficient φ_j must also satisfy the body boundary condition such that

$$\frac{\partial \varphi_j}{\partial n} = n_j \qquad \text{on } S_b \tag{3.36}$$

Each φ_j can be interpreted as the complex amplitude of the radiated velocity potential due to the body oscillating in mode j with unit velocity amplitude ($\hat{\dot{\xi}}_j = 1$). The φ_j coefficients must also satisfy the Laplace equation (Eqn. 3.7) and the boundary conditions on the seabed (Eqn. 3.12) and the free surface (Eqn. 3.17).

Writing the complex radiation force amplitude, Eqn. 3.33, in terms of the complex coefficients φ_j, we have for the jth component of the radiation force

$$\hat{F}_{r_j} = i\omega\rho \iint_{S_b} \sum_{k=1}^{6} \varphi_k \hat{\dot{\xi}}_k n_j \, dS \tag{3.37}$$

$$= -\sum_{k=1}^{6} Z_{jk} \hat{\dot{\xi}}_k \tag{3.38}$$

where

$$Z_{jk} = -i\omega\rho \iint_{S_b} \varphi_k n_j \, dS \tag{3.39}$$

is an element of the *radiation impedance* matrix $\mathbf{Z}(\omega)$. The component Z_{jk} is the jth component of the reaction force which is due to wave radiation from mode k oscillating with unit velocity amplitude ($\hat{\dot{\xi}}_k = 1$). When $j = k$, the force or moment is caused by a motion in that same direction. When $j \neq k$, the force in one direction results from motion in another direction, which is known as coupling between the forces and moments.

The radiation force can alternatively be written in vectorial form as

$$\hat{\boldsymbol{F}}_r = -Z(\omega)\hat{\dot{\boldsymbol{\xi}}} \tag{3.40}$$

The radiation impedance matrix $\mathbf{Z}(\omega)$ may be decomposed into real and imaginary components as

$$Z(\omega) = b(\omega) + iX(\omega) = b(\omega) + i\omega a(\omega) \tag{3.41}$$

where $a(\omega) = X(\omega)/\omega$. Substituting Eqn. 3.41 into Eqn. 3.40 allows the complex amplitude of the radiation force to be written as

$$\hat{\boldsymbol{F}}_r = -(b(\omega)\hat{\dot{\boldsymbol{\xi}}} + a(\omega)\hat{\ddot{\boldsymbol{\xi}}}\,) \tag{3.42}$$

where the complex amplitude of the acceleration $\hat{\ddot{\boldsymbol{\xi}}} = i\omega\hat{\dot{\boldsymbol{\xi}}}$ has been used. Eqn. 3.42 shows how the radiation force can be split into coefficients in phase with the acceleration and coefficients in phase with the velocity. The coefficients in phase with the velocity $b(\omega)$ are called potential damping coefficients while the coefficients in phase with the acceleration $a(\omega)$ are called added mass coefficients.

The radiated waves generated by the floating bodies at any given time will persist indefinitely. These generated waves affect the fluid pressure field and hence the body force of the floating body at all subsequent times which introduces memory effects. To account for fluid memory effects, Cummins [38] considered the behaviour of the fluid and the floating body in the time domain, so that the response of the body (in six degrees of freedom) could be represented due to an arbitrary forcing function. Prior to the work of Cummins, it was necessary to choose the frequency at which the added mass and damping were to be considered, since the coefficients of added mass and damping are frequency dependent. Cummins derived the equations of motion by stating that at time $t = 0$ the body is given an impulsive displacement in the jth mode with a constant velocity in initially still water. He then split the fluid velocity potential resulting from the impulse into two parts; the velocity at the instant of the impulse and the decaying response after the impulse. He stated that the fluid velocity potential is proportional to the velocity of the body during the impulse, whereas after the impulse, the velocity potential is proportional to the change in body displacement. He then applied the theory that if the response of a stable linear system to a unit impulse is known, then the response of the system to an arbitrary force is given by the convolution of the input with the systems impulse response. Applying this theory, the radiation force can be expressed as

$$\boldsymbol{F}_r = -a\ddot{\boldsymbol{\xi}} - \int_0^t K_r(t-\tau)\dot{\boldsymbol{\xi}}(\tau)d\tau \tag{3.43}$$

in which the term a in Eqn. 3.43 (proportional to the accelerations) is known as the added mass, representing the inertia of the fluid particles that is put in motion by the body when oscillating. The added mass a is constant and independent of frequency of motion. The term in Eqn. 3.43 that is a convolution with the body velocity arises because the resulting wave created due to the impulse will, in principle, persist at all subsequent times, affecting the motion of the body at subsequent times. This is known as fluid memory effects, and

is captured by the convolution integral. The term $K_r(t)$ is known as the retardation functions or matrix of impulse response functions and depends on the geometry of the body.

In order to relate the matrices a and $K_r(t)$ in Eqn. 3.43 to their frequency domain counterparts, it is necessary to use the approach given by Olgilvie [60], such that

$$a(\omega) = a - \frac{1}{\omega}\int_0^\infty K_r(\tau)sin(\omega\tau)d\tau \tag{3.44}$$

$$b(\omega) = \int_0^\infty K_r(\tau)cos(\omega\tau)d\tau \tag{3.45}$$

Eqn. 3.44 must be valid for all ω, hence, we choose $\omega = \infty$ implying that

$$a = a(\infty) \tag{3.46}$$

Eqn. 3.45 is rewritten using the inverse Fourier transform giving

$$K_r(t) = \frac{2}{\pi}\int_0^\infty b(\omega)cos(\omega t)d\omega \tag{3.47}$$

Therefore, using the approach by Ogilvie, frequency dependent hydrodynamic added mass and damping coefficients can be transformed into frequency independent added mass coefficients and radiation impulse response functions for describing the behaviour of a body and the fluid in the time domain. The frequency dependent added mass and damping coefficients $a(\omega)$ and $b(\omega)$ can be initially calculated experimentally, although due to the complexity in doing so, it is more common to use a frequency domain hydrodynamic software package (such as WAMIT) to calculate the added mass and damping coefficients in the frequency domain for a range of frequencies. The transformations in Eqns. 3.44 - 3.47 can then be applied to obtain the frequency independent added mass at infinite frequency and the radiation impulse response functions.

3.4.3 The excitation force

The excitation force is the force on the body resulting from the incident and diffraction potentials. The principal of superposition allows for the determination of these forces on a restrained body with zero forward speed. Following Eqn. 3.28 this can be written

$$F_{e_j} = \rho \iint_{S_b} \left(\frac{\partial \phi_i}{\partial t} + \frac{\partial \phi_d}{\partial t}\right) n_j \; dS \tag{3.48}$$

$$\hat{F}_{e_j} = i\omega\rho \iint_{S_b} (\hat{\phi}_i + \hat{\phi}_d) n_j \, dS \tag{3.49}$$

The Froude-Krylov component of the total excitation is defined as the contribution from the undisturbed incident wave potential $\hat{\phi}_i$ while the diffraction component of the total excitation corresponds to the contribution from the diffraction potential $\hat{\phi}_d$.
For a given incident wave field, the body boundary condition for the diffraction potential, considering the body at rest, $\dot{\xi}_j = \phi_r = 0$, can be written

$$-\frac{\partial \hat{\phi}_i}{\partial n} = \frac{\partial \hat{\phi}_d}{\partial n} \qquad \text{on } S_b \tag{3.50}$$

The potentials $\hat{\phi}_d$ and $\hat{\phi}_i$ must also satisfy the boundary condition Eqn. 3.12 on the seabed, as well as the free surface boundary condition Eqn. 3.17 at $z = 0$.

3.4.3.1 The diffraction force

The complex amplitude of the diffraction force can be written as

$$\hat{F}_{d_j} = i\omega\rho \iint_{S_b} \hat{\phi}_d n_j \, dS \tag{3.51}$$

The diffraction force can be written in terms of a transfer function $f(\omega)$ such that

$$\boldsymbol{F}_d(\omega) = f(\omega)\zeta_w(\omega) \tag{3.52}$$

Here, the systems input $\zeta_w(\omega)$ is the Fourier transform of the complex elevation amplitude of the undisturbed incident wave at the origin, and $\boldsymbol{F}_d(\omega)$ is the output of the system.
The presence of the body in the fluid results in the diffraction of the incident wave system, and the addition of a disturbance to the incident wave potential associated with the scattering effect of the body. The diffraction force for the currently considered WEC is defined to act at the reference centre of the body. Due to the large geometry of the body, the WEC is affected by the incident wave before it reaches the reference centre. To account for this acausal nature of the excitation force, a convolution product is used to represent the diffraction force by taking the inverse Fourier transform of Eqn. 3.52 such that

$$\boldsymbol{F}_d = \int_{-\infty}^{+\infty} K_d(t-\tau)\zeta_w(\tau)d\tau \tag{3.53}$$

where

$$K_d(t) = \frac{1}{2\pi}\int_{-\infty}^{+\infty} f(\omega)e^{i\omega t}d\omega \tag{3.54}$$

is the impulse response function for the diffraction force and $\zeta_w(x, y, t)$ is the free surface elevation of the incident wave at the prescribed reference point, as defined in Eqn. 3.22.

3.4.3.2 The Froude-Krylov force

The Froude-Krylov force is the force introduced due to the undisturbed incident potential ϕ_i. From Eqn. 3.28, the Froude-Krylov component in direction j is expressed as

$$F_{FK_j} = \rho \iint_{S_b} \frac{\partial \phi_i}{\partial t} n_j \; dS \tag{3.55}$$

$$\hat{F}_{FK_j} = i\omega\rho \iint_{S_b} \hat{\phi}_i n_j \; dS \tag{3.56}$$

where the deep water incident wave potential ϕ_i is obtained from Eqn. 3.20.
In a similar way to the diffraction force, the Froude-Krylov force can be expressed as a convolution integral as

$$\boldsymbol{F}_{FK} = \int_{-\infty}^{+\infty} K_{FK}(t-\tau)\zeta_w(\tau)d\tau \tag{3.57}$$

3.4.4 Hydrostatic force

The hydrostatic component in direction j is obtained from the hydrostatic part of Eqn. 3.28 as

$$F_{hs_j} = \iint_{S_b} \rho g z \; n_j \; dS \tag{3.58}$$

The components due the the weight of the body must be added to the hydrostatic force to calculate the total hydrostatic forces and moments. The forces and moments associated with the weight of the body act through the centre of gravity of the body (x_g, y_g, z_g) and can be expressed according to Newman [55] as

$$\begin{aligned} F_{m_j} &= (0, 0, mg) \qquad j = 1, 2, 3 \\ F_{m_j} &= (mgy_g + mgz_g\xi_4 - mgx_g\xi_6, -mgx_g + mgz_g\xi_5 - mgy_g\xi_6, 0) \qquad j = 4, 5, 6 \end{aligned} \tag{3.59}$$

where $j = 1, 2$ and 3 are for the force components in the x, y and z directions respectively, and $j = 4, 5$ and 6 are for the moments about the x, y and z axis respectively. (x_b, y_b, z_b)

are the coordinates of the center of buoyancy of the body. It is possible to express Eqn. 3.58 in terms of volume integrals by applying Gauss's theorem [55]. The resulting expression when added to the weight components of the hydrostatic force and moments in Eqn. 3.59, result in the total hydrostatic force and moment which can be written as

$$F_{hs_j} = (\rho\forall - m)g\delta_{j3} + (my_g - \rho\forall y_b)g\delta_{j4} - (mx_g - \rho\forall x_b)g\delta_{j5} - \sum_{k=1}^{6} c_{(j\ k)}\xi_k \tag{3.60}$$

where δ_{jk} is the Kroenecker delta function, equal to one if $j = k$, and zero otherwise. The term $c_{(j\ k)}$ in Eqn. 3.60 which is dependent on the motion of the body is known as the matrix of hydrostatic coefficients in this study. For an axi-symmetric body where off-diagonal hydrostatic terms are zero, the only nonzero elements of $c_{(j\ k)}$ are:

$$\begin{aligned} c_{(3\ 3)} &= \rho g S_w \\ c_{(4\ 4)} &= \rho g W_{22} + \rho g \forall z_b - mgz_g \\ c_{(5\ 5)} &= \rho g W_{11} + \rho g \forall z_b - mgz_g \end{aligned} \tag{3.61}$$

where S_w is the waterplane area, and W_{11} and W_{22} are the the waterplane area moments of inertia about the horizontal x and y axes respectively. For a free floating body in equilibrium ($\xi_j = 0$), the mass of the body must equal the displaced mass ($m = \rho\forall$) and the terms of zero-order in the body motions must vanish for an axi-symmetric body, since $y_g = y_b$ and $x_g = x_b$. The resulting nonzero hydrostatic force and moment coefficients are

$$\begin{aligned} c_{(3\ 3)} &= \rho g S_w \\ c_{(4\ 4)} &= \rho g \forall[(W_{22}/\forall) + z_b - z_g] = \rho g \forall GM_T \\ c_{(5\ 5)} &= \rho g \forall[(W_{11}/\forall) + z_b - z_g] = \rho g \forall GM_L \end{aligned} \tag{3.62}$$

where GM_T and GM_L are the transverse and longitudinal metacentric heights respectively. This is defined as the distance between the centre of gravity and the metacentre of the body.

3.4.5 Inertial force

The components of the inertial force F_{w_j}, associated with the acceleration of the body can be written in the form

$$F_{w_j} = \sum_{k=1}^{6} M_{jk}\ddot{\xi}_k \tag{3.63}$$

The inertia matrix M_{jk} in Eqn. 3.63 is associated with the mass of the body m, the center of gravity of the body (x_g, y_g, z_g), and the moments and products of inertia I_{jk}. For a floating body in a state of equilibrium in calm water, the inertia matrix is given by Newman [55] as

$$M_{jk} = \begin{bmatrix} m & 0 & 0 & 0 & mz_g & -my_g \\ 0 & m & 0 & -mz_g & 0 & mx_g \\ 0 & 0 & m & my_g & -mx_g & 0 \\ 0 & -mz_g & my_g & I_{xx} & I_{xy} & I_{xz} \\ mz_g & 0 & -mx_g & I_{yx} & I_{yy} & I_{yz} \\ -my_g & mx_g & 0 & I_{zx} & I_{zy} & I_{zz} \end{bmatrix} \tag{3.64}$$

3.5 General equations of motion for a WEC

The forces outlined in Section 3.4 are a set of generalised forces for floating bodies due to wave body interactions. Additional forces must be included when considering the wave body interactions of a floating WEC. Generally a power take off (PTO) is implemented into a WEC to extract energy from the relative motion of two or more parts of the WEC. Examples of different types of PTO systems include hydraulic systems and linear generators. The PTO force in the current analysis is modeled as a simple linear damper given by

$$F_{pto,j} = -B_{PTO_{jk}}\dot{\xi}_k \tag{3.65}$$

where $B_{PTO_{jk}}$ are the elements of the PTO damping matrix . A mooring system must also be included in the equation of motion for a WEC. Since nonlinear mooring modeling is beyond the scope of the study, it was decided to use a simple mooring system providing a linear stiffness, with the purpose of preventing the model from drifting. It should be noted

however, that the choice of mooring can introduce significant nonlinearities as outlined by Fitzgerald and Bergdahl [61], and in some cases can induce parametric resonance due to internal excitation [62]. The linear mooring is modelled as

$$F_{moor,j} = -k_{moor_{jk}} \Delta l \tag{3.66}$$

where $k_{moor_{jk}}$ are the elements of the linear stiffness matrix for the mooring system and $\Delta \boldsymbol{l}$ is the change in length in the mooring line from it's position in the static equilibrium position.

Based on the theory outline in Section 3.4 and including the additional PTO and mooring forces, the general equation of motion for a floating WEC with a linear damper PTO system and a linear stiffness mooring system can be expressed as

$$F_w = F_{FK} + F_d + F_r + F_{hs} + F_{pto} + F_{moor} \tag{3.67}$$

3.6 Numerical modelling of the Wavebob

As outlined in Chapter 2, the WEC designed by Wavebob is an axi-symmetric, self-reacting point absorber, that primarily operates in the heave mode. At the first stage in the numerical modelling of the Wavebob, the equations of motion will be applied to each individual body resulting in a 12 degree of freedom system. The next stage involves representing the interactions between the two bodies. To do so, it is assumed that the two bodies oscillate relative to each other only in the heave direction, while the two bodies are rigidly connected for the other modes of oscillation. This reduces the analysis to a system with 7 degrees of freedom corresponding to three rotations (roll, pitch, yaw) and two translations (surge, sway), plus two additional translations representing the heave motions of each body. The bodies are connected through the PTO system which is modelled as a linear damper, while a simple linear mooring system is used to prevent the device from drifting.

3.6.1 Coordinate frames and notation

The motion of each body is characterised by six oscillatory modes of motion as outlined in Table 3.1. The coordinate systems used to define the system dynamics are illustrated

in Fig. 3.3. An earth fixed frame $O_o x_o y_o z_o$ is assumed to be inertial and has it's origin at the still water level; it defines the position of the body axes as well as the incident of the waves. The individual axes of the earth fixed frame are $O_o x_o, O_o y_o$ and $O_o z_o$. The body fixed frames of body A and body B are denoted $O_A x_A y_A z_A$ and $O_B x_B y_B z_B$ respectively, and have their origin at the centre of gravity of the respective body; it defines the angular movement of the body with respect to the earth fixed frame. When describing the equations of motion, it is useful to refer to a general body axes frame as $O_j x_j y_j z_j$ which can refer to either the $O_A x_A y_A z_A$ frame or the $O_B x_B y_B z_B$ frame. An inertial translating frame $O_h x_h y_h z_h$ is fixed to the equilibrium state with it's vertical axes passing through the centre of gravity of the torus. The system is not fixed to the body with the $O_h z_h$ axis always perpendicular to the still water level. The notation for a vector expressed in a general frame is given by $\mathbf{r}^k = [x^k, y^k, z^k]^T$ while the unit vectors for a particular frame along the x, y and z axes are given by $\mathbf{i}^k, \mathbf{j}^k$ and $\mathbf{k}^k$ respectively (decomposed in frame k).

Mode No.	Mode Name	Mode No.	Mode Name
1	Torus surge	7	FNT surge
2	Torus sway	8	FNT sway
3	Torus heave	9	FNT heave
4	Torus roll	10	FNT roll
5	Torus pitch	11	FNT pitch
6	Torus yaw	12	FNT yaw

Table 3.1: 12 modes of oscillatory motion for the torus (body A) & FNT (body B)

3.6.2 Torus forces

As a first step, we consider each body independently from the other, with no PTO included in the analysis. It should be noted that any term with a subscript A refers to the torus, while a subscript B refers to the FNT. Applying Eqn. 3.67 to the torus and noting that $\mathbf{F}_{moor_A} = 0$ (as the mooring lines are all attached to the FNT) we can express the individual force acting on the torus as

$$F_{w_A} = \begin{bmatrix} m_A & 0 & 0 & 0 & m_A z_{g_A} & 0 \\ 0 & m_A & 0 & -m_A z_{g_A} & 0 & 0 \\ 0 & 0 & m_A & 0 & 0 & 0 \\ 0 & -m_A z_{g_A} & 0 & I_{xx_A} & 0 & 0 \\ m_A z_{g_A} & 0 & 0 & 0 & I_{yy_A} & 0 \\ 0 & 0 & 0 & 0 & 0 & I_{zz_A} \end{bmatrix} \begin{bmatrix} \ddot{\xi}_1 \\ \ddot{\xi}_2 \\ \ddot{\xi}_3 \\ \ddot{\xi}_4 \\ \ddot{\xi}_5 \\ \ddot{\xi}_6 \end{bmatrix} \tag{3.68}$$

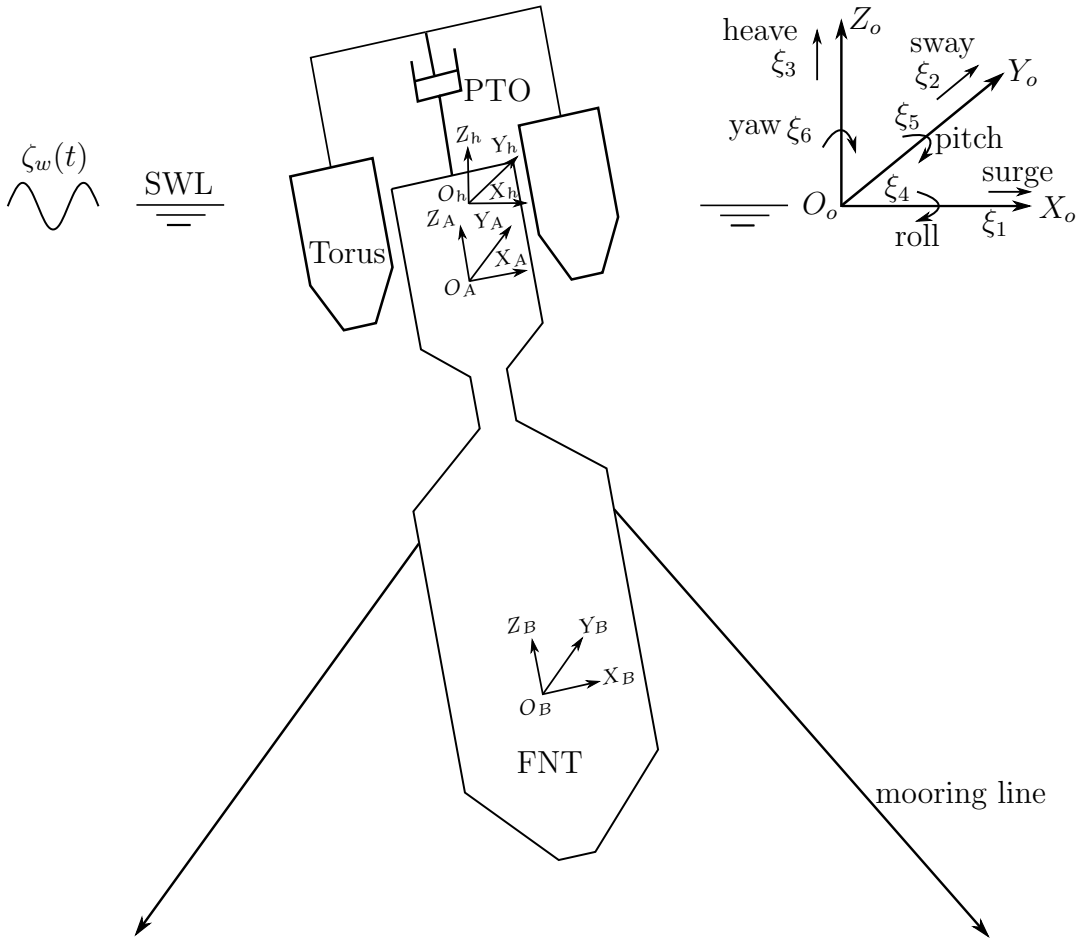

Figure 3.3: Schematic representation of Wavebob showing the torus (body A) and FNT (body B). Also shown are the body-fixed co-ordinate frames ($O_A x_A y_A z_A$ and $O_B x_B y_B z_B$), the earth fixed inertial frame ($O_o x_o y_o z_o$) and the translating inertial frame ($O_h x_h y_h z_h$)

where the products of inertia are zero due to the torus being axisymmetric. z_{g_A} is the vertical coordinate of the centre of gravity of the torus and $x_{g_A} = y_{g_A} = 0$

$$F_{r_A} = -\begin{bmatrix} a_{(1\ 1)} & 0 & 0 & 0 & a_{(1\ 5)} & 0 \\ 0 & a_{(2\ 2)} & 0 & a_{(2\ 4)} & 0 & 0 \\ 0 & 0 & a_{(3\ 3)} & 0 & 0 & 0 \\ 0 & a_{(4\ 2)} & 0 & a_{(4\ 4)} & 0 & 0 \\ a_{(5\ 1)} & 0 & 0 & 0 & a_{(5\ 5)} & 0 \\ 0 & 0 & 0 & 0 & 0 & a_{(6\ 6)} \end{bmatrix} \begin{bmatrix} \ddot{\xi}_1 \\ \ddot{\xi}_2 \\ \ddot{\xi}_3 \\ \ddot{\xi}_4 \\ \ddot{\xi}_5 \\ \ddot{\xi}_6 \end{bmatrix}$$

$$-\begin{bmatrix} \int_0^t K_{r_{(1\ 1)}}(t) & 0 & 0 & 0 & \int_0^t K_{r_{(1\ 5)}}(t) & 0 \\ 0 & \int_0^t K_{r_{(2\ 2)}}(t) & 0 & \int_0^t K_{r_{(2\ 4)}}(t) & 0 & 0 \\ 0 & 0 & \int_0^t K_{r_{(3\ 3)}}(t) & 0 & 0 & 0 \\ 0 & \int_0^t K_{r_{(4\ 2)}}(t) & 0 & \int_0^t K_{r_{(4\ 4)}}(t) & 0 & 0 \\ \int_0^t K_{r_{(5\ 1)}}(t) & 0 & 0 & 0 & \int_0^t K_{r_{(5\ 5)}}(t) & 0 \\ 0 & 0 & 0 & 0 & 0 & \int_0^t K_{r_{(6\ 6)}}(t) \end{bmatrix} \begin{bmatrix} \dot{\xi}_1 \\ \dot{\xi}_2 \\ \dot{\xi}_3 \\ \dot{\xi}_4 \\ \dot{\xi}_5 \\ \dot{\xi}_6 \end{bmatrix} \tag{3.69}$$

where $a_{(j\ k)}$ is the infinite frequency added mass in direction j due to an acceleration of the body in direction k. Due to the torus being axi-symmetric we have $a_{(1\ 1)} = a_{(2\ 2)}$, $a_{(4\ 4)} = a_{(5\ 5)}$ and $a_{(2\ 4)} = a_{(4\ 2)} = -a_{(1\ 5)} = -a_{(5\ 1)}$. Similarly, $K_{r_{(j\ k)}}(t)$ is the impulse response function in mode j due to an impulse in velocity in mode k. Note, the complete convolution term $\int_0^t K_{r_{(j\ k)}}(t-\tau)\dot{\xi}_k d\tau$, has been re-written $\int_0^t K_{r_{(j\ k)}}(t)\dot{\xi}_k$ throughout this chapter for convenience. A similar approach is taken for the excitation impulse response functions.

$$F_{d_A} = \begin{bmatrix} \int_{-t}^{t} K_{d_{(1)}}(t) & 0 & 0 & 0 & 0 & 0 \\ 0 & 0 & 0 & 0 & 0 & 0 \\ 0 & 0 & \int_{-t}^{t} K_{d_{(3)}}(t) & 0 & 0 & 0 \\ 0 & 0 & 0 & 0 & 0 & 0 \\ 0 & 0 & 0 & 0 & \int_{-t}^{t} K_{d_{(5)}}(t) & 0 \\ 0 & 0 & 0 & 0 & 0 & 0 \end{bmatrix} \begin{bmatrix} \zeta_w \\ \zeta_w \\ \zeta_w \\ \zeta_w \\ \zeta_w \\ \zeta_w \end{bmatrix} \tag{3.70}$$

$$F_{FK_A} = \begin{bmatrix} \int_{-t}^{t} K_{FK_{(1)}}(t) & 0 & 0 & 0 & 0 & 0 \\ 0 & 0 & 0 & 0 & 0 & 0 \\ 0 & 0 & \int_{-t}^{t} K_{FK_{(3)}}(t) & 0 & 0 & 0 \\ 0 & 0 & 0 & 0 & 0 & 0 \\ 0 & 0 & 0 & 0 & \int_{-t}^{t} K_{FK_{(5)}}(t) & 0 \\ 0 & 0 & 0 & 0 & 0 & 0 \end{bmatrix} \begin{bmatrix} \zeta_w \\ \zeta_w \\ \zeta_w \\ \zeta_w \\ \zeta_w \\ \zeta_w \end{bmatrix} \tag{3.71}$$

where it is noted that in regular head waves, there is only excitation in the surge, heave and pitch modes.

$$F_{hs_A} = - \begin{bmatrix} 0 & 0 & 0 & 0 & 0 & 0 \\ 0 & 0 & 0 & 0 & 0 & 0 \\ 0 & 0 & \rho g S_{w_A} & 0 & 0 & 0 \\ 0 & 0 & 0 & \rho g \forall_A GM_{T_A} & 0 & 0 \\ 0 & 0 & 0 & 0 & \rho g \forall_A GM_{L_A} & 0 \\ 0 & 0 & 0 & 0 & 0 & 0 \end{bmatrix} \begin{bmatrix} \xi_1 \\ \xi_2 \\ \xi_3 \\ \xi_4 \\ \xi_5 \\ \xi_6 \end{bmatrix} \tag{3.72}$$

Here S_{w_A} is the waterplane area of the torus, $\forall_A$ is the displaced volume of the torus and GM_{T_A} and GM_{L_A} are the transverse and longitudinal metacentric heights of the torus respectively.

3.6.3 FNT forces

The forces acting on the FNT can be expressed in a similar way by taking advantage of the axi-symmetric properties of the FNT.

$$F_{w_B} = \begin{bmatrix} m_B & 0 & 0 & 0 & m_B z_{g_B} & 0 \\ 0 & m_B & 0 & -m_B z_{g_B} & 0 & 0 \\ 0 & 0 & m_B & 0 & 0 & 0 \\ 0 & -m_B z_{g_B} & 0 & I_{xx_B} & 0 & 0 \\ m_B z_{g_B} & 0 & 0 & 0 & I_{yy_B} & 0 \\ 0 & 0 & 0 & 0 & 0 & I_{zz_B} \end{bmatrix} \begin{bmatrix} \ddot{\xi}_7 \\ \ddot{\xi}_8 \\ \ddot{\xi}_9 \\ \ddot{\xi}_{10} \\ \ddot{\xi}_{11} \\ \ddot{\xi}_{12} \end{bmatrix} \tag{3.73}$$

$$F_{r_B} = -\begin{bmatrix} a_{(7\ 7)} & 0 & 0 & 0 & a_{(7\ 11)} & 0 \\ 0 & a_{(8\ 8)} & 0 & a_{(8\ 10)} & 0 & 0 \\ 0 & 0 & a_{(9\ 9)} & 0 & 0 & 0 \\ 0 & a_{(10\ 8)} & 0 & a_{(10\ 10)} & 0 & 0 \\ a_{(11\ 7)} & 0 & 0 & 0 & a_{(11\ 11)} & 0 \\ 0 & 0 & 0 & 0 & 0 & a_{(12\ 12)} \end{bmatrix} \begin{bmatrix} \ddot{\xi}_7 \\ \ddot{\xi}_8 \\ \ddot{\xi}_9 \\ \ddot{\xi}_{10} \\ \ddot{\xi}_{11} \\ \ddot{\xi}_{12} \end{bmatrix}$$

$$- \begin{bmatrix} \int_0^t K_{r_{(7\ 7)}}(t) & 0 & 0 & 0 & \int_0^t K_{r_{(7\ 11)}}(t) & 0 \\ 0 & \int_0^t K_{r_{(8\ 8)}}(t) & 0 & \int_0^t K_{r_{(8\ 10)}}(t) & 0 & 0 \\ 0 & 0 & \int_0^t K_{r_{(9\ 9)}}(t) & 0 & 0 & 0 \\ 0 & \int_0^t K_{r_{(10\ 8)}}(t) & 0 & \int_0^t K_{r_{(10\ 10)}}(t) & 0 & 0 \\ \int_0^t K_{r_{(11\ 7)}}(t) & 0 & 0 & 0 & \int_0^t K_{r_{(11\ 11)}}(t) & 0 \\ 0 & 0 & 0 & 0 & 0 & \int_0^t K_{r_{(12\ 12)}}(t) \end{bmatrix} \begin{bmatrix} \dot{\xi}_7 \\ \dot{\xi}_8 \\ \dot{\xi}_9 \\ \dot{\xi}_{10} \\ \dot{\xi}_{11} \\ \dot{\xi}_{12} \end{bmatrix} \tag{3.74}$$

$$F_{d_B} = \begin{bmatrix} \int_{-t}^t K_{d_{(7)}}(t) & 0 & 0 & 0 & 0 & 0 \\ 0 & 0 & 0 & 0 & 0 & 0 \\ 0 & 0 & \int_{-t}^t K_{d_{(9)}}(t) & 0 & 0 & 0 \\ 0 & 0 & 0 & 0 & 0 & 0 \\ 0 & 0 & 0 & 0 & \int_{-t}^t K_{d_{(11)}}(t) & 0 \\ 0 & 0 & 0 & 0 & 0 & 0 \end{bmatrix} \begin{bmatrix} \zeta_w \\ \zeta_w \\ \zeta_w \\ \zeta_w \\ \zeta_w \\ \zeta_w \end{bmatrix} \tag{3.75}$$

$$F_{FK_B} = \begin{bmatrix} \int_{-t}^t K_{FK_{(7)}}(t) & 0 & 0 & 0 & 0 & 0 \\ 0 & 0 & 0 & 0 & 0 & 0 \\ 0 & 0 & \int_{-t}^t K_{FK_{(9)}}(t) & 0 & 0 & 0 \\ 0 & 0 & 0 & 0 & 0 & 0 \\ 0 & 0 & 0 & 0 & \int_{-t}^t K_{FK_{(11)}}(t) & 0 \\ 0 & 0 & 0 & 0 & 0 & 0 \end{bmatrix} \begin{bmatrix} \zeta_w \\ \zeta_w \\ \zeta_w \\ \zeta_w \\ \zeta_w \\ \zeta_w \end{bmatrix} \tag{3.76}$$

$$F_{hs_B} = -\begin{bmatrix} 0 & 0 & 0 & 0 & 0 & 0 \\ 0 & 0 & 0 & 0 & 0 & 0 \\ 0 & 0 & \rho g S_{w_B} & 0 & 0 & 0 \\ 0 & 0 & 0 & \rho g \forall_B G M_{T_B} & 0 & 0 \\ 0 & 0 & 0 & 0 & \rho g \forall_B G M_{L_B} & 0 \\ 0 & 0 & 0 & 0 & 0 & 0 \end{bmatrix} \begin{bmatrix} \xi_7 \\ \xi_8 \\ \xi_9 \\ \xi_{10} \\ \xi_{11} \\ \xi_{12} \end{bmatrix} \tag{3.77}$$

$$F_{moor_B} = \begin{bmatrix} -k_{moor_B} \Delta l_x \\ -k_{moor_B} \Delta l_y \\ -k_{moor_B} \Delta l_z \\ (r_m^h \times F_{moor_B})_x \\ (r_m^h \times F_{moor_B})_y \\ (r_m^h \times F_{moor_B})_z \end{bmatrix} \tag{3.78}$$

where k_{moor_B} is the linear mooring stiffness coefficient and Δl_x, Δl_y and Δl_z are the change in lengths of the mooring lines in the x, y and z directions respectively. The mooring

moments are calculated as the cross product of the position vector $\mathbf{r}_m^h$ (the position vector of the point of attachment of the mooring line to the FNT) with the mooring force F_{moor_B}, represented in the $O_h x_h y_h z_h$ frame.

3.6.4 Linear equations of motion for 7 degrees of freedom

To analyse the hydrodynamic interaction between the bodies it is necessary to include the hydrodynamic coupling between the different modes of motion. Considering a 7 degree of freedom system with each body allowed to oscillate relative to the other in the heave direction only, the mass matrix M can be written

$$M = \begin{bmatrix} m_t & 0 & 0 & 0 & 0 & m_t z_g & 0 \\ 0 & m_t & 0 & 0 & -m_t z_g & 0 & 0 \\ 0 & 0 & m_A & 0 & 0 & 0 & 0 \\ 0 & 0 & 0 & m_B & 0 & 0 & 0 \\ 0 & -m_t z_g & 0 & 0 & I_{xx_t} & 0 & 0 \\ m_t z_g & 0 & 0 & 0 & 0 & I_{yy_t} & 0 \\ 0 & 0 & 0 & 0 & 0 & 0 & I_{zz_t} \end{bmatrix} \tag{3.79}$$

Here $m_t = m_A + m_B$ is the total mass of the system, I_{xx_t}, I_{yy_t} and I_{zz_t} are the total moments of inertia of the system of two bodies about the respective axes, with $I_{xx_t} = I_{yy_t}$ due to symmetry. z_g is the vertical coordinate of the centre of gravity of the system.
The infinite frequency added mass matrix $a(\infty)$ output from WAMIT for a two body system, is a 12×12 matrix which includes the added mass for each body along with the coupled added mass terms for the two body system. This can be reduced to a 7×7 matrix as

$$a(\infty) = \begin{bmatrix} a_{1,1} & 0 & 0 & 0 & 0 & a_{1,6} & 0 \\ 0 & a_{2,2} & 0 & 0 & a_{2,5} & 0 & 0 \\ 0 & 0 & a_{3,3} & 0 & 0 & 0 & 0 \\ 0 & 0 & 0 & a_{4,4} & 0 & 0 & 0 \\ 0 & a_{5,2} & 0 & 0 & a_{5,5} & 0 & 0 \\ a_{6,1} & 0 & 0 & 0 & 0 & a_{6,6} & 0 \\ 0 & 0 & 0 & 0 & 0 & 0 & a_{7,7} \end{bmatrix} \tag{3.80}$$

where $a_{j,k}$ refers to the the index of the matrix and not to the mode of motion. For example, $a_{1,6}$ is the entry in the first row and sixth column of $a(\infty)$. The nonzero entries

are computed as

$$
\begin{aligned}
a_{1,1} &= a_{(1\ 1)} + a_{(1\ 7)} + a_{(7\ 1)} + a_{(7\ 7)} \\
a_{1,6} &= a_{(1\ 5)} + a_{(1\ 11)} + a_{(7\ 5)} + a_{(7\ 11)} \\
a_{2,2} &= a_{(2\ 2)} + a_{(2\ 8)} + a_{(8\ 2)} + a_{(8\ 8)} \\
a_{2,5} &= a_{(2\ 4)} + a_{(2\ 10)} + a_{(8\ 4)} + a_{(8\ 10)} \\
a_{3,3} &= a_{(3\ 3)} + a_{(3\ 9)} \\
a_{4,4} &= a_{(9\ 9)} + a_{(9\ 3)} \\
a_{5,2} &= a_{(4\ 2)} + a_{(4\ 8)} + a_{(10\ 2)} + a_{(10\ 8)} \\
a_{5,5} &= a_{(4\ 4)} + a_{(4\ 10)} + a_{(10\ 4)} + a_{(10\ 10)} \\
a_{6,1} &= a_{(5\ 1)} + a_{(5\ 7)} + a_{(11\ 1)} + a_{(11\ 7)} \\
a_{6,6} &= a_{(5\ 5)} + a_{(5\ 11)} + a_{(11\ 5)} + a_{(11\ 11)} \\
a_{7,7} &= a_{(6\ 6)} + a_{(6\ 12)} + a_{(12\ 6)} + a_{(12\ 12)}
\end{aligned}
\tag{3.81}
$$

Similar to the 12 degree of freedom case, $a_{(j\ k)}$ refers to the added mass in mode j due to an acceleration in mode k. For example, the entry $a_{1,6}$ of the matrix is equal to $a_{(1\ 5)} + a_{(1\ 11)} + a_{(7\ 5)} + a_{(7\ 11)}$. Here, $a_{(1\ 5)}$ is the added mass of the torus in the surge mode (*mode 1*) due to an acceleration of the torus in the pitch mode (*mode 5*). $a_{(1\ 11)}$ is the added mass of the torus in the surge mode (*mode 1*) due to an acceleration of the FNT in the pitch mode (*mode 11*). $a_{(7\ 5)}$ is the added mass of the FNT in the surge mode (*mode 7*) due to an acceleration of the torus in the pitch mode (*mode 5*). $a_{(7\ 11)}$ is the added mass of the FNT in the surge mode (*mode 7*) due to an acceleration of the FNT in the pitch mode (*mode 11*).

The PTO in the 7 degree of freedom system is modelled as a linear damper which only

provides a damping force in the heave mode of each body. The PTO force for each individual body can be expressed as

$$F_{PTO_A} = -B_{PTO}\begin{bmatrix} 0 \\ 0 \\ (\dot{\xi}_3 - \dot{\xi}_9) \\ 0 \\ 0 \\ 0 \end{bmatrix} \qquad F_{PTO_B} = B_{PTO}\begin{bmatrix} 0 \\ 0 \\ (\dot{\xi}_3 - \dot{\xi}_9) \\ 0 \\ 0 \\ 0 \end{bmatrix} \tag{3.82}$$

where B_{PTO} is the PTO damping coefficient. The resulting 7 degree of freedom linear equations of motion can therefore be written as

$$\begin{bmatrix} m_t + a_{1,1} & 0 & 0 & 0 & 0 & m_t z_g + a_{1,6} & 0 \\ 0 & m_t + a_{2,2} & 0 & 0 & -m_t z_g + a_{2,5} & 0 & 0 \\ 0 & 0 & m_A + a_{3,3} & 0 & 0 & 0 & 0 \\ 0 & 0 & 0 & m_B + a_{4,4} & 0 & 0 & 0 \\ 0 & -m_t z_g + a_{5,2} & 0 & 0 & I_{xx_t} + a_{5,5} & 0 & 0 \\ m_t z_g + a_{6,1} & 0 & 0 & 0 & 0 & I_{yy_t} + a_{6,6} & 0 \\ 0 & 0 & 0 & 0 & 0 & 0 & I_{zz_t} + a_{7,7} \end{bmatrix} \begin{bmatrix} \ddot{\xi}_1 \\ \ddot{\xi}_2 \\ \ddot{\xi}_3 \\ \ddot{\xi}_9 \\ \ddot{\xi}_4 \\ \ddot{\xi}_5 \\ \ddot{\xi}_6 \end{bmatrix}$$

$$= \begin{bmatrix} F_{FK_{A,1}} + F_{d_{A,1}} + F_{hs_{A,1}} + F_{r_{A,1}} + F_{FK_{B,1}} + F_{d_{B,1}} + F_{hs_{B,1}} + F_{r_{B,1}} + F_{moor_{B,1}} \\ F_{FK_{A,2}} + F_{d_{A,2}} + F_{hs_{A,2}} + F_{r_{A,2}} + F_{FK_{B,2}} + F_{d_{B,2}} + F_{hs_{B,2}} + F_{r_{B,2}} + F_{moor_{B,2}} \\ F_{FK_{A,3}} + F_{d_{A,3}} + F_{hs_{A,3}} + F_{r_{A,3}} + F_{PTO_{A,3}} \\ F_{FK_{B,9}} + F_{d_{B,9}} + F_{hs_{B,9}} + F_{r_{B,9}} + F_{PTO_{B,9}} + F_{moor_{B,9}} \\ F_{FK_{A,4}} + F_{d_{A,4}} + F_{hs_{A,4}} + F_{r_{A,4}} + F_{FK_{B,4}} + F_{d_{B,4}} + F_{hs_{B,4}} + F_{r_{B,4}} + F_{moor_{B,4}} \\ F_{FK_{A,5}} + F_{d_{A,5}} + F_{hs_{A,5}} + F_{r_{A,5}} + F_{FK_{B,5}} + F_{d_{B,5}} + F_{hs_{B,5}} + F_{r_{B,5}} + F_{moor_{B,5}} \\ F_{FK_{A,6}} + F_{d_{A,6}} + F_{hs_{A,6}} + F_{r_{A,6}} + F_{FK_{B,6}} + F_{d_{B,6}} + F_{hs_{B,6}} + F_{r_{B,6}} + F_{moor_{B,6}} \end{bmatrix} \tag{3.83}$$

where the subscript A refer to the forces and moments of the torus and the subscript B refer to the forces and moments of the FNT. The numeric subscripts in the matrix on the right hand side of Eqn. 3.83 refer to the mode with which the forces and moments are associated with according to Table 3.1. For example, $F_{FK_{A,3}}$ refers to the Froude-Krylov excitation force of the torus in the torus heave mode (*mode 3*) and $F_{FK_{B,9}}$ refers to the Froude-Krylov excitation force of the FNT in the FNT heave mode (*mode 9*).

3.7 Nonlinear equations of motion

It is common for a heaving point absorber WEC to operate while resonating in heave in order to maximize the power absorbed by the PTO. Thus, in order to maximise power output in the case of Wavebob, it is required to have a large relative heave motion, as this is the mode in which power is absorbed for the considered WEC. Due to the large

amplitude motions, there will potentially be nonlinear coupling among the longitudinal and lateral modes, which cannot be modelled using a fully linear model. Furthermore, it is known from experimental testing that the Wavebob is prone to parametric instabilities under certain wave conditions. This can result in large roll and pitch motions resulting from parametric motion which is inherently a nonlinear phenomenon.

In order to accurately represent the system dynamics of the nonlinear system, it is therefore necessary to use an approach whereby the dynamic and hydrostatic pressure due to the undisturbed incident wave is integrated over the time varying wetted surface, i.e., the instantaneous wetted surface of the body. This results in nonlinear hydrostatic restoring forces and nonlinear Froude-Krylov excitation forces, while the linear representation of the diffraction and radiation forces remain in the analysis.

Referring to Fig. 3.3, the nonlinear equations of motion are integrated in the body axes frames $O_A x_A y_A z_A$ and $O_B x_B y_B z_B$ of the torus and FNT respectively. Since the nonlinear Froude-Krylov and hydrostatic forces depend on the instantaneous position of the incident wave, these forces must first be calculated in the $O_h x_h y_h z_h$ frame, as the incidence of the wave is described in this frame relative to the fixed inertial frame $O_o x_o y_o z_o$. It is therefore necessary to transform these forces from the $O_h x_h y_h z_h$ frame to the body axes frames using a suitable frame transformation in order to integrate the equations of motion. When translating the equations of motion from the the translating $O_h x_h y_h z_h$ frame to the rotating body fixed frames, Coriolis forces between the two frames appear which must also be included in the equations of motion.

3.7.1 Nonlinear drag

A drag force has been included in the numerical model to approximate the energy losses due to viscosity. As pointed out by Haslum and Faltinsen [49], the linear damping assumption is not a sufficient approximation when large response amplitudes occur, which often is the case for point absorbers which are prone to large amplitude motions due to parametric resonance. Due to the large amplitude motions of the device, it is assumed that viscous damping is the main source of nonlinear damping for the Wavebob point absorber. For this reason, a quadratic damping term has been included which can be

written for degree of freedom j as

$$F_{drag,j} = -0.5\rho C_{d_{jk}} A(\dot{\xi}_k)^2 \tag{3.84}$$

where $C_{d_{jk}}$ is element jk of the matrix of drag coefficients and A is the frontal area of the body. Estimates for the drag coefficient in the heave, roll and pitch modes are based on the experimental free decay tests of the locked body. This will be explained further in Section 4.4.

3.7.2 Nonlinear Froude-Krylov force and hydrostatic restoring force

The Froude-Krylov excitation forces and moments are the loads introduced by the pressure field generated by undisturbed waves. In linear theory, the pressure is integrated over the surface of the body at the mean water level with the body in it's equilibrium position. This method is suitable for small amplitude waves, however, when the device undergoes large amplitude motions due to resonance conditions and/or large amplitude waves for example, there can be a significant change in wetted surface area and wave profile with time. Therefore, the large amplitude motion of the WEC introduces a nonlinear relationship between the pressure acting on the surface of the body due to the undisturbed wave, and the body displacements. In this model, the Froude-Krylov forces are related to the motion of the WEC, as the pressure of the undisturbed incident wave is integrated over the instantaneous wetted surface $S_b(t)$, of the body, which changes with time. With respect to the general body axes frame $O_j x_j y_j z_j$, nonlinear Froude-Krylov dynamic excitation forces and moments may be expressed as

$$F_{FK_d} = \int\int_{S_b(t)} p_d \begin{bmatrix} \mathbf{m}_i^j \\ \mathbf{r}_i^j \times \mathbf{m}_i^j \end{bmatrix} dS \tag{3.85}$$

where $\mathbf{r}_i^j$ is the position vector of wetted panel i with surface area dS expressed in the general body fixed frame $O_j x_j y_j z_j$, and $\mathbf{m}_i^j$ is the unit normal vector pointing outward of the same panel with components n_x^j, n_y^j and n_z^j. The dynamic pressure p_d of the incident wave is obtained from the linear hydrodynamic part of Eqn. 3.10 as

$$p_d = -\rho \frac{\partial \phi_i}{\partial t} \tag{3.86}$$

where the deep water incident wave potential is obtained from Eqn. 3.20.

Similar to the Froude-Krylov excitation forces, the hydrostatic restoring force is nonlinear, as it is also calculated over the time-varying instantaneous wetted surface of the body. The hydrostatic pressure force and the gravity force form the nonlinear Froude-Krylov static force which is expressed in the general body fixed frame $O_j x_j y_j z_j$ as

$$F_{FK_s} = \int\int_{S_b(t)} p_s \begin{bmatrix} \mathbf{m}_i^j \\ \mathbf{r}_i^j \times \mathbf{m}_i^j \end{bmatrix} dS - mg \begin{bmatrix} \mathbf{k}^j \\ \mathbf{r}_g^j \times \mathbf{k}^j \end{bmatrix} \tag{3.87}$$

Here, the first term represents the hydrostatic force and the second term represents the forces due to the weight of the body. $\mathbf{r}_g^j$ is the position vector of the centre of gravity in the body fixed frame $O_j x_j y_j z_j$ frame and $\mathbf{k}^j$ is the unit vector along the $O_j z$ axis in the $O_j x_j y_j z_j$ frame. Note that the gravity force changes direction with time in the body fixed frame since the unit vector $\mathbf{k}^j$ moves with the body fixed frame $O_j x_j y_j z_j$. However, the direction of the gravity force in the inertial frame is a constant, i.e. $\mathbf{k}^o = [0, 0, 1]^T$, where $\mathbf{k}^o$ is the unit vector in the z direction in the earth fixed frame.

The hydrostatic pressure p_s at a depth z is obtained from the hydrostatic part of Eqn. 3.10 as

$$p_s = -\rho g z \tag{3.88}$$

The nonlinear equations of motion can therefore be expressed as

$$F_w + F_c = F_{FK_d} + F_d + F_r + F_{FK_s} + F_{pto} + F_{moor} + F_{drag} \tag{3.89}$$

where F_c refers to the Coriolis forces which can be written following the methods of Fossen [63] as

$$F_c = \begin{bmatrix} m_t(-\dot{\xi}_2\dot{\xi}_6) + m_A(\dot{\xi}_3\dot{\xi}_5) + m_B(\dot{\xi}_9\dot{\xi}_5) \\ m_t(\dot{\xi}_1\dot{\xi}_6) - m_A(\dot{\xi}_3\dot{\xi}_4) - m_B(\dot{\xi}_9\dot{\xi}_4) \\ m_A(-\dot{\xi}_1\dot{\xi}_5 + \dot{\xi}_2\dot{\xi}_4) \\ m_B(-\dot{\xi}_1\dot{\xi}_5 + \dot{\xi}_2\dot{\xi}_4) \\ (I_{zz_t} - I_{yy_t})\dot{\xi}_5\dot{\xi}_6 \\ (I_{xx_t} - I_{zz_t})\dot{\xi}_6\dot{\xi}_4 \\ (I_{yy_t} - I_{xx_t})\dot{\xi}_4\dot{\xi}_5 \end{bmatrix} \tag{3.90}$$

Rewriting Eqn. 3.89 in matrix form results in

$$
\begin{bmatrix}
m_t + a_{1,1} & 0 & 0 & 0 & 0 & m_t z_g + a_{1,6} & 0 \\
0 & m_t + a_{2,2} & 0 & 0 & -m_t z_g + a_{2,5} & 0 & 0 \\
0 & 0 & m_A + a_{3,3} & 0 & 0 & 0 & 0 \\
0 & 0 & 0 & m_B + a_{4,4} & 0 & 0 & 0 \\
0 & -m_t z_g + a_{5,2} & 0 & 0 & I_{xx_t} + a_{5,5} & 0 & 0 \\
m_t z_g + a_{6,1} & 0 & 0 & 0 & 0 & I_{yy_t} + a_{6,6} & 0 \\
0 & 0 & 0 & 0 & 0 & 0 & I_{zz_t} + a_{7,7}
\end{bmatrix}
\begin{bmatrix}
\ddot{\xi}_1 \\ \ddot{\xi}_2 \\ \ddot{\xi}_3 \\ \ddot{\xi}_9 \\ \ddot{\xi}_4 \\ \ddot{\xi}_5 \\ \ddot{\xi}_6
\end{bmatrix}
$$

$$
+
\begin{bmatrix}
m_t(-\dot{\xi}_2\dot{\xi}_6) + m_A(\dot{\xi}_3\dot{\xi}_5) + m_B(\dot{\xi}_9\dot{\xi}_5) \\
m_t(\dot{\xi}_1\dot{\xi}_6) - m_A(\dot{\xi}_3\dot{\xi}_4) - m_B(\dot{\xi}_9\dot{\xi}_4) \\
m_A(-\dot{\xi}_1\dot{\xi}_5 + \dot{\xi}_2\dot{\xi}_4) \\
m_B(-\dot{\xi}_1\dot{\xi}_5 + \dot{\xi}_2\dot{\xi}_4) \\
(I_{zz_t} - I_{yy_t})\dot{\xi}_5\dot{\xi}_6 \\
(I_{xx_t} - I_{zz_t})\dot{\xi}_6\dot{\xi}_4 \\
(I_{yy_t} - I_{xx_t})\dot{\xi}_4\dot{\xi}_5
\end{bmatrix}
\tag{3.91}
$$

$$
=
\begin{bmatrix}
F_{FK_{d_{A,1}}} + F_{d_{A,1}} + F_{FK_{s_{A,1}}} + F_{r_{A,1}} + F_{drag_{A,1}} + F_{FK_{d_{B,1}}} + F_{d_{B,1}} + F_{FK_{s_{B,1}}} + F_{r_{B,1}} + F_{drag_{B,1}} + F_{moor_{B,1}} \\
F_{FK_{d_{A,2}}} + F_{d_{A,2}} + F_{FK_{s_{A,2}}} + F_{r_{A,2}} + F_{drag_{A,2}} + F_{FK_{d_{B,2}}} + F_{d_{B,2}} + F_{FK_{s_{B,2}}} + F_{r_{B,2}} + F_{drag_{B,2}} + F_{moor_{B,2}} \\
F_{FK_{d_{A,3}}} + F_{d_{A,3}} + F_{FK_{s_{A,3}}} + F_{r_{A,3}} + F_{PTO_{A,3}} + F_{drag_{A,3}} \\
F_{FK_{d_{B,9}}} + F_{d_{B,9}} + F_{FK_{s_{B,9}}} + F_{r_{B,9}} + F_{PTO_{B,9}} + F_{moor_{B,9}} + F_{drag_{B,9}} \\
F_{FK_{d_{A,4}}} + F_{d_{A,4}} + F_{FK_{s_{A,4}}} + F_{r_{A,4}} + F_{drag_{A,4}} + F_{FK_{d_{B,4}}} + F_{d_{B,4}} + F_{FK_{s_{B,4}}} + F_{r_{B,4}} + F_{drag_{B,4}} + F_{moor_{B,4}} \\
F_{FK_{d_{A,5}}} + F_{d_{A,5}} + F_{FK_{s_{A,5}}} + F_{r_{A,5}} + F_{drag_{A,5}} + F_{FK_{d_{B,5}}} + F_{d_{B,5}} + F_{FK_{s_{B,5}}} + F_{r_{B,5}} + F_{drag_{B,5}} + F_{moor_{B,5}} \\
F_{FK_{d_{A,6}}} + F_{d_{A,6}} + F_{FK_{s_{A,6}}} + F_{r_{A,6}} + F_{drag_{A,6}} + F_{FK_{d_{B,6}}} + F_{d_{B,6}} + F_{FK_{s_{B,6}}} + F_{r_{B,6}} + F_{drag_{B,6}} + F_{moor_{B,6}}
\end{bmatrix}
$$

This chapter has presented a framework for extending a linear model to a nonlinear model for the purpose of accurately representing the system dynamics of a heaving point absorber WEC. A nonlinear analysis is deemed necessary in the current work due to the large amplitude motions which a point absorber WEC is prone to, due to operating in parametric resonance conditions and/or due to large amplitude waves. Due to the large amplitude motions, the wetted surface of the body will not be constant with time, as is assumed in a fully linear model. There will in fact be a nonlinear relationship between the motion of the device and the instantaneous wetted surface (due to the incident wave) which changes with time in the nonlinear model. For this reason, the nonlinear Froude-Krylov excitation forces and nonlinear hydrostatic restoring forces are integrated on the instantaneous time-varying wetted surface in the current work.

Furthermore, in a linear model, a small angle approximation is used in the rotation matrices, as it is assumed that the body rotations are small about the inertial fixed frame. This is not the case in the nonlinear model presented in this work, as it is known that a point absorber is prone to nonlinear parametric instabilities, resulting in large amplitude roll and pitch motions which makes a small angle approximation to be invalid. For these reasons, a linear model will not be able to accurately predict the motion responses of a point absorber WEC undergoing large amplitude motions, and it will not be able to capture parametric motion which is an inherently nonlinear phenomenon.

Chapter 5 presents the results from the linear hydrodynamic analysis performed in WAMIT, resulting in the linear radiation damping and added mass coefficients and also the diffraction components of the total excitation force as explained in Section 3.4. The results for the analysis of the nonlinear numerical model are presented for regular waves and irregular in Chapter 6 and 7 respectively, with comparisons being made with experimental data in regular waves in order to validate the model.

Chapter 4

SML17 experimental model

4.1 Introduction

A wave tank testing campaign was carried out by the Wavebob engineering team at École Centrale de Nantes (ECN) in June 2010. The main goals of the test campaign were to:

• create an experimental power matrix;

• test the stability of the device and investigate the phenomenon of parametric motion and it's influence on the mechanical power absorbed;

• validate the numerical code.

A 1:17 scale model known hereinafter as SML17 was constructed for the tests. The model was equipped with a power take off (PTO) for damping the relative motion and to enable the team to realise an empirical power assessment.

4.2 Experimental test arrangement

4.2.1 The École Centrale de Nantes test tank

The tank at ECN, as shown in Fig. 4.1, is 50m long and 30m wide, with a constant depth of 5m. There is also a pit in the centre of the tank which measures 5m × 5m with an additional 5m depth. A multiflap wavemaker with 48 individual flaps allows to create multidirectional waves up to 1m in height. Two bridges span the tank which are used for camera equipment and device inspection. Access to the device is made possible with a small inflatable boat. A picture of the ECN wave tank with the SML17 model in the tank is shown in Fig. 4.2.

During the tests, data was collected using two different systems. The National Instruments

compact RIO (cRIO) controller on board the SML17 device was used for acquiring data from the accelerometers and linear position sensors installed on the model. They were also used to log force measurements in the PTO and mooring system amongst others. Wave elevation and body motions were captured using an optical tracking system available at ECN.

Figure 4.1: The École Centrale de Nantes wave tank [64]

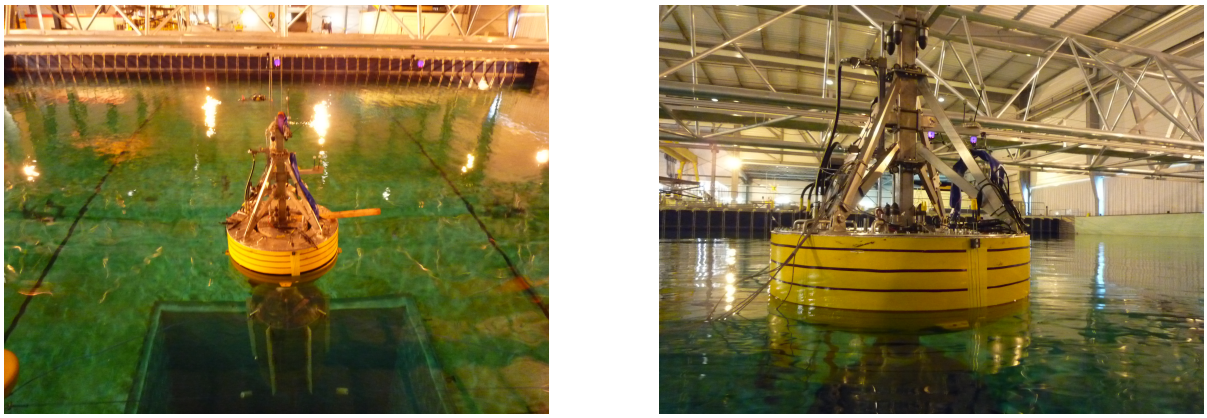

Figure 4.2: SML17 model at École Centrale de Nantes testing facility

4.2.2 Mooring

The model was moored by three mooring assemblies to the bottom of the basin as shown in Fig. 4.3. Each mooring assembly utilises a sub-surface buoy which is connected to

the model via a top line and a bridle line. The sub-surface buoys provide buoyancy and also provide a restoring force when the system is displaced. The sub-surface buoys are connected to an anchor block on the floor of the tank by an anchor line.

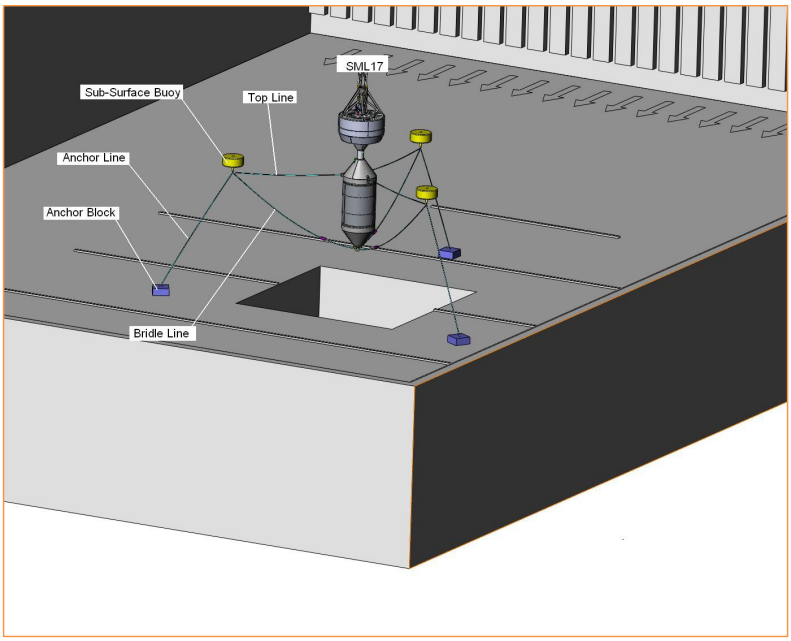

(a) 3D image of the SML17 mooring assembly

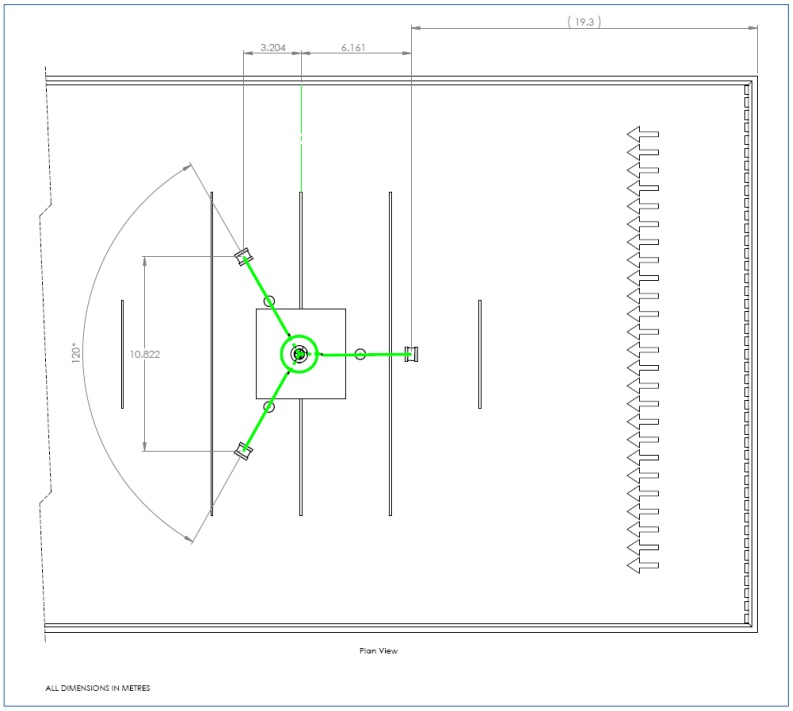

(b) plan view of the SML17 mooring assembly

Figure 4.3: SML17 mooring arrangement

4.3 SML17 configuration

The SML17 model was drawn up in SolidWorks (Fig. 4.4) to allow for the device to be manufactured. The SolidWorks model was also used to provide initial estimates of the mass properties of the device which are outlined in Table 4.1 - 4.3. The materials chosen for the manufacturing of the torus, FNT and sub-assemblies, along with the dimensions of all of the parts, determine the distributions of mass of the system. The main dimensions of SML17 are shown in Fig. 4.5. The dimensions of the model are defined in relation to a coordinate system with $Z = 0$ in the plane of the still waterline, and the Z-axis positive upwards as shown in Fig. 4.5. The still waterline is a predefined parameter when designing the model. The mass distribution and volume of the overall system must be chosen such that the still waterline is in the desired position. It can also be seen in Fig. 4.5 that the torus and FNT are separated by a small gap of width 60mm. This small gap is known as a moonpool in this study and will be explained further in Section 5.1.

Property	Unit	Magnitude
Mass	kg	306
Moment of inertia I_{xx}	kgm^2	85
Moment of inertia I_{yy}	kgm^2	85
Moment of inertia I_{zz}	kgm^2	68
Centre of gravity above waterline	m	0.12
Centre of buoyancy above waterline	m	0.17

Table 4.1: Mass properties of the torus

Property	Unit	Magnitude
Mass	kg	1427
Moment of inertia I_{xx}	kgm^2	8162
Moment of inertia I_{yy}	kgm^2	8162
Moment of inertia I_{zz}	kgm^2	124
Centre of gravity above waterline	m	-2.223
Centre of buoyancy above waterline	m	-2.025

Table 4.2: Mass properties of the FNT

Property	Unit	Magnitude
Mass	kg	1735
Moment of inertia I_{xx}	kgm^2	8227
Moment of inertia I_{yy}	kgm^2	8227
Moment of inertia I_{zz}	kgm^2	196
Centre of gravity above waterline	m	-1.82
Centre of buoyancy above waterline	m	-1.72

Table 4.3: Mass properties of the torus & FNT combined

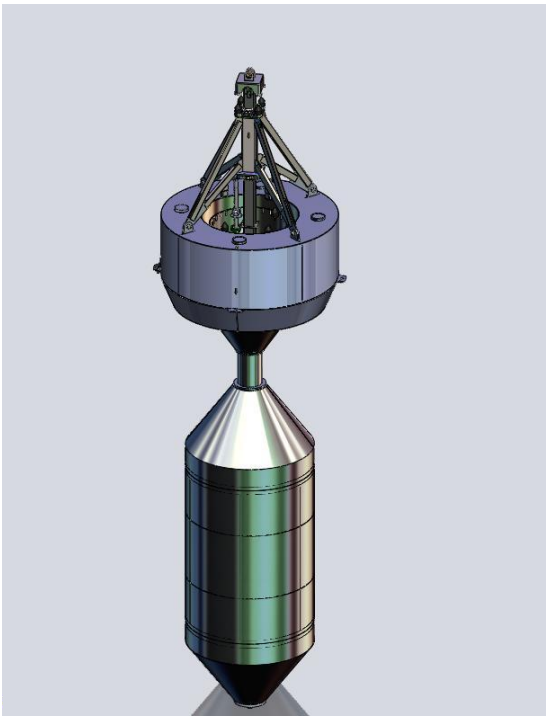

Figure 4.4: SML17 SolidWorks model [21]

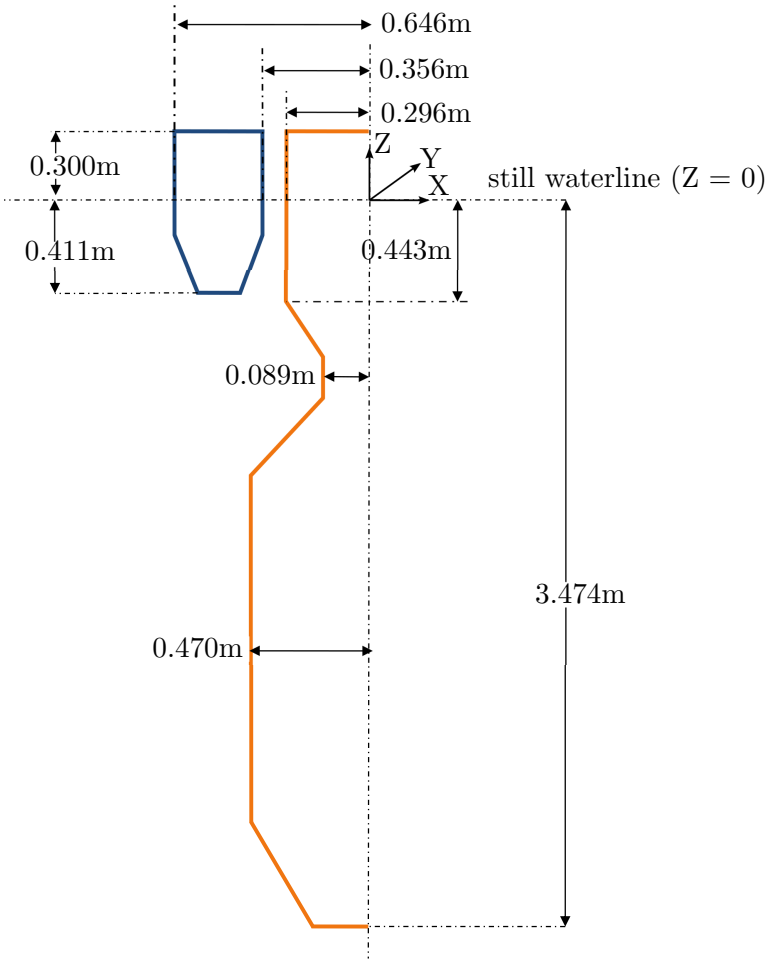

Figure 4.5: Main dimensions of SML17

4.4 Free decay tests

Heave and pitch free decay tests were performed with the mooring system attached in order to determine the natural frequencies of the model. For these tests the model was locked, so that there was no relative motion between the torus and the FNT. The device therefore behaved as a single body. This was achieved by providing an "infinite damping" to the PTO system. The free decay tests were also useful for gaining an insight into the level of damping in the heave and pitch degrees of freedom. It would have been beneficial to have separated the torus and FNT from each other, and to have performed free decay tests for each individual body on their own in the water, as it would then be possible to estimate a separate damping coefficient for each body using system identification methods. This damping coefficient could then be easily implemented into the nonlinear numerical

simulations when calculating the drag forces on each individual body. Although the free decay tests were performed on the locked body, it was still possible to get an idea of the order of magnitude of the damping so that a damping coefficient for each body could be estimated for use in the numerical simulations.

The heave and pitch free decay tests are illustrated in Fig. 4.6 and 4.7 respectively. Also shown in these figures are the frequency domain spectra for each test, with the corresponding natural frequencies calculated from the analysis given in Table 4.4.

The heave time trace in Fig. 4.6(a) resembles a typical single degree of freedom free decay test, showing a reduction in kinetic and potential energy in each cycle. The corresponding frequency domain spectrum in Fig. 4.6(b) shows one main peak, corresponding to the heave natural frequency, which would be typical of a single degree of freedom system. On the other hand, from the pitch free decay results in Fig. 4.7, it is apparent that the response contains vibration in more than one degree of freedom, as the time trace is quite irregular and there is an alternating increase and decrease in energy in the system from one peak to the next. The frequency domain spectrum of the pitch motion reveals three main peaks confirming this observation. The reason for this is that it is almost impossible to excite a pure pitch with a static displacement, due to a coupling with both the surge and the heave modes. The mooring system may also introduce nonlinearities which will interact with the pitch oscillations.

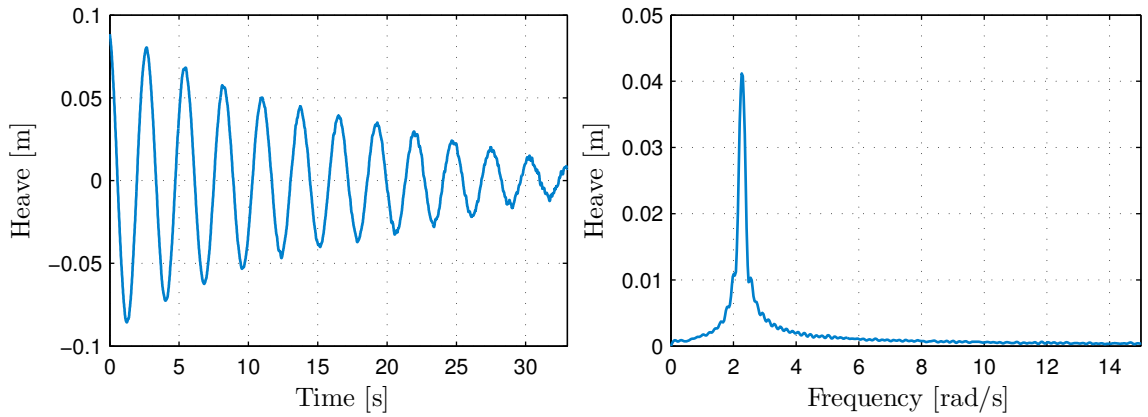

(a) (b)

Figure 4.6: (a) Experimental time trace for heave free decay test (b) frequency domain amplitude spectrum for heave free decay test

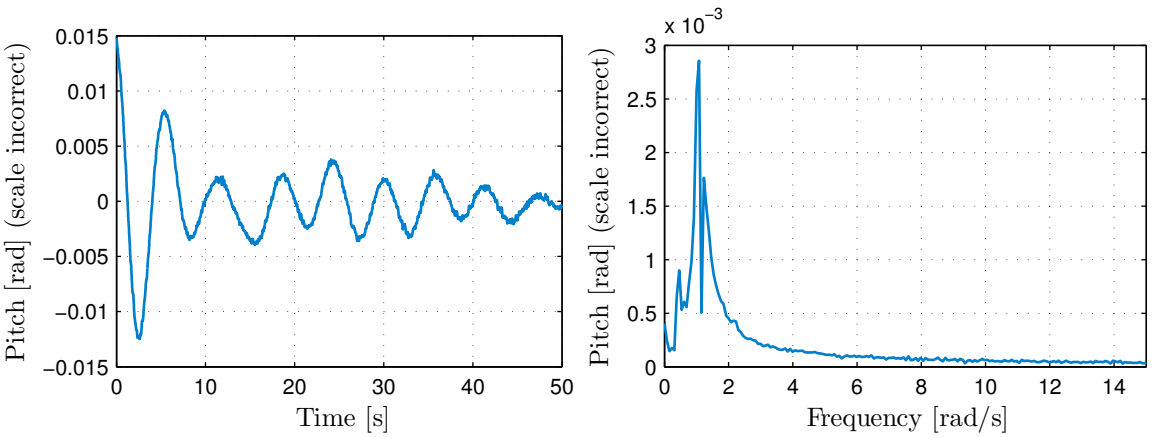

(a) (b)

Figure 4.7: (a) Experimental time trace for pitch free decay test (b) frequency domain amplitude spectrum for pitch free decay test

Mode	Natural frequency (rad/s)
Heave	2.199
Pitch	1.068

Table 4.4: Nautral frequencies of SML17 based on free decay tests

Chapter 5

Nonlinear numerical model implementation & validation

5.1 WAMIT pre-processing

The first step in implementing the nonlinear model is to obtain the hydrodynamic coefficients from WAMIT. WAMIT is a boundary element method software program developed for the computation of wave loads and motions of floating or submerged offshore structures. It is based on linear potential theory and is capable of solving the diffraction and radiation problem for a given geometry for a range of frequencies. For the numerical simulations in the current work, WAMIT is utilised to obtain the added mass matrix at infinite frequency and also the matrix of radiation and diffraction impulse response functions. A full explanation of these quantities is given in Section 3.4.

5.1.1 Description of geometry for WAMIT analysis

In order to run the hydrodynamic simulations in WAMIT, the model geometry must be first defined. Since WAMIT is based on linear theory, only the body surface below the still water level $Z = 0$ needs to be defined. The geometry of the torus and FNT is developed in MultiSurf, a geometric modelling program which is linked to WAMIT by MultiSurf's relational geometry (RG) framework. The RG framework can be directly accessed by WAMIT for analysis purposes within WAMIT's higher-order solution. The advantages of this option are that the geometry is developed using the CAD environment of MultiSurf, and also that the geometry can easily be exported to WAMIT without significant effort or approximation. Due to the axi-symmetry of the model, only a quarter of the body

needs to be modelled, which requires less computational effort. The model is built with the coordinate $Z = 0$ as the design waterline so the parts of the wetted surface below $Z = 0$ are at a negative Z. The geometry and mesh as created in MultiSurf for the torus and FNT are shown in Fig. 5.1.

Resonant interactions can occur in the inner fluid domain between the torus and the FNT, known as the moonpool[1], which are manifested as extreme amplifications of the hydrodynamic loading [65]. Since linear potential theory generally overpredicts the amplitude of the resonances, an effective way to apply a damping factor to the moonpool in WAMIT can be implemented by replacing the physical free surface of the moonpool by a lid, or heaving piston as outlined by Newman [66]. Since the lid is free to heave, without external constraints, it acts just like the free surface. With moderate choices of damping to the lid heave mode, the resonant modes are attenuated. As the moonpool cross-section is small, only the heave mode is relevant within the range of wave periods considered. Once the geometry is created in MultiSurf, it is then exported to WAMIT for the hydrodynamic analysis. The complete SML17 model for the WAMIT analysis including the lid is shown in Fig. 5.2.

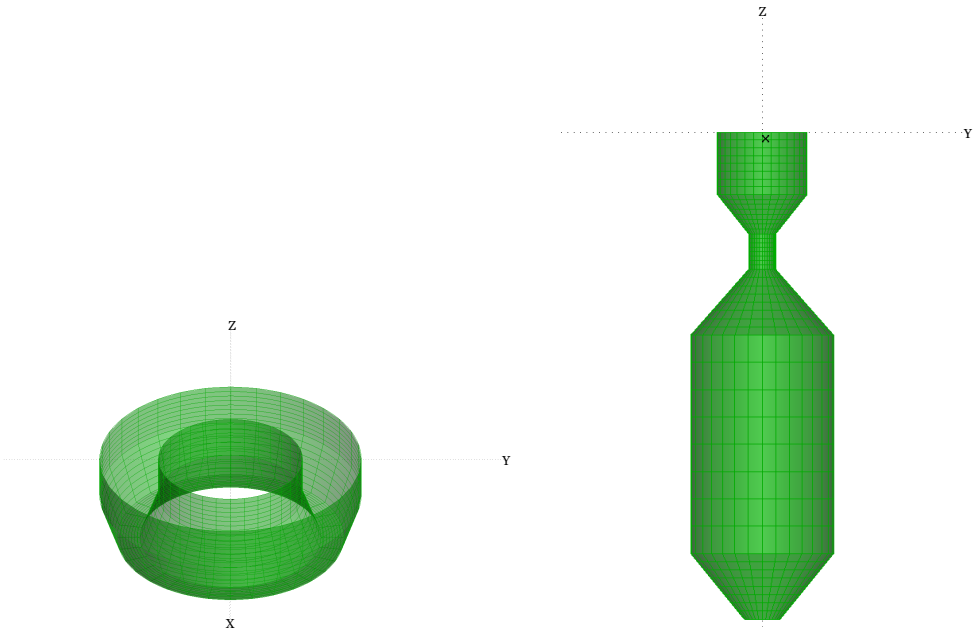

(a) Torus (b) FNT

Figure 5.1: Torus and FNT geometry and mesh created in MultiSurf

[1]The small gap between the torus and the FNT is known as a moonpool

5.1.2 WAMIT ouput

Regarding the WAMIT computations, the hydrodynamic analysis was performed for a set of 300 uniformly spaced wave frequencies between 0.0314 rad/s and 9.42 rad/s. Computations were also performed at the infinite frequency limit so as to construct the added mass matrix at infinite frequency $a(\infty) \in \mathbb{R}^{12\times12}$. The hydrodynamic added mass and damping coefficients output from WAMIT are illustrated in Appendix A.1 and A.2 respectively. It should be noted from these figures that both the added mass and damping coefficients are frequency dependent, and that the added mass coefficients approach a constant value at high frequencies, while the damping coefficients are close to zero for both low and high frequencies.

Using the same notation as presented in Section 3.6.4, the added mass coefficient $a_{(j\ k)}$ refers to the added mass in mode j due to a change in acceleration in mode k, where modes *1-6* are the torus modes (surge, sway, heave, roll, pitch and yaw) and modes *7-12* are the FNT modes. For example, $a_{(1\ 5)}$ refers to the added mass of the torus in surge due to a change in acceleration of the torus in pitch whereas $a_{(7\ 11)}$ represents the added mass of the FNT in surge due to a change in acceleration of the FNT in pitch. Similarly, for the damping, the coefficient $b_{(j\ k)}$ refers to the damping in mode j due to a change in velocity in mode k.

The diffraction excitation force coefficients are shown in Appendix A.4. Since the analysis is performed in head waves, there is only excitation in the surge, heave and pitch modes. Both the radiation damping and diffraction excitation force coefficients are transformed into time domain impulse response functions using the Frequency-to-Time-domain (F2T) utility in WAMIT. The radiation and diffraction impulse response functions are illustrated in Appendix A.3 and A.4 respectively. It should be noted that the radiation impulse response functions $K_{r_{(j\ k)}}$ are zero for time $t < 0$, whereas the diffraction impulse response functions $K_{d_{(j)}}$ are non-zero for time $t < 0$. As explained in Section 3.4.3, the diffraction force is acausal, due to the body being affected by the incident wave before it reaches the reference, which is defined to act at the centre of the body.

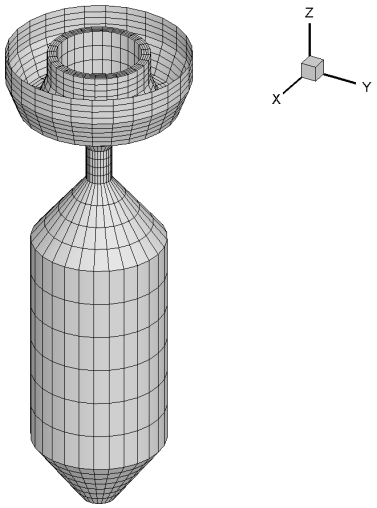

Figure 5.2: SML17 model including torus, FNT and lid as used in WAMIT hydrodynamic analysis

5.2 Validation of re-meshing algorithm

As outlined in Section 5.1, the WAMIT analysis requires only the geometry of the mean wetted surface of the torus and FNT to be constructed. The reason for this is that WAMIT is based on a linear analysis, and therefore the hydrodynamic forces are calculated on the mean wetted surface of each body below the still waterline ($Z = 0$), due to the assumption of small amplitude waves. However, in the nonlinear numerical model simulations, the entire geometry including the body surfaces above the still waterline must be modelled, as the nonlinear Froude-Krylov excitation forces and nonlinear Froude-Krylov hydrostatic restoring forces are calculated on the instantaneous wetted surface of the body in this model. Therefore, prior to running the nonlinear simulations, the entire geometry of each body, including parts of the geometry for $Z > 0$ must be created using the software package MultiSurf. The geometry is then discretised into panels in Multisurf; the coordinates of the nodes of each panel along with the connectivities of each panel are then exported for use in the nonlinear model.

The re-meshing algorithm used for for computing the intersection between the free surface and the body surface was developed by Gilloteaux [40]. Gilloteaux breaks down the procedure for discretising the wetted surface using the re-meshing algorithm into six steps, as shown in Fig. 5.3. The first is reading the geometry, resulting in the spatial

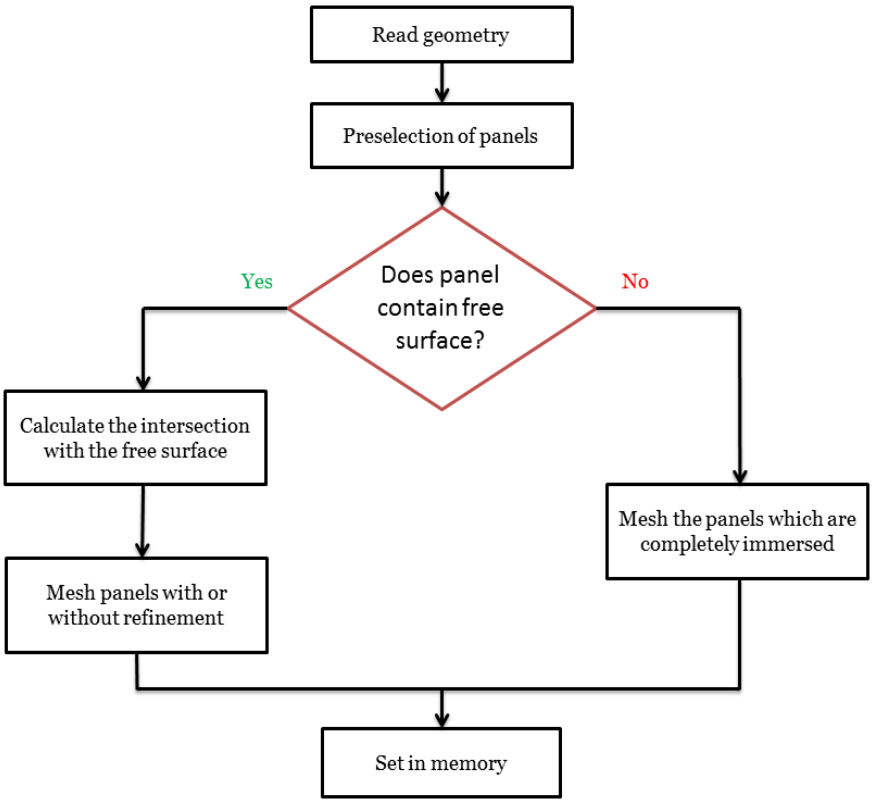

Figure 5.3: Procedure for discretisation of the wetted surface [40]

coordinates of the tops of the panels and their connectivities. It follows a stage of pre-selection whereby the panels are sorted according to their position relative to the free surface. The panels containing the free surface are stored along with the panels which are completely immersed. The third stage applies to panels containing the free surface; it looks for the intersection between the free surface and the panels. Once the intersection is determined, then the submerged part is meshed. The fourth step uses the algebraic mesh procedure called transfinite method, which is an interpolation procedure that can generate grids conforming to specified boundaries. The fifth step occurs for panels which are completely immersed in the same way as above—discretised using the transfinite method. Finally, the last step is mesh memorisation, in order to apply the pressure field at the centre of the panels, for calculation of the static and dynamic pressure due to the incident wave field, resulting in the nonlinear Froude-Krylov forces. Fig. 5.4 shows a snapshot of the SML17 simulation model where the wetted surface due to an irregular wave is meshed using the method outlined above.

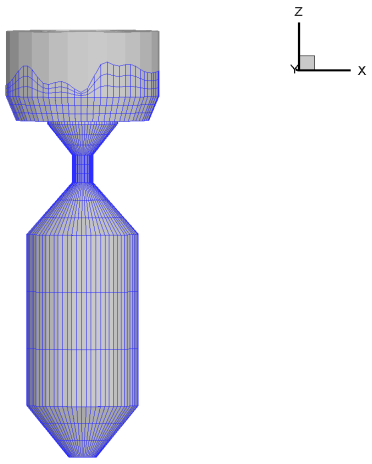

Figure 5.4: View of the SML17 nonlinear simulation model showing discretisation of the wetted surface due to an irregular wave field

A series of numerical hydrostatic inclination tests were carried out on a floating cylinder to validate the accuracy of the algorithm. The principle is to calculate the righting moment using the exact wetted surface in still water for a series of roll angles using the nonlinear numerical model. The hydrostatic and stability software package Hydro was then used to compare the results for the same set of tests. The results of this analysis are shown in Fig. 5.5, where it can be seen that the re-meshing algorithm used in the nonlinear model is capable of accurately calculating the instantaneous wetted surface of the body.

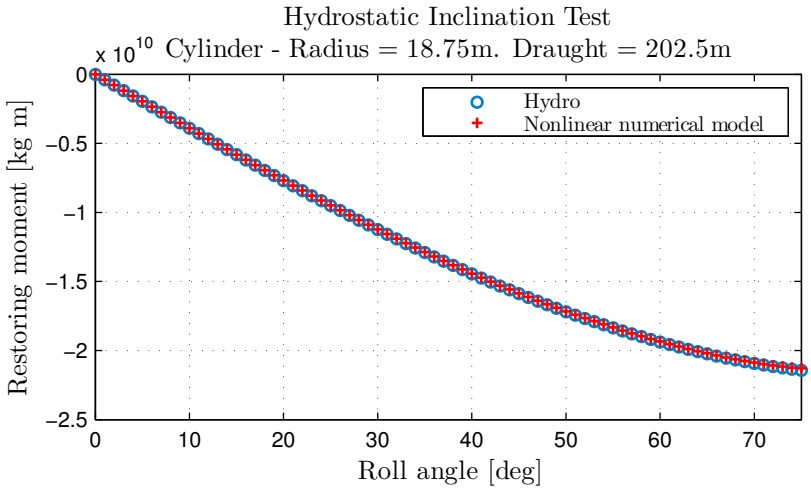

Figure 5.5: Comparison of the hydrostatic restoring moment obtained from the commercial software package Hydro and the nonlinear numerical model

5.3 Validation of convolution algorithm

The development of the algorithm for calculating the radiation forces and diffraction forces in the nonlinear numerical model was developed in the current work. As explained in Section 3.4.2, a convolution of the radiation impulse response function with the previous time history of the body velocity is used to calculate the radiation forces, while a convolution of the diffraction impulse response function with the wave elevation at the origin of the inertial frame is used to calculate the diffraction forces. A general mathematical description of the convolution integral, along with a geometric interpretation of convolution is provided in Appendix B. The author found that an accurate model of the linear radiation force convolution term was necessary to model parametric resonance. The method for performing the convolution in the current work can be illustrated by re-writing the convolution term for the radiation force in Eqn. 3.43. For the heave degree of freedom (*mode 3*), for example, this can be written

$$F_{r3} = \int_0^t K_{r_{(3\ 3)}}(t-\tau)\dot{\xi}_3(\tau)d\tau \tag{5.1}$$

where $K_{r_{(3\ 3)}}$ is the radiation impulse response function in the heave degree of freedom due to an impulse in velocity in the heave mode, and $\dot{\xi}_3$ is the heave velocity. To illustrate each of these terms graphically, it is first necessary to express the heave velocity and the impulse response function in terms of a "dummy" integration variable τ. This results in $\dot{\xi}_3(\tau)$ for the heave velocity and $K_{r_{(3\ 3)}}(\tau)$ for the impulse response function as shown in Figs. 5.6(a) and (b) respectively. It should be noted that the impulse response function has been scaled in these figures to the same order of magnitude of the velocity for better visualisation of the process. The impulse response function is then mirrored about the y-axis to produce $K_{r_{(3\ 3)}}(-\tau)$, and is then shifted to time t resulting in $K_{r_{(3\ 3)}}(t-\tau)$ as shown in Fig. 5.6(c). The product of $K_{r_{(3\ 3)}}(t-\tau)$ and $\dot{\xi}_3(\tau)$ is shown in Fig. 5.6(d), with the area under the graph shown as shaded. Finally, the result of the convolution is shown in Fig. 5.6(e) which is the integration of the product of $K_{r_{(3\ 3)}}(t-\tau)$ and $\dot{\xi}_3(\tau)$, found by calculating the shaded area under the graph in Fig. 5.6(d).

The equation of motion in the nonlinear model is numerically integrated using a fourth-order Runge-Kutta method which will be discussed further in Section 5.4. This method requires the equation of motion to be solved four times in each time step; once at the initial

point t_i, once at the endpoint t_{i+1}, and twice at the midpoints. In order for the convolution terms to be calculated at the midpoints, an interpolation procedure is used to calculate both the impulse response function and the instantaneous velocity time-history at the midpoints. This is done using a simple linear interpolation method which is explained in detail in Appendix C. Finally, trapezoidal integration is used to integrate the product of the impulse response function and the state variable according to Eqn. 3.43. The method of trapezoidal integration is explained in Appendix D.

A series of numerical simulations over a wide range of excitation frequencies were performed in regular waves using a floating truncated cylinder in order to validate the algorithm developed for calculating the convolution terms in the numerical model. The MultiSurf model of the truncated cylinder used for the analysis is shown in Fig. 5.7. Since the aim of the tests was to validate the radiation and diffraction forces, i.e linear forces, the algorithm for calculating the instantaneous wetted surface of the body was turned off so that the diffraction, radiation and Froude-Krylov excitation forces were calculated on the mean wetted surface using convolution operators. The diffraction forces and Froude-Krylov excitation forces were calculated using a convolution of the corresponding impulse response function with the wave elevation at the origin of the inertial frame.

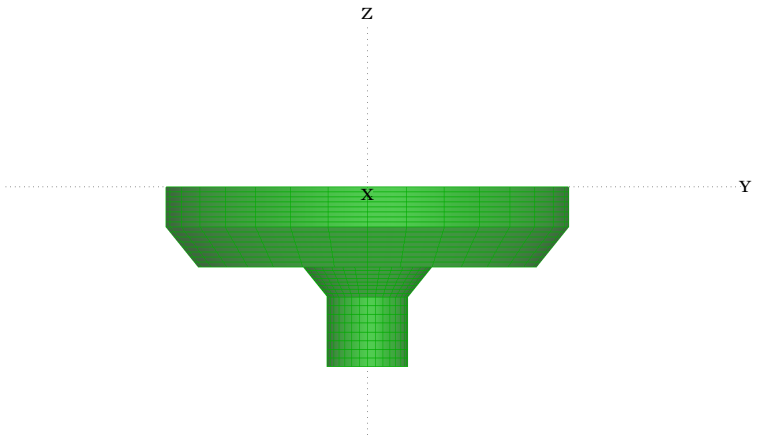

Figure 5.7: MultiSurf model of the truncated cylinder used for validating the linear numerical model

Based on the results of the time domain simulations, Response Amplitude Operators (RAOs) were constructed which are the ratio of the amplitude of motion response of the body, for one particular degree of freedom, to the wave amplitude causing the motion.

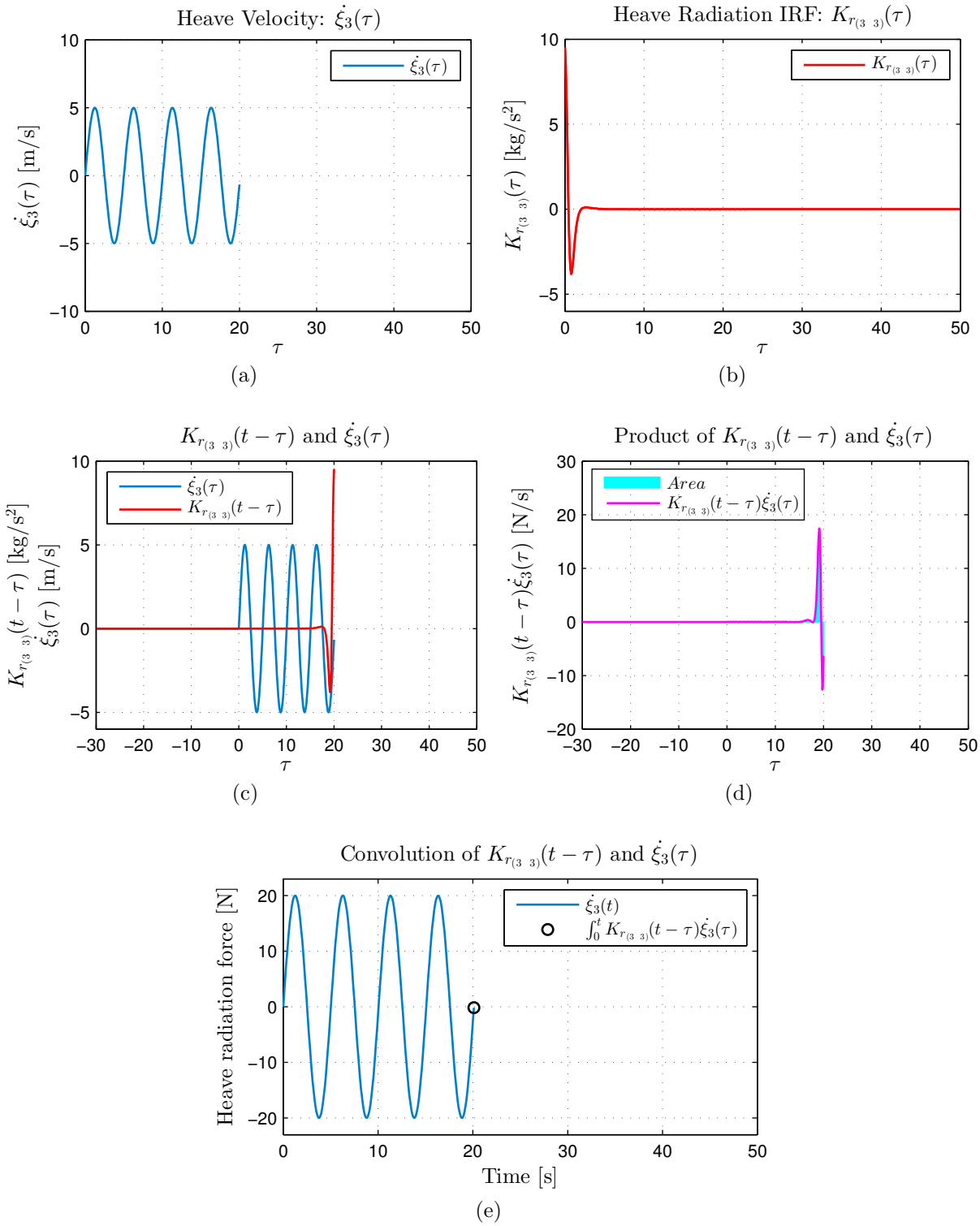

Figure 5.6: (a) Heave velocity $\dot{\xi}_3(\tau)$ (b) heave impulse response function $K_{r_{(3\ 3)}}(\tau)$ (scaled) (c) heave velocity $\dot{\xi}_3(\tau)$ and time shifted and mirrored impulse response function $K_{r_{(3\ 3)}}(t-\tau)$ (d) product of $K_{r_{(3\ 3)}}(t-\tau)$ and $\dot{\xi}_3(\tau)$, the area under the graph is shown as shaded (e) convolution of $K_{r_{(3\ 3)}}(t-\tau)$ and $\dot{\xi}_3(\tau)$ to give radiation damping force

The RAOs were calculated over a wide range of wave frequencies to get an overall idea of the linear responses of the body in waves. The RAOs were then compared with the RAOs output from WAMIT based on a frequency domain analysis of the truncated cylinder using the same wave conditions. The RAOs from the numerical model (with nonlinear algorithm turned off) and the WAMIT simulations of the truncated cylinder are presented in Figs. 5.8(a) - (c) for the surge, heave and pitch modes respectively, as a function of incident wave frequency. Only these modes are presented as there is no direct lateral excitation and hence no response in the sway, roll and yaw modes in a linear analysis of regular head waves. The figures show that the RAOs obtained using the two methods are in good agreement except for the frequencies around the pitch natural frequency at approximately 5 rad/s in Figs. 5.8(c). The unity amplitude heave RAOs in Figs. 5.8(b) corresponding to the zero-frequency limit agrees well in both methods. For extremely long period waves (low frequency), the body follows the wave in heave, which means that the output is the same as that of the input excitation. A strong correlation between the surge and pitch can be seen between 4 rad/s and 6 rad/s. As the wave frequency is reduced from 5 rad/s to 4 rad/s, there is a reduction in surge and pitch motion. This is partly due to a coupling in the surge and pitch modes. As the body goes through pitch resonance at 5 rad/s there is a shift in phase and the body will not encounter the incident wave crest when the pitch motion is reaching it's maximum amplitude, but a little after, thus creating a smaller pitch force and a smaller surge force also. For frequencies less than 4 rad/s, the surge response increases as the wave frequency decreases since the surge motion is related mainly to the incident wavelength, so it increases as the wave frequency decreases. This comparison of the RAOs using the time domain numerical model with the WAMIT frequency domain RAOs has verified the technique for computing the linear diffraction and radiation forces in the nonlinear numerical model.

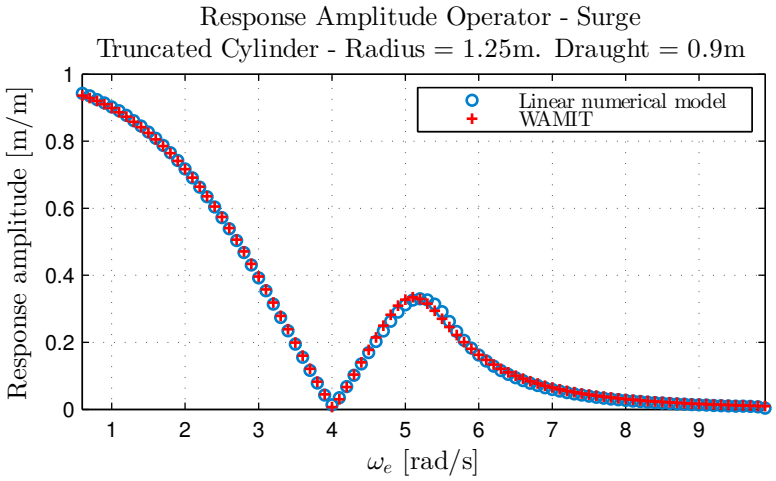

(a)

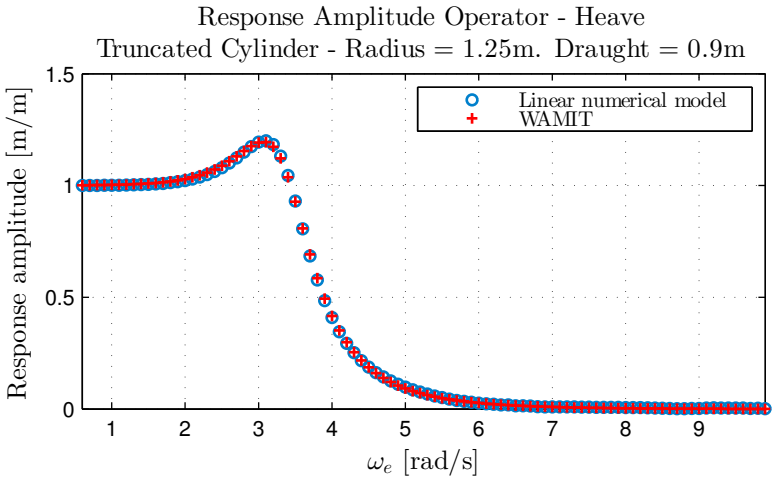

(b)

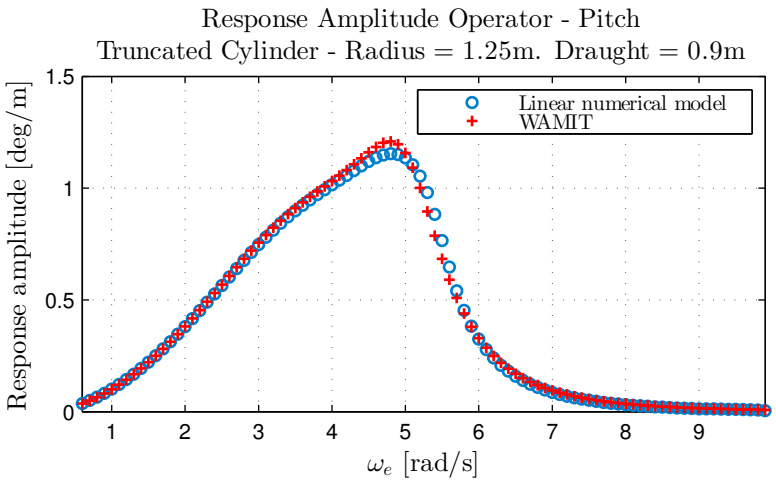

(c)

Figure 5.8: Comparison between linear RAOs obtained using the numerical model and WAMIT for (a) surge motion (b) heave motion and (c) pitch motion

5.4 Solving the nonlinear equation of motion

The nonlinear equation of motion given in Eqn. 3.91 is solved using a Runge-Kutta fourth order method. This is a numerical technique used for numerically integrating ordinary differential equations. An explanation of the Runge-Kutta fourth order procedure is provided in Appendix E. Fig. 5.9 presents the program flowchart depicting the general procedure performed by the nonlinear simulation model. It can be seen that the pre-processing stage occurs outside the time-loop and involves modelling the geometry of the WEC, performing the hydrodynamic analysis in WAMIT and computation of the incident wave train coefficients. The program initially reads an input file whereby the user can specify the following inputs:

- regular or irregular waves;
- JONSWAP or Bretschneider wave spectrum (if irregular waves have been chosen)
- wave characteristics; wave period, wavelength, wave height, water depth, duration of ramp function;
- coordinates of linear mooring system and mooring stiffness coefficients;
- PTO damping coefficient;
- time step;
- nonlinear viscous drag coefficients.

Inside the main loop, the calculation of the wetted surface along with the calculation of the forces due to fluid-structure interactions are computed. At each time-step, the forces, motions and velocities are output to corresponding *.txt* files. The updated coordinates of the corner points of each panel in the fixed frame of reference are also exported for visualisation purposes.

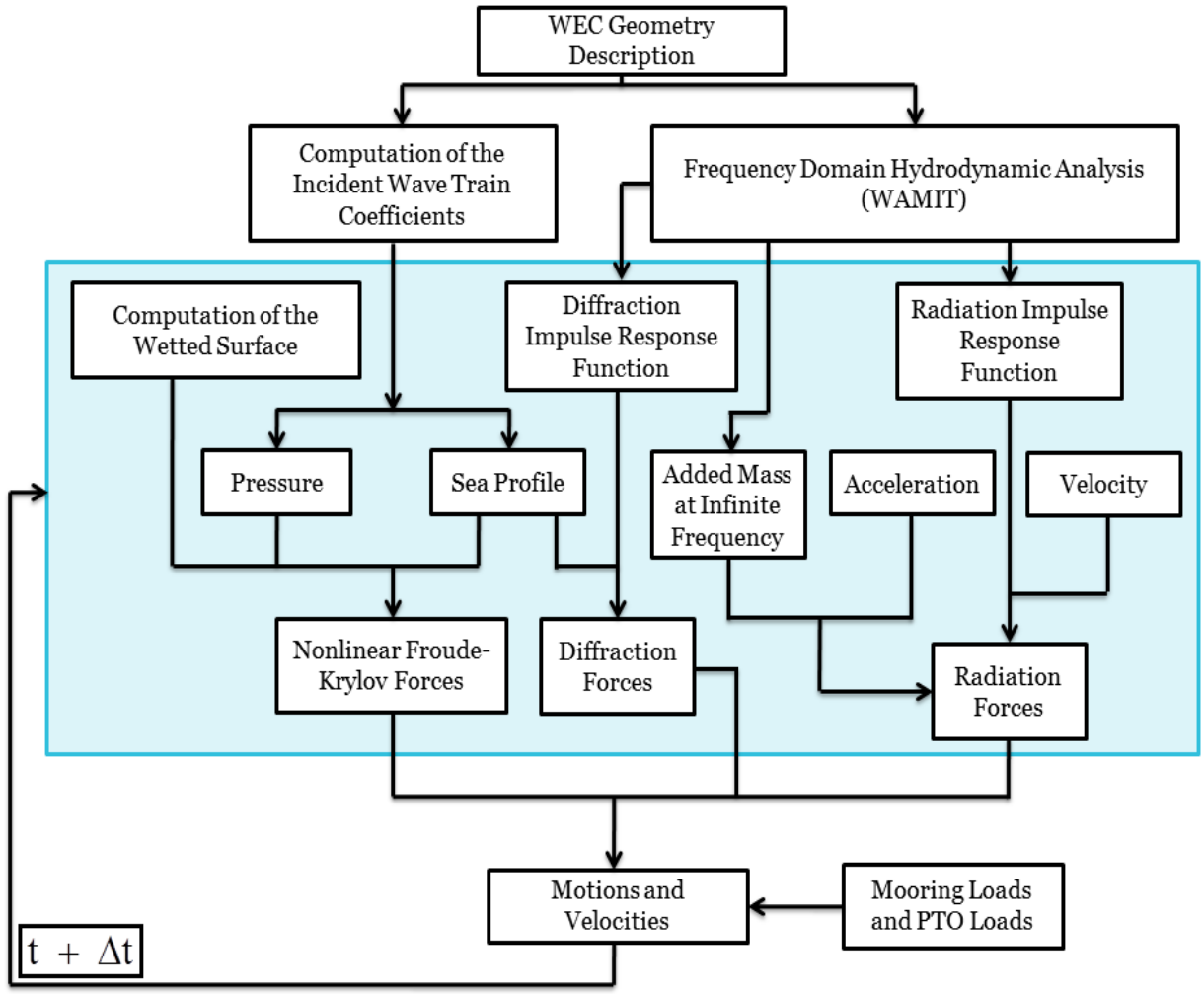

Figure 5.9: Flowchart depicting the general procedure performed by the nonlinear numerical model

Chapter 6

Results in regular waves

6.1 Regular waves - non parametric resonance conditions

A set of of experiments were carried out at École Centrale de Nantes (ECN) in regular waves at wave frequencies outside the exact parametric resonance condition of $\omega_e/\omega_4 = 2$, to investigate the first order responses of the system. The ratio ω_e/ω_4 is the ratio of the wave excitation frequency to the roll natural frequency. It should be noted that due to the axi-symmetric geometric properties of the device, the roll natural frequency is equal to the pitch natural frequency ($\omega_4 = \omega_5$). The experimental conditions for the this set of tests are outlined in Table 6.1. Tests T01-T10 correspond to wave amplitudes of 0.025m while tests T11-T20 correspond to wave amplitudes of 0.05m. Both sets of wave amplitudes were considered for a range of wave excitation frequencies with a constant PTO damping coefficient of 5000 Ns/m. Numerical simulations using the same test conditions in Table 6.1 were carried out using the nonlinear numerical model to see if the the model was capable of reproducing the motion responses of SML17 which were observed in the experimental tests. The exact parametric resonance tuning of 2 was not considered in this set of tests as the main objective was to validate the numerical model in non parametric resonance conditions.

All simulations were performed with an initial roll and pitch angle of 0.007 rad ($\xi_{4_0} = \xi_{5_0} = 0.007$ rad), and a 5s ramp function was used to gradually increase the total energy of the wave. The mooring system used in the experiments was modelled as a simple linear stiffness in the numerical simulations, using three mooring lines connecting the FNT to

Test No.	ζ_o [m]	ω_e [rad/s]	ω_e/ω_4	B_{PTO} [Ns/m]
T01	0.025	5.0265	4.706	5000
T02	0.025	4.3982	4.118	5000
T03	0.025	3.1416	2.941	5000
T04	0.025	2.8274	2.647	5000
T05	0.025	2.6389	2.471	5000
T06	0.025	2.4504	2.294	5000
T07	0.025	2.3248	2.177	5000
T08	0.025	2.2619	2.118	5000
T09	0.025	2.0106	1.882	5000
T10	0.025	1.885	1.765	5000
T11	0.05	5.0265	4.706	5000
T12	0.05	4.3982	4.118	5000
T13	0.05	3.1416	2.941	5000
T14	0.05	2.8274	2.647	5000
T15	0.05	2.6389	2.471	5000
T16	0.05	2.4504	2.294	5000
T17	0.05	2.3248	2.177	5000
T18	0.05	2.2619	2.118	5000
T19	0.05	2.0106	1.882	5000
T20	0.05	1.885	1.765	5000

Table 6.1: Experimental conditions for tests T01-T20

the bottom of the tank. Fig. 6.1 shows a 3D view of the SML17 simulation model with mooring lines and incident wave.

Transfer functions this set of tests are presented in Fig. 6.2 for tests T01 - T10 and Fig. 6.3 for tests T11 - T20. The transfer functions are defined as the normalised amplitude of the oscillations in the considered degree of freedom. The translational modes (surge and heave) are normalised by the incident wave amplitude ζ_o, while the rotational modes (roll and pitch) are normalised by $k\zeta_o$, i.e., the product of the wave amplitude and the wavenumber k, as defined in Eqn. 3.21. It should be noted that the roll mode is not directly excited in regular head waves, therefore the roll transfer function is known as the wave induced transfer function. The amplitude of the oscillations were calculated using the standard deviation of the signal after transients had died out. Frequency domain amplitude spectra of the motion responses of test T18 and test T20 are illustrated in Figs. 6.4 and 6.5 respectively. These two tests were investigated to see if nonlinear effects were apparent in the frequency response due to the higher motion response, which would be expected for these lower frequency (higher period) waves.

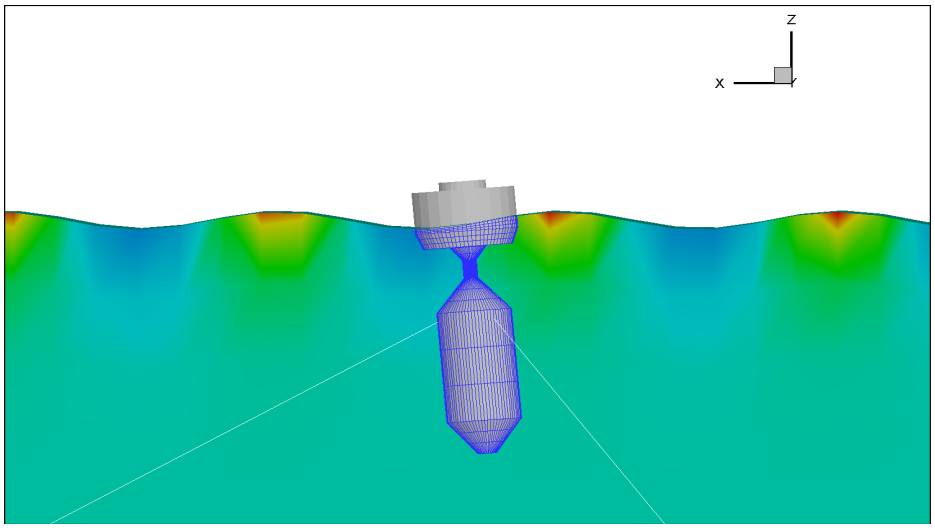

Figure 6.1: 3D view of the SML17 simulation model showing incident wave, mooring lines and meshed wetted surface for calculation of the nonlinear Froude-Krylov forces

6.1.1 Analysis of the nonlinear numerical model in non parametric resonance conditions

A comparison of the simulation and the experimental transfer functions for tests T01 - T10 can be seen in Fig. 6.2. Apart from slight deviations at the smaller wave frequencies, the overall trend of the motion responses obtained from the numerical model in both the vertical and horizontal planes shows excellent agreement with that from the experimental tests. The small errors occurring at the lower wave excitation frequencies are possibly due to mooring nonlinearities appearing in the experimental tests as a result of the complex mooring system utilised in the experiments. These nonlinear mooring effects are not captured in the numerical model due to the assumption of a linear mooring system in the analysis.

The heave response of both the torus and FNT is quite large for the lower wave excitation frequencies with the transfer functions of both bodies responding with amplitudes of almost twice the wave amplitude at the heave resonance of 2.199 rad/s. However, the relative heave transfer function is less than one for all wave excitation frequencies due to both bodies having large heave responses, but with a small heave phase angle between the two bodies. Since the mooring system used in the numerical model and the experimental tests is designed to have a minimal effect on the heave motion response, the differences between the heave responses in the numerical model and experimental results can be

attributed to the damping forces provided by the PTO system. A linear PTO was used in the experimental tests which is represented as a linear damping force in the numerical simulations. There will however be additional damping appearing in the real model due to friction in the linear bearing system and PTO, which are not modelled in the numerical simulations. Structural damping due to rubbing friction and joint slippage will also be present in the experimental tests which are not represented in the numerical model.

Both the experimental and numerical results show almost zero roll response for all frequencies considered as shown in Fig. 6.2(e). The reason for this is that the roll mode is not externally excited in regular waves, and since the test conditions are for reasonably small amplitude waves ($\zeta_o = 0.025$m) which are outside the parametric resonance zone of instability, the device is not being parametrically excited. The pitch motion transfer function is unity for the lowest excitation frequency tested and then steadily decreases as the wave frequency increases, which is predicted extremely well in the simulations.

The experimental and numerical transfer functions for tests T11-T20 at the larger amplitude of $\zeta_o = 0.05$m are compared in Fig. 6.3. The numerical model shows good capabilities in reproducing the system dynamics of the device for this wave height, except for the torus and FNT heave motions at the lower wave frequencies, where the numerical model tends to overpredict the response by around 22%. These deviations in the heave motion are due to friction in the PTO and structural damping effects in the real system which were not included in the numerical model as explained previously.

Since the responses are normalised, the transfer functions for tests T11-T20 and tests T01-T10 are very similar, as the only difference in the two sets of tests is the wave amplitude. The most obvious difference between the two set of tests is in the roll mode which is not externally excited in regular waves. In test T18 ($\omega_e = 2.2619$ rad/s) in Fig. 6.3(e), the numerical model shows a large wave induced roll transfer function of almost 1.5, whereas all other tests have almost zero response in both the simulations and experimental tests. In order to understand this disagreement between the model behaviour and experimental results, the tuning factor ω_e/ω_4 must be taken into consideration. It can be seen from Table 6.1 that test T18 corresponds to a tuning factor of 2.118, which is close to the first instability region ($\omega_e/\omega_4 = 2$) of the Mathieu type equation (see Fig. 2.11). The large roll oscillations reveal that the numerical model is falsely predicting parametric roll at this

wave frequency considering that the experimental results for this test shown almost zero roll response. It seems that when the experimental conditions are close to the limits of stability, the numerical model does not exactly match the frequency at which the abrupt variation in roll motion takes place. However, the numerical model showed no evidence of parametric roll in test T08, as seen in Fig. 6.2(e), which also has a tuning factor of 2.118, but has a lower wave amplitude of $\zeta_o = 0.025$m. There is clearly a wave amplitude threshold which must be overcome before parametric resonance takes place. For the lower wave amplitude of $\zeta_o = 0.025$m, the amplitude of modulation of the time varying parameters in the system is not above the threshold value as there is enough damping in the system to overcome parametric instabilities. For this reason, no parametric roll takes place in test T08.

By examining the frequency domain representations of test T18 and test T20 in Figs. 6.4 and 6.5 respectively, it can be seen that, except for the roll mode, the model is responding with first order responses at the wave excitation frequency of 2.2619 rad/s for test T18 and 1.885 rad/s for test T20. The roll mode, however, is responding predominantly at the roll natural frequency of 1.068 rad/s in both tests. The main difference between the roll response in both tests is the roll amplitude. The peak value of the roll amplitude spectrum is almost two orders of magnitude higher in test T18 than it is in test T20. As explained above, the large roll oscillations observed in test T18 in the numerical model are due to parametric roll, as the numerical model is more prone to parametric instabilities in wave conditions which are close to the limits of stability. Although the frequency domain spectrum for the roll mode in test T20 also shows a peak at the roll natural frequency, this is not due to parametric roll as the amplitude of oscillation is almost zero, and instead, can be attributed to extraneous (uncontrolled) forcing due to mild mode coupling.

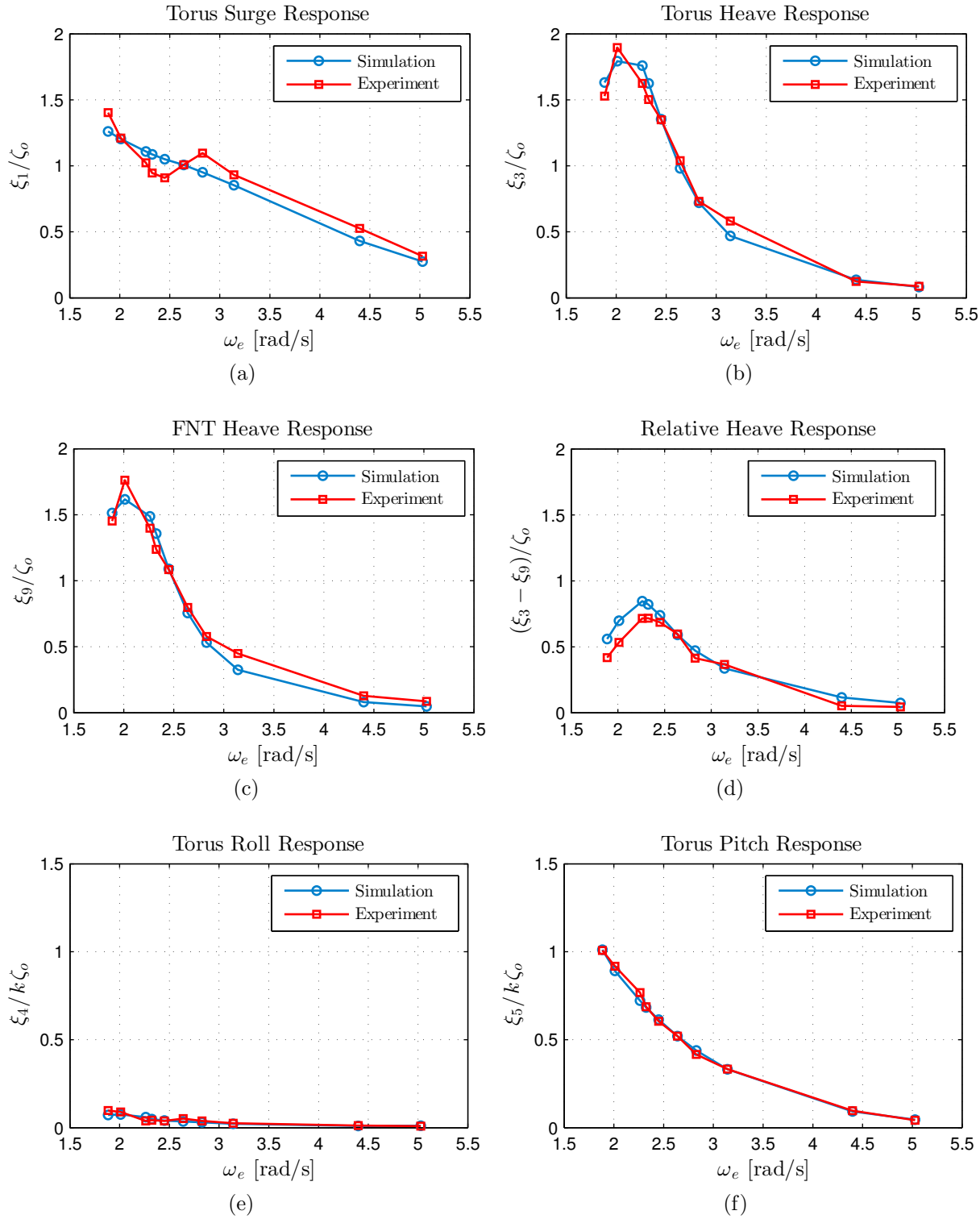

Figure 6.2: Transfer functions for tests T01-T10 for (a) torus surge (b) torus heave (c) FNT heave (d) relative heave (e) torus roll and (f) torus pitch

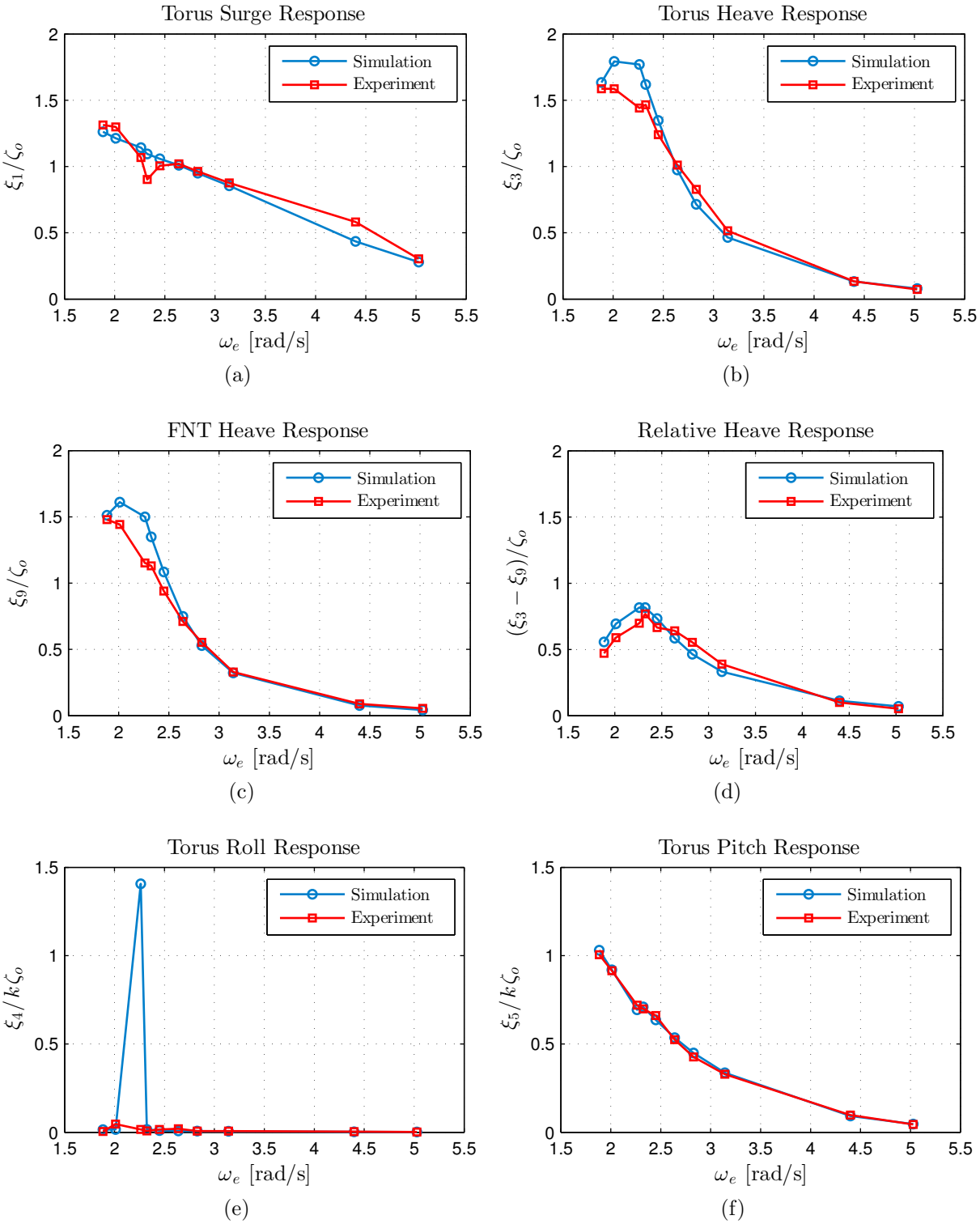

Figure 6.3: Transfer functions for tests T11-T20 for (a) torus surge (b) torus heave (c) FNT heave (d) relative heave (e) torus roll and (f) torus pitch

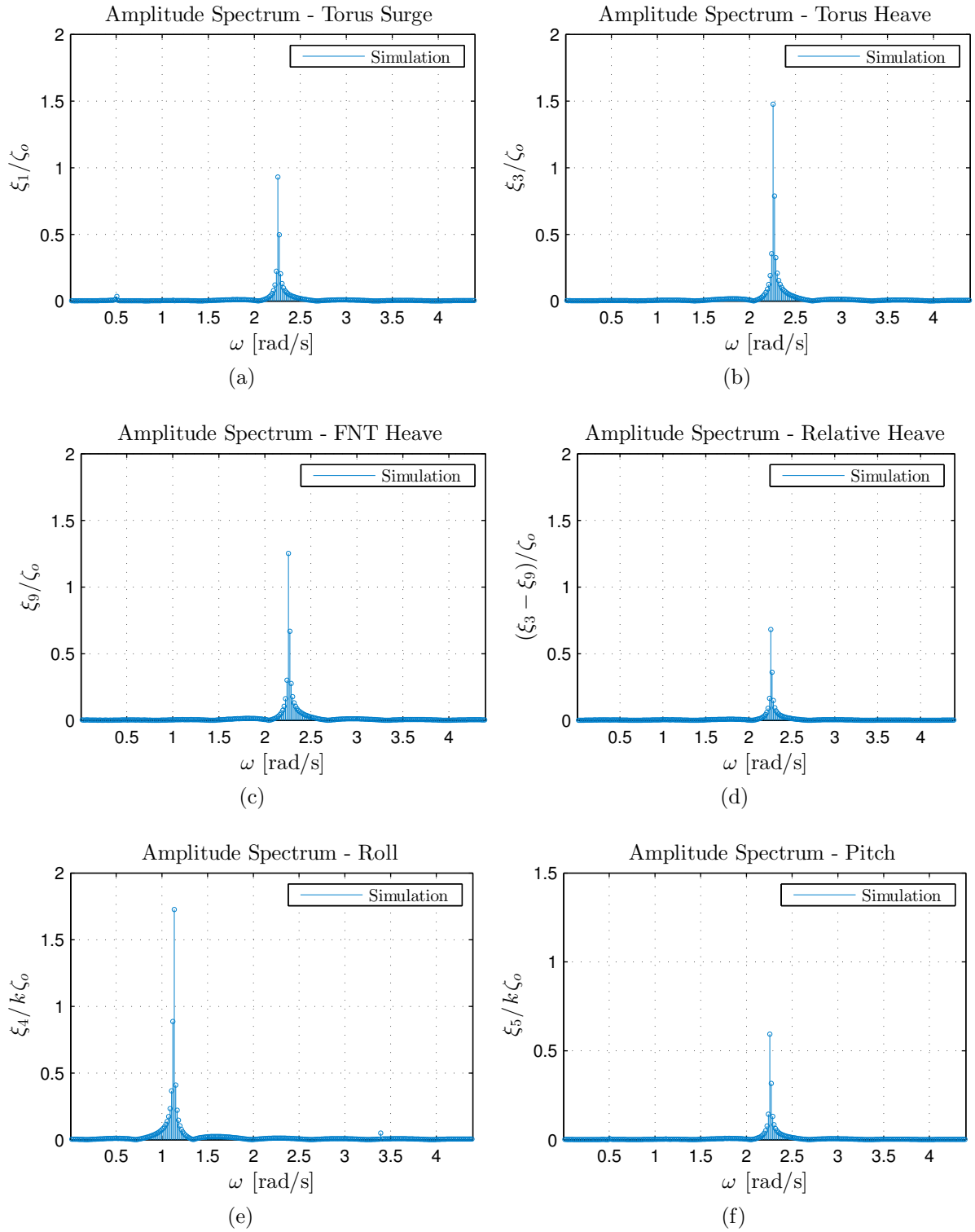

Figure 6.4: Frequency domain amplitude spectra for test T18 ($\omega_e = 2.2619$ rad/s, $\zeta_o = 0.05$m) for (a) torus surge (b) torus heave (c) FNT heave (d) relative heave (e) torus roll and (f) torus pitch

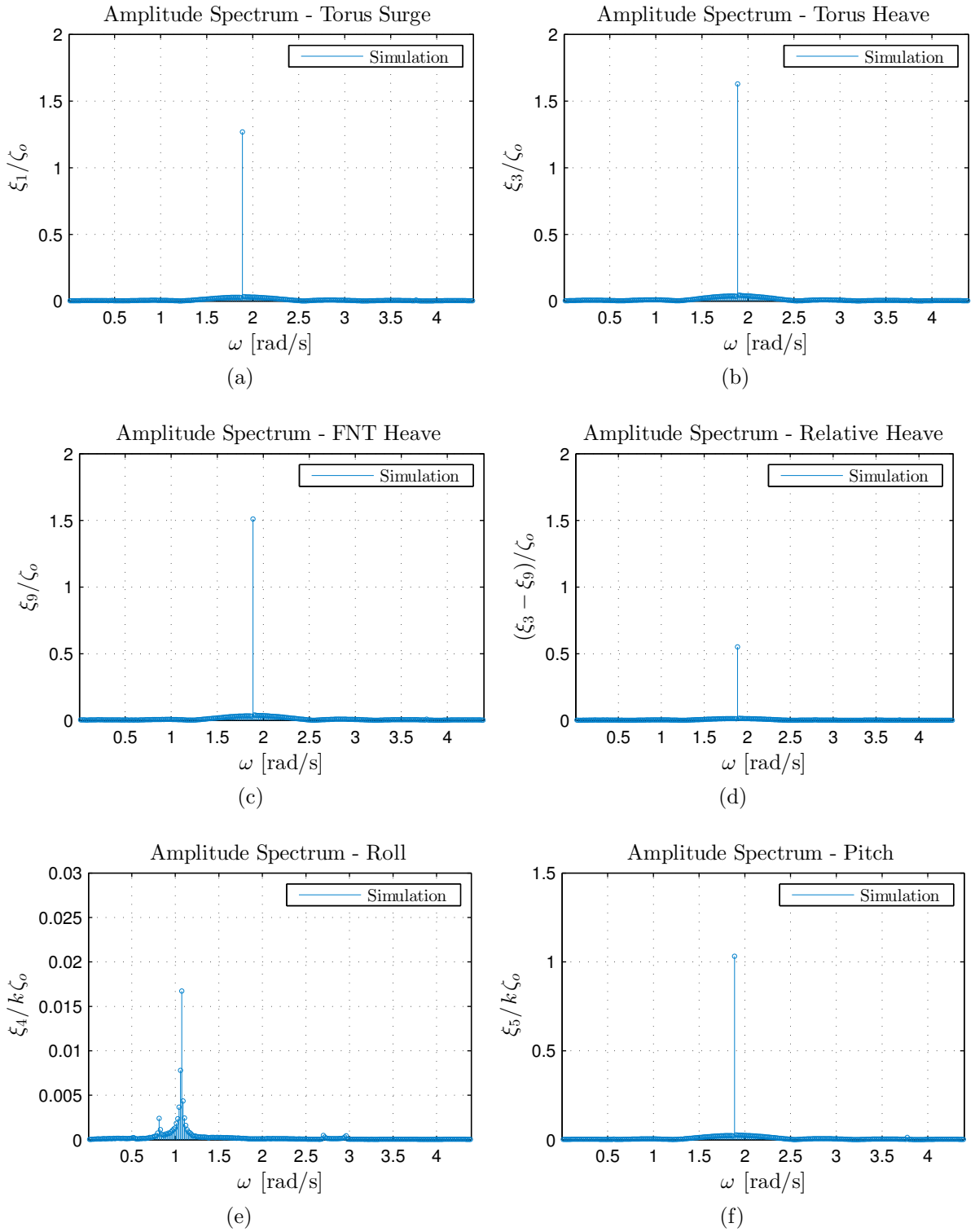

Figure 6.5: Frequency domain amplitude spectra for test T20 ($\omega_e = 1.885$ rad/s, $\zeta_o = 0.05$m) for (a) torus surge (b) torus heave (c) FNT heave (d) relative heave (e) torus roll and (f) torus pitch

6.2 Regular waves - parametric resonance conditions

A series of experiments were conducted at ECN with various levels of excitation at wave frequencies around the tuning factor of 2, in order to investigate the stability of the device at parametric resonance conditions. The experimental conditions for this set of tests are outlined in Table 6.2. A set of numerical simulations using the same set of conditions in Table 6.2 were carried out to demonstrate the ability of the numerical model to capture the nonlinear responses due to parametric motion. The time traces of these tests are presented rather than the transfer functions since it is important to have both a qualitative and quantitative evaluation of parametric motion. Ideally, the numerical model should not only have similar amplitudes of parametric oscillations, but should also develop parametric resonance within the same time frame as the experimental tests. Frequency decomposition of the motion responses from the numerical simulations was also performed to understand how the frequency response of the device differs when it is undergoing parametric resonance.

The time traces and frequency response of the numerical and experimental results are show in Figs. 6.6 - 6.9 for the tests according to Table 6.2. Only the relative heave, roll and pitch motions are shown, as they are considered the most important due to the strong nonlinear coupling between these modes when the device undergoes parametric resonance. It should be noted, however, that nonlinear coupling with the other modes (surge, sway and yaw) is also required to simulate parametric resonance in this model.

Test No.	ζ_o [m]	ω_e [rad/s]	ω_e/ω_4	B_{PTO} [Ns/m]
T21	0.025	2.26	2.1161	5000
T22	0.025	2.20	2.0599	5000
T23	0.025	2.14	2	5000
T24	0.05	2.26	2.1161	5000
T25	0.05	2.20	2.0599	5000
T26	0.05	2.14	2	5000
T27	0.075	2.26	2.1161	5000
T28	0.075	2.20	2.0599	5000
T29	0.075	2.14	2	5000
T30	0.1	2.26	2.1161	5000
T31	0.1	2.20	2.0599	5000
T32	0.1	2.14	2	5000

Table 6.2: Experimental conditions for tests T21-T32

6.2.1 Analysis of the model at parametric resonance

The series of experimental tests for waves conditions around the tuning factor of 2 revealed that SML17 is prone to parametric instabilities in the heave, roll and pitch modes when the wave excitation exceeds a certain threshold. Under the same wave conditions used during the experiments, the nonlinear numerical model shows good overall capabilities in reproducing the phenomenon. One of the main differences between the simulation and the experimental results is the threshold at which parametric resonance first begins and also the width of the instability zone, i.e., the range of wave excitation frequencies at which parametric resonance takes place for a given wave amplitude.

For a wave amplitude of $\zeta_o = 0.025$m, there was no parametric motion observed in the experimental tests as shown in Fig. 6.6. The numerical model accurately predicts the heave, roll and pitch oscillations for test T21 at the higher tuning factor of 2.1161, however, the numerical model falsely predicts parametric roll for the two tests at the tuning factors of 2.0599 and 2 corresponding to tests T22 and T23 respectively. The numerical model also falsely predicts parametric pitch and heave at the tuning factor of 2 as shown in Fig. 6.6(e). Clearly, the threshold at which parametric resonance takes place is lower in the numerical model, and also, the width of the instability region is wider in the numerical model for a given wave amplitude.

As the wave amplitude is increased to $\zeta_o = 0.05$m, the parametric resonance threshold is now exceeded in the experimental test only at the exact tuning of 2 (test T26) for all three degrees of freedom, with no parametric resonance taking place at the tuning factors of 2.1161 (test T24) or 2.0599 (test T25) as can be seen from Fig. 6.7. Again, the numerical model falsely predicts parametric roll at the tuning factors of 2.1161 and 2.0599 and falsely predicts parametric heave and pitch at the tuning factor of 2.0599 as shown in Fig. 6.7(c). At the exact tuning of 2 in Fig. 6.7(e), the numerical model develops parametric roll and pitch within the same time frame as that in the experiments, and it also predicts the magnitude of the steady state response to a high degree of accuracy. The numerical model also captures the strong coupling between the heave, roll and pitch modes. It can be seen that as both parametric roll and pitch develop, there is a corresponding reduction in the relative heave motion. This is owing the transfer of energy between the heave

mode and the roll/pitch modes. Once the onset of parametric roll and pitch begins at around 50s, the relative heave begins to reduce in magnitude, as some of the energy needed in the heave mode is transferred to the roll/pitch modes. The frequency response of the numerical simulation for this test is shown in Fig. 6.7(f), where the nonlinearity due to parametric resonance is clearly evident. The parametric motion has a significant effect on the heave mode, as can be seen from the relative heave motion spectrum. The largest peak is at the wave excitation frequency, but there are also peaks at the roll/pitch natural frequency, and also at even harmonics of the roll/pitch natural frequency, implying a strong nonlinear coupling between the modes. The nonlinearity is also evident in the pitch spectrum, where the dominant peak is at the pitch natural frequency, with a much smaller peak at the wave excitation frequency. Therefore, when parametric resonance takes place, the device pitch's predominantly at it's own natural frequency, even though it is being excited at twice the pitch natural frequency. The roll mode which is not being directly excited, is also showing strong parametric response at the roll natural frequency. It can also be seen that the heave, roll and pitch responses all reach a steady state after approximately 120s, which is well predicted in the numerical model.

The results from tests T27 - T32 for wave amplitudes of $\zeta_o = 0.075$m and $\zeta_o = 0.1$m are illustrated in Figs. 6.8 and 6.9 respectively. The main difference in the results for these tests is that parametric resonance now occurs in all three modes, for the three different tuning factors considered, in both the numerical and experimental tests. The roll and pitch modes are responding predominantly at the roll/pitch natural frequency in all of these tests, and the strength of the nonlinear coupling between the heave and roll/pitch modes is also increased as the wave amplitude increases. This is shown by the increased amplitude of the harmonics of the roll/pitch natural frequency appearing in the frequency spectra of the heave. The presence of these harmonics is consistent with a Mathieu-Duffing type nonlinearity which is embedded in the system, showing the presence of higher order nonlinearities which become more prevalent as the excitation is increased.

In relation to the onset of parametric motion, the numerical model does quite a good job at predicting the time frame at which the instability begins, except for test T27 in Fig. 6.8(a), where the numerical model develops parametric motion around 100s sooner than it does in the experiments. As the wave amplitude increases to $\zeta_o = 0.1$m, the

experimental results show the model developing parametric pitch almost immediately after the test begins, as shown in Fig. 6.9(e) for a tuning factor of 2. This tells us that in large regular waves, the parametric instability will occur in a very short space of time and a large amplitude steady state response will be attained in roll and pitch, with both modes oscillating at their natural frequency and also at superharmonics of their natural frequency. The response amplitude of the relative heave on the other hand will reduce when parametric motion takes place. This of course has a negative impact on the Wavebob as the relative heave mode is the primary power producing mode for the device.

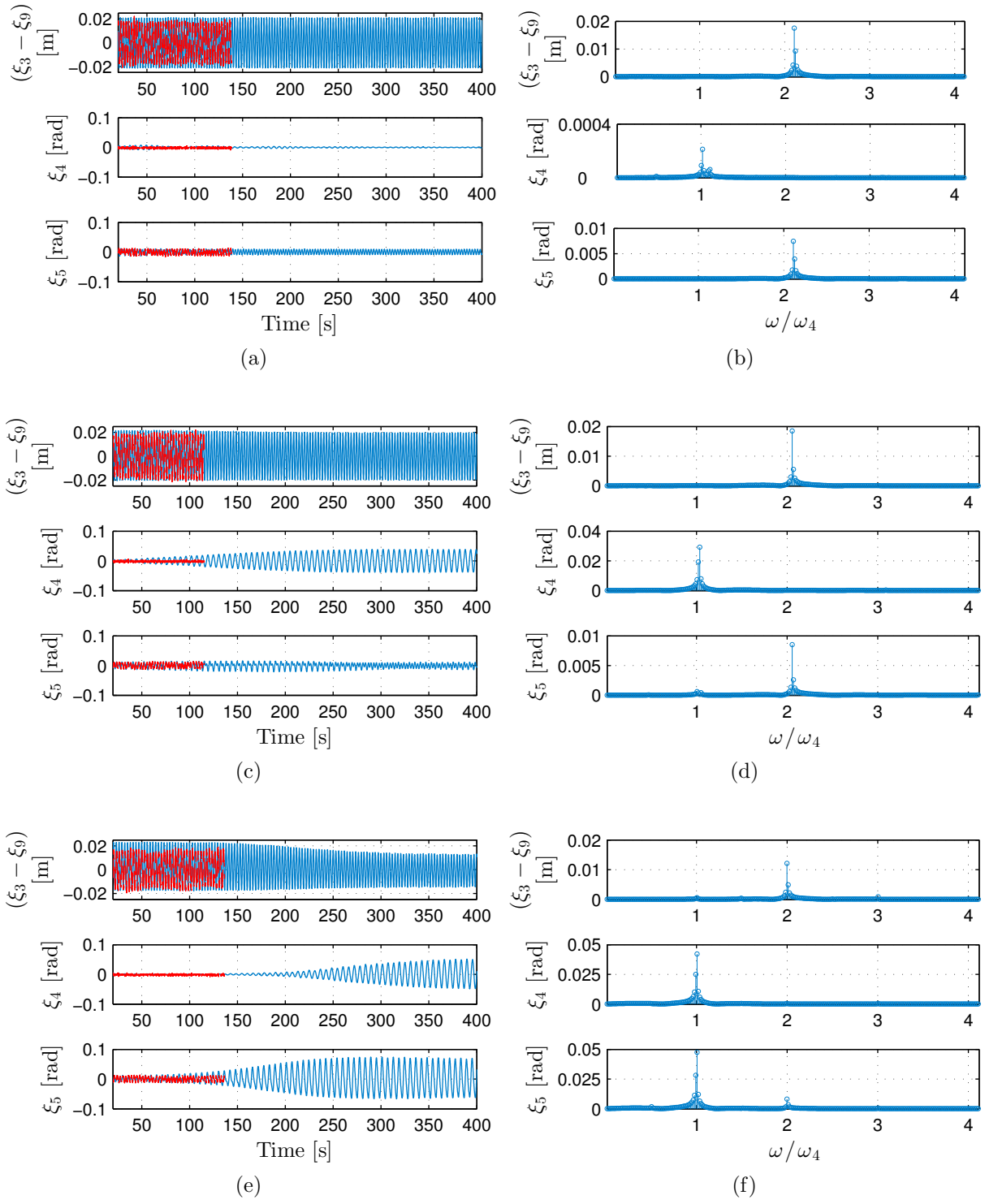

Figure 6.6: (a) Time series for test T21 (b) amplitude spectrum for test T21 (c) time series for test T22 (d) amplitude spectrum for test T22 (e) time series for test T23 (f) amplitude spectrum for test T23. Exp.(−−red), sim.(−blue)

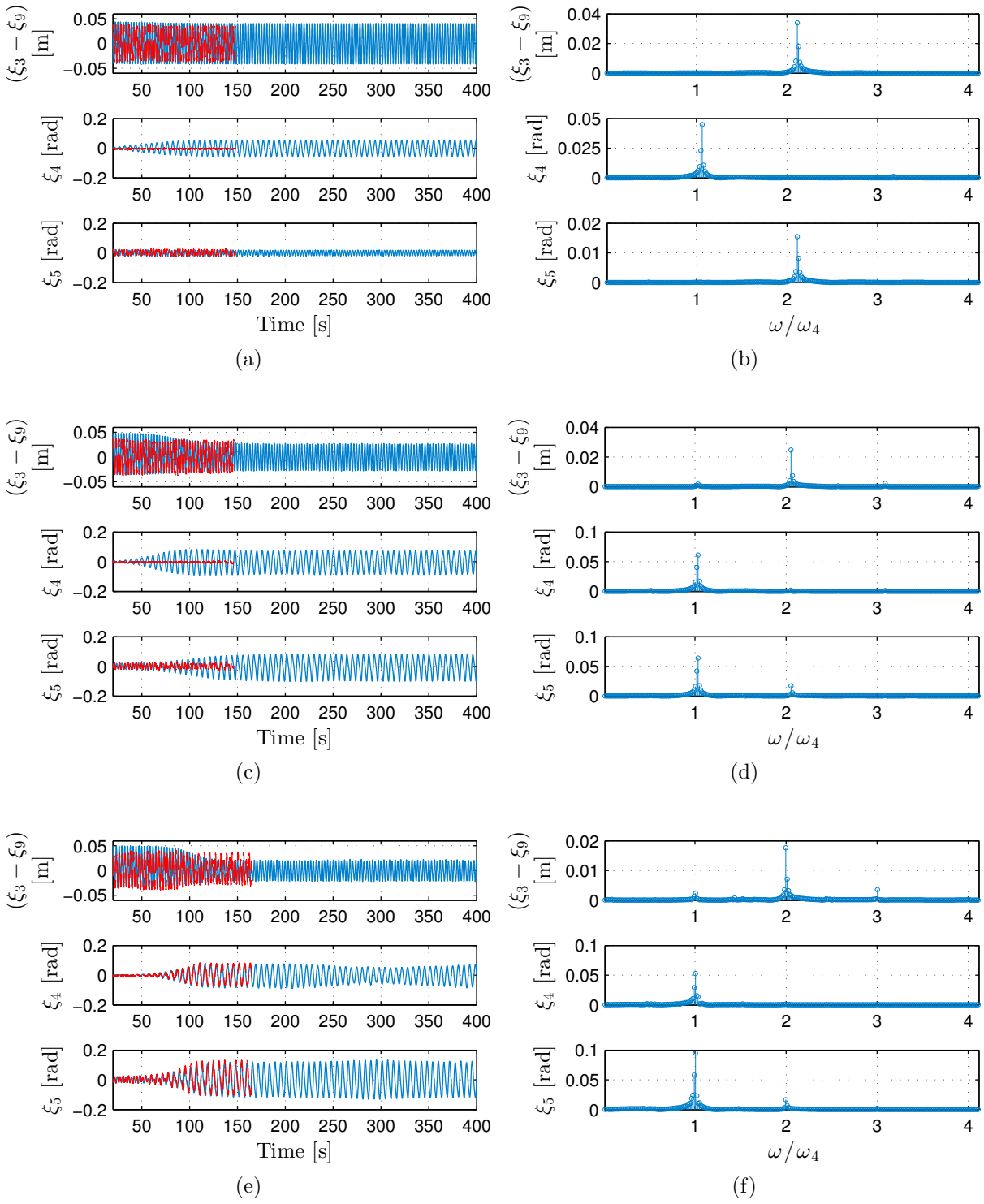

Figure 6.7: (a) Time series for test T24 (b) amplitude spectrum for test T24 (c) time series for test T25 (d) amplitude spectrum for test T25 (e) time series for test T26 (f) amplitude spectrum for test T26. Exp.(−−red), sim.(−blue)

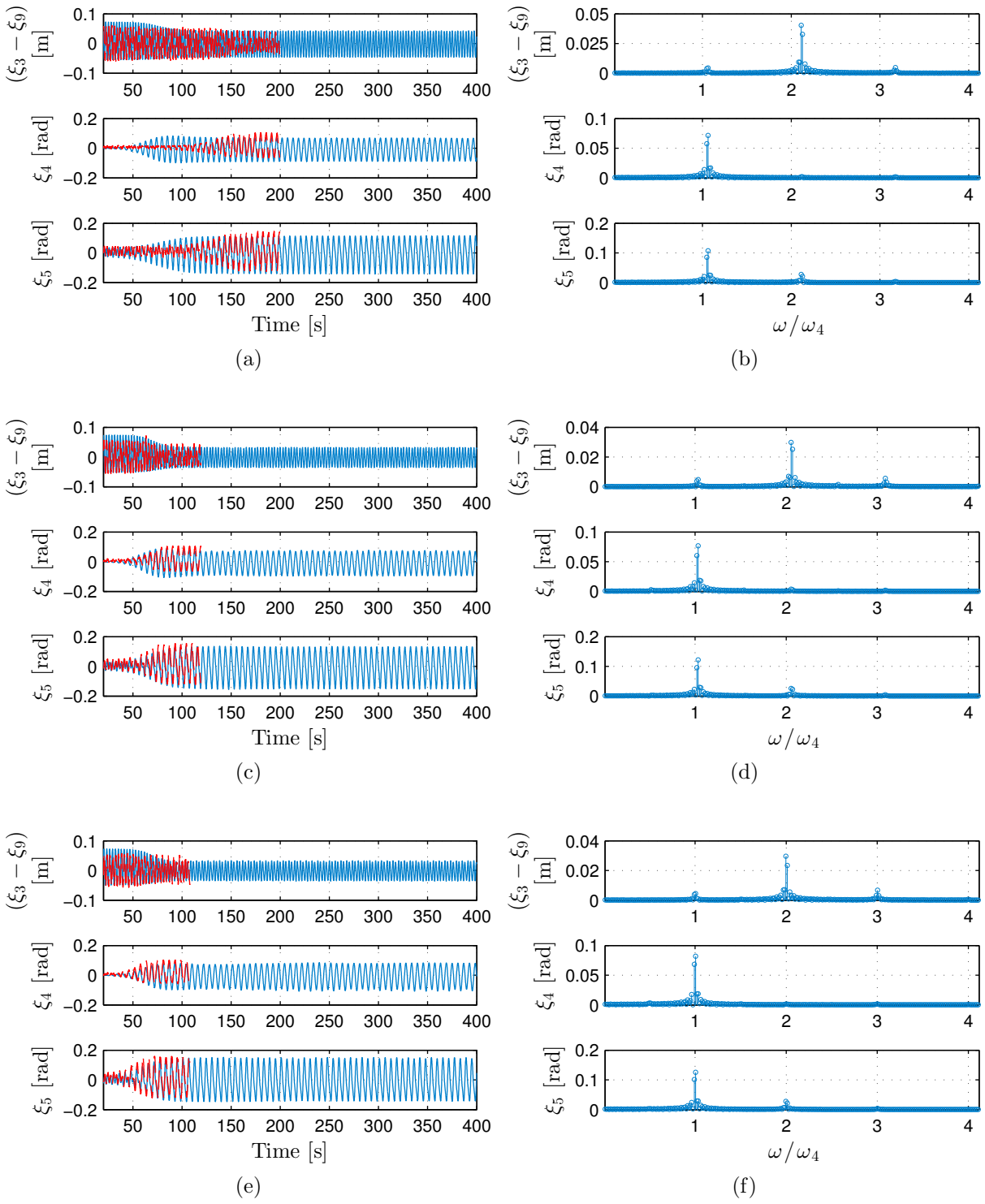

Figure 6.8: (a) Time series for test T27 (b) amplitude spectrum for test T27 (c) time series for test T28 (d) amplitude spectrum for test T28 (e) time series for test T29 (f) amplitude spectrum for test T29. Exp.(−−red), sim.(−blue)

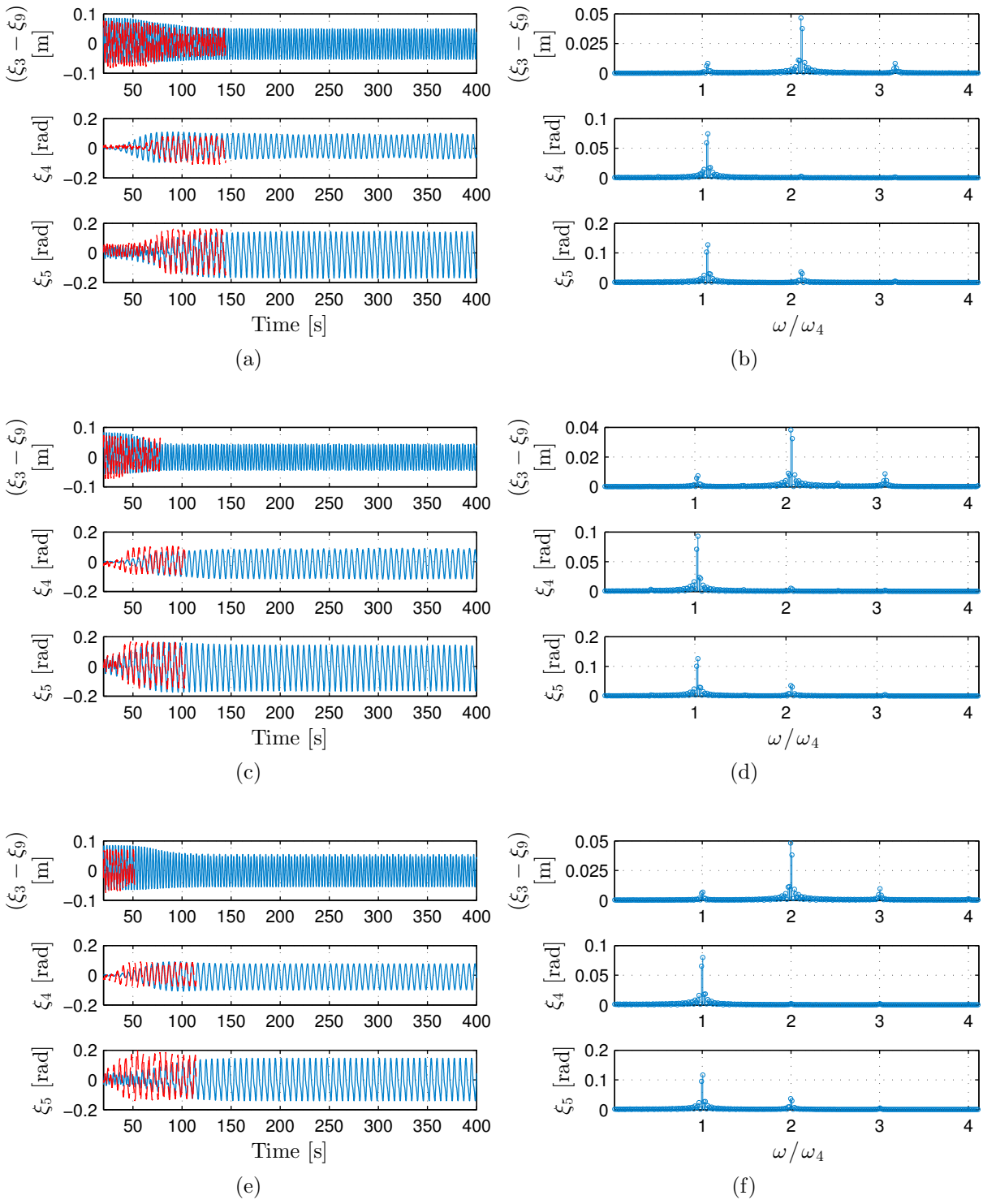

Figure 6.9: (a) Time series for test T30 (b) amplitude spectrum for test T30 (c) time series for test T31 (d) amplitude spectrum for test T31 (e) time series for test T32 (f) amplitude spectrum for test T32. Exp.(−−red), sim.(−blue)

6.3 Evidence of nonlinearity

To further illustrate the evidence of the strong nonlinear behaviour of the model due to parametric resonance, a series of numerical simulations were carried out for a range of wave excitation frequencies, from $\omega_e = 0.7012$ rad/s up to $\omega_e = 5.0265$ rad/s, in increments of 0.0048 rad/s. A constant wave amplitude of $\zeta_o = 0.05$m and a PTO damping coefficient of $B_{PTO} = 5000$ Ns/m was used for the tests. The amplitude spectra for this set of numerical tests are shown in the form of surface plots and waterfall plots, for the relative heave, roll and pitch modes, as shown in Figs. 6.10 - 6.12. It should be noted that the surface plot and the waterfall plot for a particular mode are simply different ways to present the data for visualisation purposes, with both methods using the same response data for that particular degree of freedom.

The relative heave motion spectra in Figs. 6.10(a) and (b) shows how the relative heave motion responds at the wave excitation frequency at the higher wave frequencies. As the excitation frequency reduces, the relative heave motion response increases as it approaches the tuning factor of 2. The heave resonance was calculated from free decay tests as 2.199 rad/s, corresponding to a tuning factor of 2.059. The relative heave has it's largest amplitude of response at frequencies slightly above and below the tuning factor of 2, due to heave resonance. At the tuning factor of 2, the relative heave motion is reduced as the model is undergoing parametric resonance. The energy input to the heave mode is transferred to the roll and pitch modes due to parametric resonance and nonlinear coupling with the roll and pitch modes, resulting in an overall reduction in the relative heave motion. At the tuning factor of 2, there is also evidence of heave response appearing at harmonics of the roll/pitch natural frequency in the relative heave spectrum, due to the nonlinear effect of parametric resonance. As the excitation frequency is further reduced below the tuning factor of 2, the relative heave motion response decreases. At the tuning factor of 1, which is equal to the roll/pitch natural frequency, the relative heave response has it's highest peak at the first harmonic of the roll/pitch natural frequency, corresponding to a normalised frequency response of $\omega/\omega_4 = 2$, with some level of response also taking place at the normalised frequency response of $\omega/\omega_4 = 1.5$. It is clear from the amplitude spectra for the relative heave motion, that the effect of nonlinearity is

significant at the parametric resonance tuning factors of 1 and 2, which have a drastic influence on the overall response of the device.

The surface plot and waterfall plot for the roll motion in Figs. 6.11 show almost zero response at the higher wave excitation frequencies as there is no direct external excitation of the roll motion in regular waves. The model shows large amplitude roll response at the tuning factors of 1 and 2, due to internal excitation from parametric resonance. There is also some level of response at the tuning factor of 1.5. In a fully linear analysis in regular waves, there would be no peaks appearing in the roll spectra for all wave excitation frequencies, as the surge, heave and pitch modes are uncoupled from the sway, roll and yaw modes.

The pitch spectra in Figs. 6.12 show mainly first order pitch response for all wave excitations except at the tuning factor of 2 where the device is undergoing parametric resonance. At the tuning factor of 2, there is some level of pitch response at the wave excitation frequency, however, the predominant peak is at the pitch natural frequency even though it is being excited at twice the pitch natural frequency. There is also some nonlinear response at the tuning factor of 1.5, with a large increase in pitch amplitude occurring at the tuning factor of 1, i.e., at pitch resonance.

To gain insight into how the frequency response of the device changes with time when it is being excited at the primary parametric resonance tuning factor of 2, a time-frequency analysis of the pitch motion was carried out, which is shown in Fig. 6.13. It can be seen that for the first 50s of the test, the model is pitching at the wave excitation frequency, and then as the onset of parametric pitch takes place, the pitch natural frequency becomes the dominant frequency. This shifting of the frequency response is a nonlinear effect which is captured well in the nonlinear numerical model.

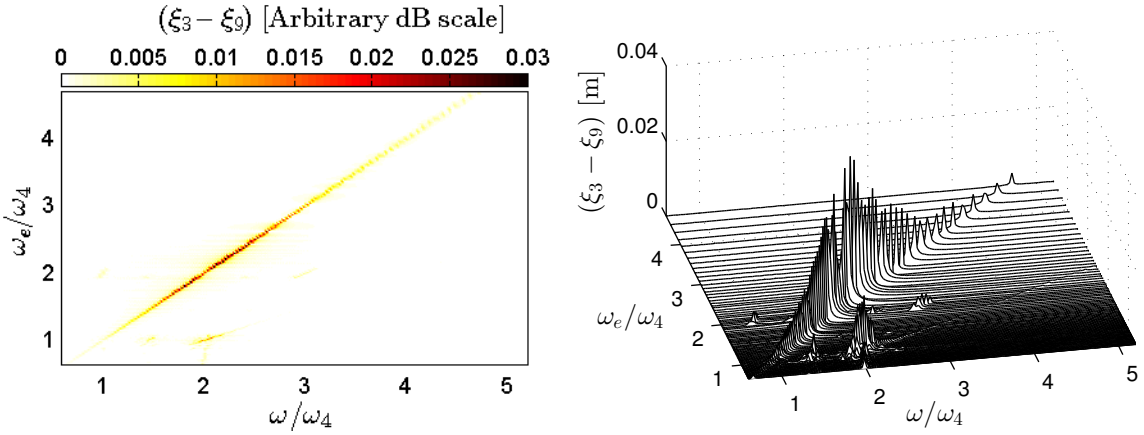

(a) (b)

Figure 6.10: Relative heave amplitude spectrum (a) surface plot (b) waterfall plot

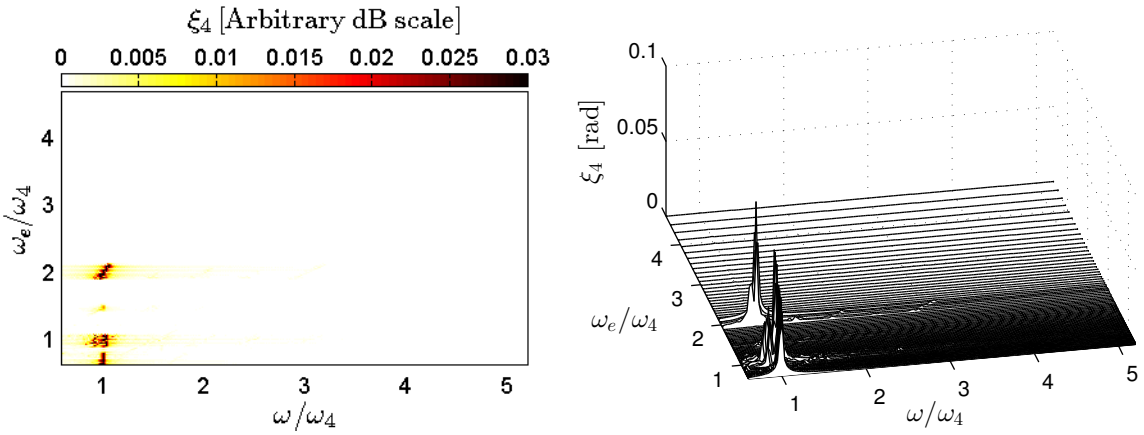

(a) (b)

Figure 6.11: Roll response amplitude spectrum (a) surface plot (b) waterfall plot

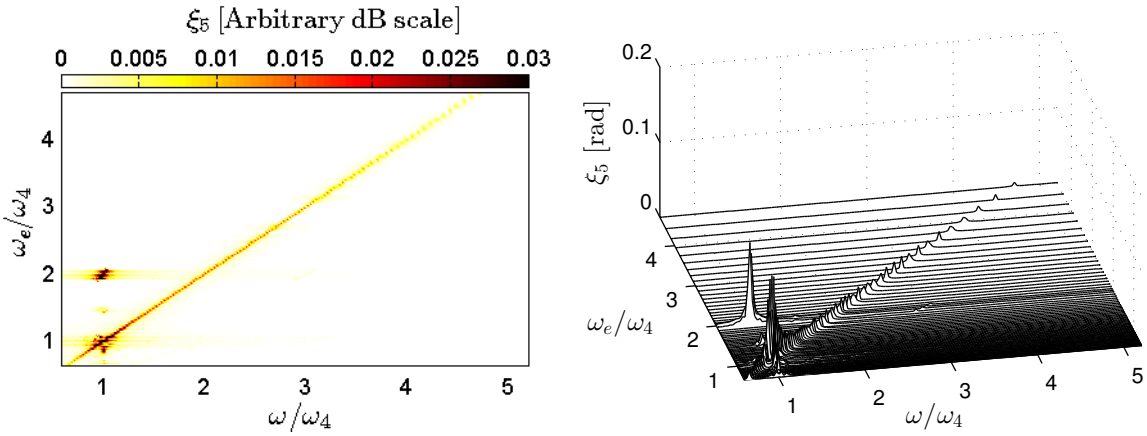

(a) (b)

Figure 6.12: Pitch response amplitude spectrum (a) surface plot (b) waterfall plot

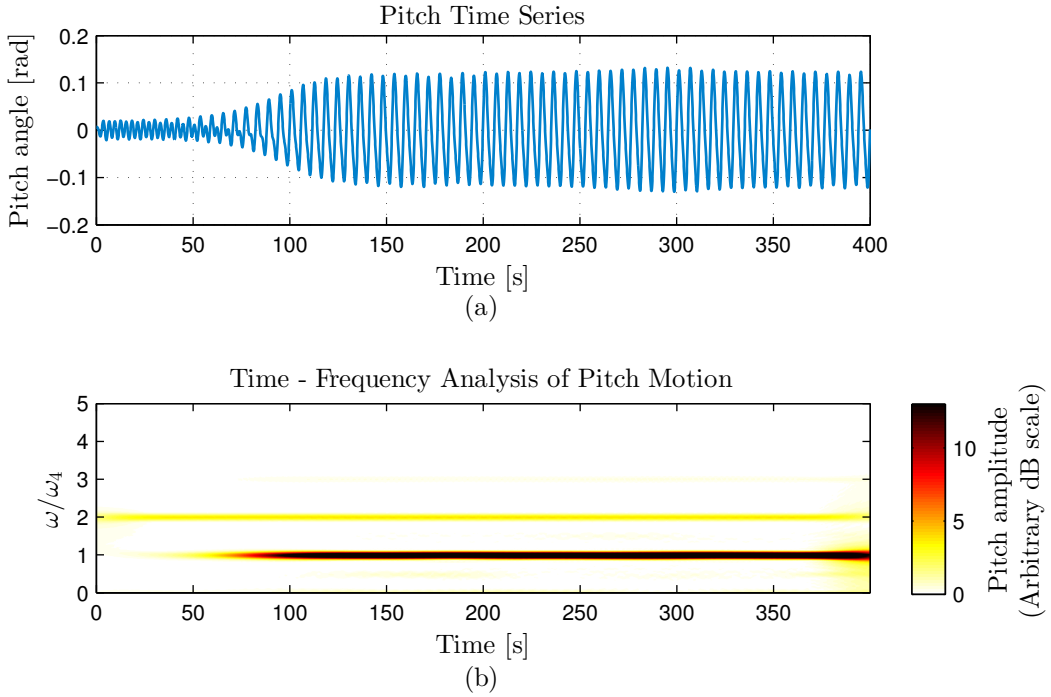

Figure 6.13: Test T26 ($\omega/\omega_4 = 2$, $\zeta_o = 0.05$m) (a) pitch time series (b) time-frequency analysis of pitch motion

6.4 Limits of stability

The results form Section 6.1 and 6.2 have demonstrated that the numerical model shows good comparisons with the experimental results for the range of wave excitation frequencies and wave amplitudes considered in the analysis. To gain further insight into the complexities of parametric resonance of the device, the numerical model was used to identify the limits of stability in the roll and pitch modes for a wide range of wave excitation frequencies and wave amplitudes. The effect of PTO damping coefficient was also investigated to see how this parameter affects the responses.

The limits of stability are presented in Figs. 6.14 - 6.16 for the roll and pitch motion for three different PTO damping coefficients of B_{PTO} = 3000 Ns/m, 4000 Ns/m and 5000 Ns/m. In the plots for the limits of stability, each point in the map corresponds to a different numerical simulation, while the colour intensity of the point signifies the steady state amplitude of the response. The advantage of displaying the limits of stability in this way are that we not only get the regions of instabilities, but we also get an idea of the steady state amplitude reached when parametric resonance occurs.

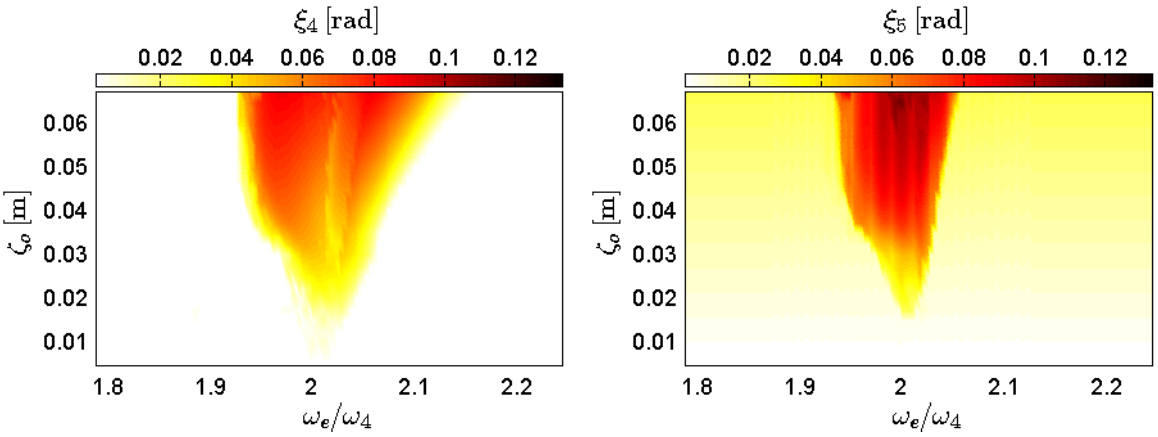

(a) (b)

Figure 6.14: Limits of stability with $B_{PTO} = 3000$ Ns/m for (a) roll mode (b) pitch mode

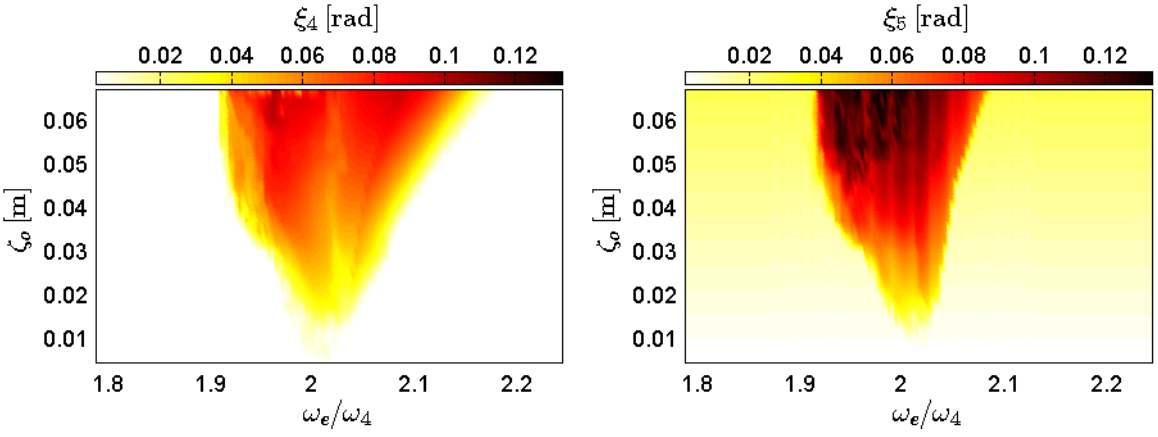

(a) (b)

Figure 6.15: Limits of stability with $B_{PTO} = 4000$ Ns/m for (a) roll mode (b) pitch mode

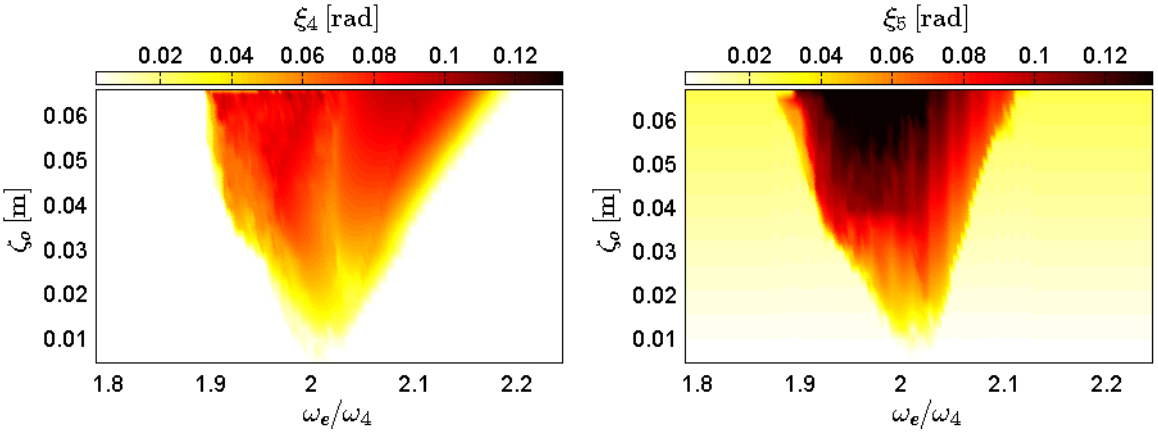

(a) (b)

Figure 6.16: Limits of stability with $B_{PTO} = 5000$ Ns/m for (a) roll mode (b) pitch mode

The roll response limits of stability reveal that the zone of instability first takes place for very small amplitude waves for all three PTO damping coefficients. Parametric roll first begins at a tuning factor of 2 with the region of instability progressively widening as the wave amplitude increases. Outside the instability zone, the roll has almost zero response and is considered a stable zone. The effect of increasing the PTO damping is to widen the zones of instability and to increases the steady state roll oscillations for a given wave amplitude. The regions of instability in the roll mode tend to bend towards the right for higher wave excitation frequencies, which becomes more pronounced as the PTO damping coefficient is increased. This behaviour is due to nonlinear stiffening of the system which is more significant for higher waves.

It can be seen that the level of PTO damping has more of an influence on the pitch motion than the roll motion in relation to the wave excitation amplitude at which parametric motion first occurs. The wave amplitude at which the pitch instability first occurs is $\zeta_o =$ 0.0175m for a PTO damping coefficient of $B_{PTO} = 3000$ Ns/m, with this value reducing to $\zeta_o = .0125$m and then $\zeta_o = 0.01$m for PTO damping coefficients of $B_{PTO} = 4000$ Ns/m and $B_{PTO} = 5000$ Ns/m respectively. Similar to what was observed in the roll limits of stability, the effect of increasing the PTO damping is to widen the width of the regions of instability and also to increases the steady state pitch oscillations for a given wave amplitude. In contrast to the roll limits of stability, the regions outside the pitch unstable zones have a significant response, as the pitch motion is being externally excited in regular waves. However, as the device is not being parametrically excited in these zones, they are considered stable.

The appearance of the unstable areas in the limits of stability for the roll and pitch motions resembles the first Mathieu unstable zone which was also observed by Rodríguez and Neves [67] in their work on parametric roll of spar platforms in waves. They point out that the shape of these unstable zones are different as to what is observed in the case of conventional ship forms, where the unstable zones are larger and have upper frontiers that do not exist in the case of spar platforms or the point absorber in the current work. It is interesting to note that when the model is undergoing parametric resonance, the roll and pitch modes become more unstable as the level of PTO damping is increased. This is not intuitive as you would expect that the response amplitudes would reduce, as there is

more damping in the system. However, the PTO damping only provides a damping in the relative heave degree of freedom, and although the relative heave motion decreases with an increase in PTO damping, this is clearly not the case for the roll and pitch modes.
To illustrate the effect of the PTO damping on the relative heave, roll and pitch modes at parametric resonance, a set of numerical simulations were carried out at a constant wave amplitude of $\zeta_o = 0.025$m and a constant normalised wave excitation frequency of $\omega_e/\omega_4 = 2$. The PTO damping coefficient was increased for each test, with the maximum steady state response then plotted against the corresponding PTO damping coefficient as shown in Fig. 6.17. It can be seen that by increasing the PTO damping, the relative heave response reduces, as would be expected, however, the roll and pitch responses steadily increase with more damping being input into the heave mode. This is useful information when designing the survivability mode of the device in large wave conditions. In the survivability mode, the device is locked, so that there is no relative motion between the torus and FNT. This is achieved by providing a large damping from the PTO in the relative heave degree of freedom. The purpose of this is to prevent the device from being damaged in large waves and storm conditions. In such wave conditions, if the device was not locked, the torus superstructure would be likely to strike the endstops on the device due to excessive relative heave motion, resulting in structural damage. However, although an increase in PTO damping will reduce the relative heave motion, the limits of stability reveal that the device will become more unstable in parametric resonance conditions as the level of PTO damping is increased, which could result in excessive roll and pitch angles resulting in damage to the structure.

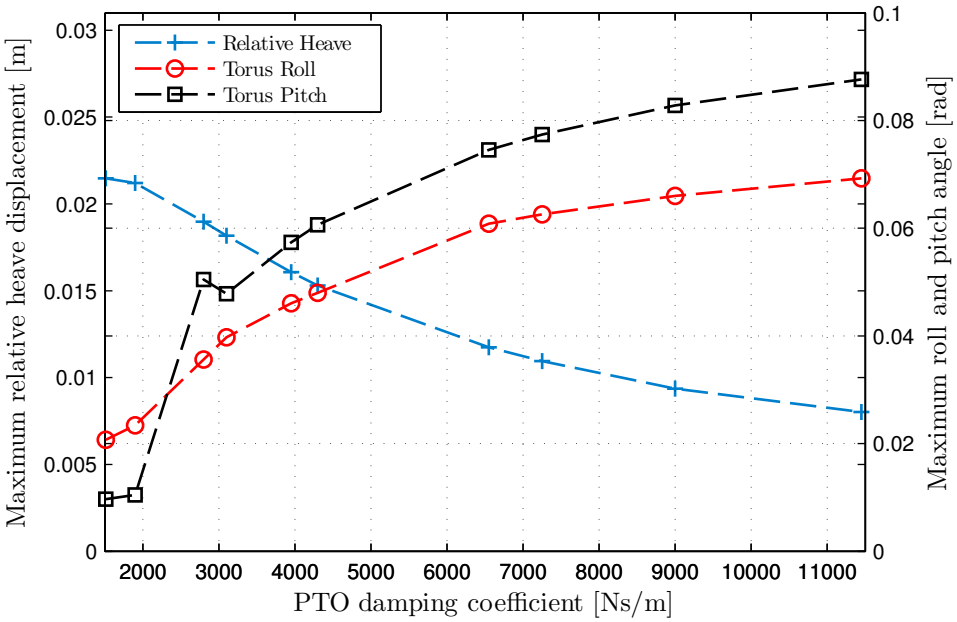

Figure 6.17: Variation of maximum relative heave displacement, maximum roll angle and maximum pitch angle for various PTO damping coefficients, ($\omega/\omega_4 = 2$, $\zeta_o = 0.025$m)

6.5 Influence of initial conditions

All of the numerical simulations which were carried out in Section 6.1 - 6.4 started with an initial roll and pitch angle of 0.007 rad. To get an idea of how the model responds to different initial pitch angles at parametric resonance conditions, numerical simulations of the test conditions in test T26 ($\omega/\omega_4 = 2$, $\zeta_o = 0.05$m, $B_{PTO} = 5000$ Ns/m) of Table 6.2 were carried out for four different initial pitch angles. The time traces and phase diagrams for these four tests are shown in Fig. 6.18. The phase diagram plots two of the state variables, displacement and velocity in this case, where each state variable is given an initial condition. The phase diagram is useful for analysing the qualitative behaviour of a second-order system over time. They are particularly useful for analysing nonlinear systems, as nonlinear systems often have multiple steady state solutions. Phase diagrams can therefore provide an understanding of which steady state solution a particular set of initial conditions will converge to. The solid blue dot in each of the phase diagrams in Fig. 6.18 represents the initial pitch angle for that particular test. All tests had an initial velocity of 0 rad/s.

The phase diagrams are elliptic in shape at low amplitude pitch angles after transients

have died out, and then begin to resemble a kidney shape at large pitch angles. This kidney shaped phase plane is typical of a nonlinear system, as it shows the appearance of higher harmonics in the response at high amplitudes. It can be seen from the time traces of the four tests in Fig. 6.18, that the pitch motion reaches roughly the same steady state amplitude of approximately 0.14 radians after around 100s in each test. To see this more clearly, the phase diagrams for all four tests are plotted together in Fig. 6.19. This phase diagram represents a stable limit cycle since the pitch trajectories tends to converge to a limit cycle for all four tests. This phase diagram also suggests that the system does not display hysteresis since the solution tends to the limit cycle, regardless of whether the initial conditions begin from inside, or outside the limit cycle, meaning that there appears to be no metastable state. This is useful information as it tells us that the pitch response will converge to a steady state solution when the device undergoes parametric resonance for a particular wave height subject to arbitrary initial pitch conditions.

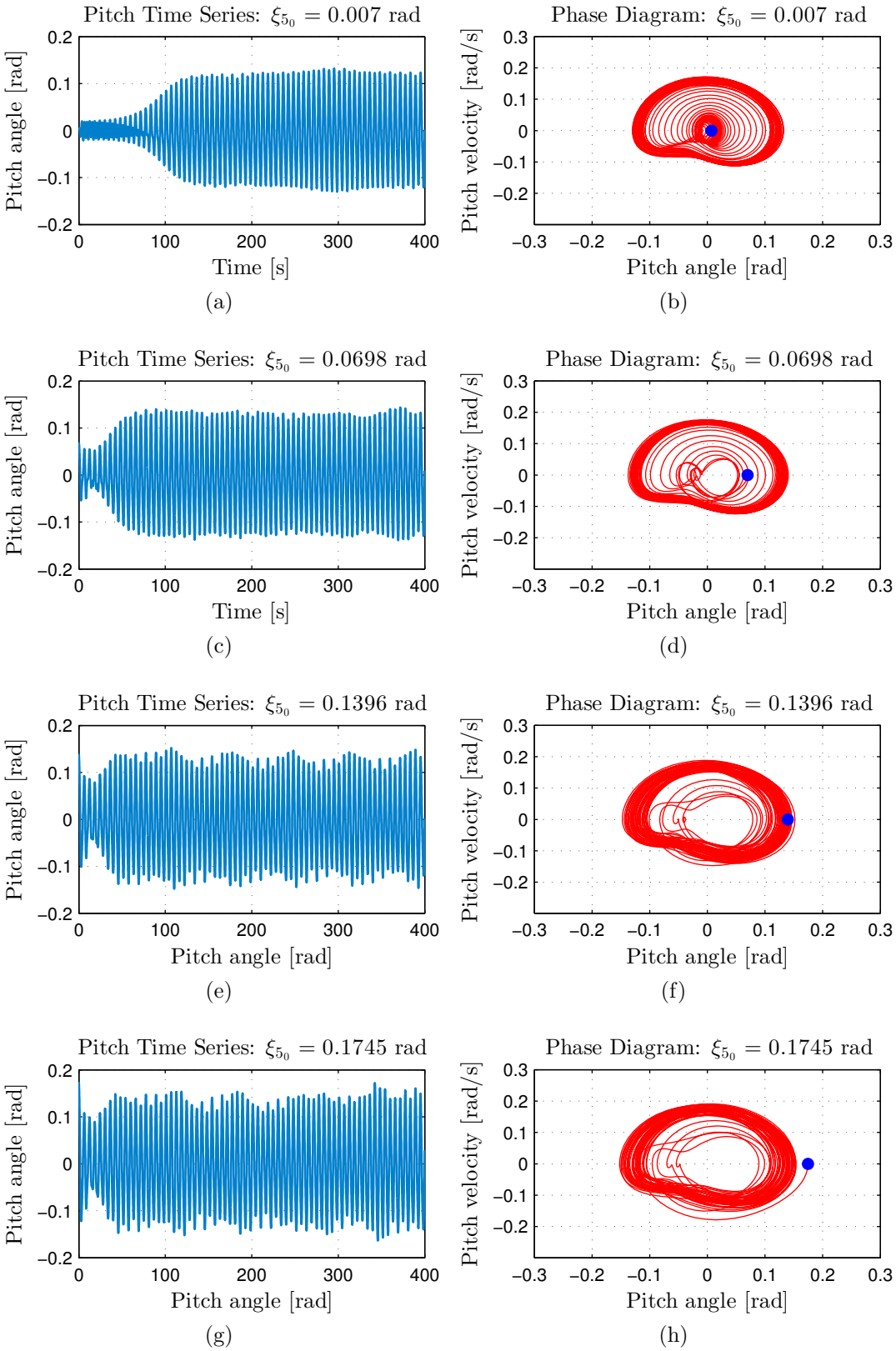

Figure 6.18: Test T26 pitch times series and phase diagrams subject to various initial conditions: (a) - (b) $\xi_{5_0} = 0.007$ rad (c) - (d) $\xi_{5_0} = 0.0698$ rad (e) - (f) $\xi_{5_0} = 0.1396$ rad (g) - (h) $\xi_{5_0} = 0.1745$ rad

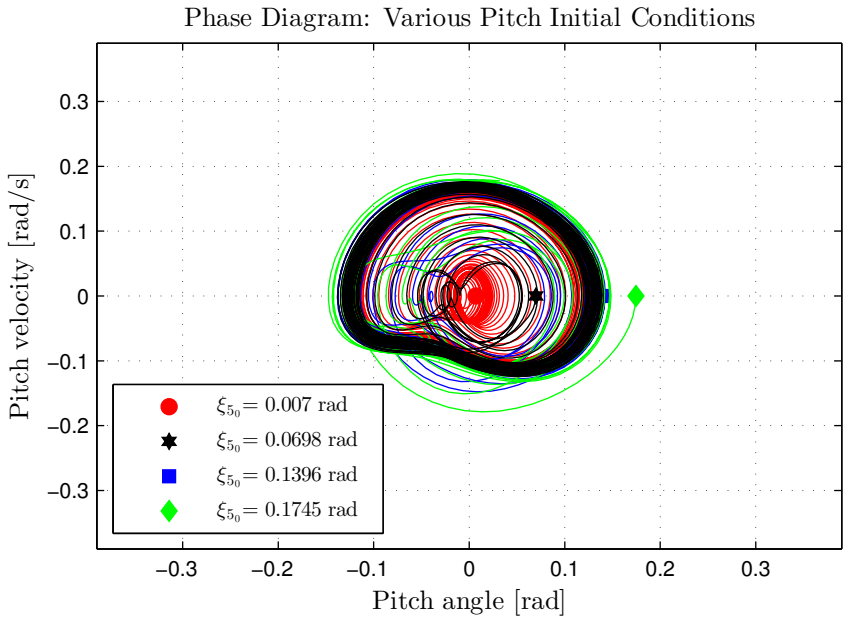

Figure 6.19: Test T26 phase plane diagram for a range of initial pitch angles using numerical simulation

Chapter 7

Results in irregular waves

7.1 Introduction

As outlined in Chapter 2, a knowledge of the response and characteristics of a point absorber WEC in regular waves is an important step in the overall design and development of the device. However, such waves do not occur in the real ocean environment, as the wave length between two successive crests, or troughs, and also the vertical distance between a crest and a trough, vary continuously. Therefore, to get a more realistic understanding of how a point absorber behaves while at sea, it is necessary to carry out numerical simulations of the device in irregular waves. The term irregular waves will be used to denote the natural sea states in which the wave characteristics are expected to have a statistical variability—in contrast to regular waves, where the properties may be assumed to be constant.

An irregular wave analysis is also important to ascertain whether or not a point absorber is susceptible to parametric motion in irregular seas, and if so, if the behaviour of the phenomenon is similar to that which occurs in regular waves. Parametric roll has been proven to be a dangerous phenomenon for several categories of ships occurring in realistic sea states, as outlined by France et al. [46]. In particular, it is to be noted that the occurrence of parametric roll of ships in irregular seas is much more dangerous and subtle than the same phenomenon in regular seas. This is due to the fact that when the parametric excitation is random, the build-up of roll can occur suddenly and abruptly after very long periods of quiescence, with a fast increase in the roll amplitude after only a few roll cycles [68]. Based upon these observations, it is of interest to deduce if a similar behaviour

of the phenomenon occurs in parametric resonance of point absorbers in irregular waves.

7.2 Irregular wave model

The realistic assessment of the motion response of the device in irregular waves requires a suitable model for the real ocean environment. Irregular waves can be classified as either long crested or short crested based upon the direction of wave propagation. If the irregularities of the observed waves are only in the dominant wind direction, so that there are mainly mono-directional wave crests with varying separation but remaining parallel to each other, the sea is referred to as a long crested irregular sea. When irregularities are apparent along the wave crests at right angles to the direction of the wind, the sea is referred to as short crested. Throughout this chapter the sea state will be considered long crested. An example is shown in Fig. 7.1 of a long crested and a shorted crested sea.

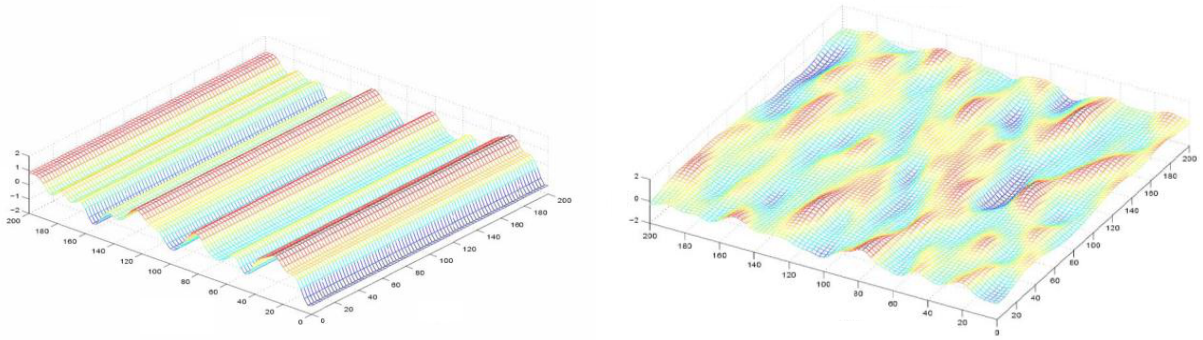

(a) (b)

Figure 7.1: 3D view of (a) a long crested sea simulation and (b) a shorted crested sea simulation

To generate long crested waves, it is considered that they can be represented by a linear superposition of a discrete number of N regular wave components, each having different amplitude, frequency, and phase angle. The wave elevation time series can therefore be represented as

$$\zeta_w(x,t) = \sum_{n=1}^{N} \zeta_{no} \cos(k_n x - \omega_n t + \theta_n) \tag{7.1}$$

where θ_n is the phase component (between $0 - 2\pi$) of component n, with amplitude ζ_{no}

and wave number k_n. The equally spaced frequencies are given by $\omega_n = 2\pi n/T_H$, where T_H is the length of the time history.

The wave spectrum is a useful tool for taking into account the irregularity of the waves, as any given seaway can be described by the energy distribution for various wave components. Within the approximations which linear theory is based upon, the wave spectrum gives us all the properties we need to define a sea state. By re-writing Eqn. 2.1 in terms of wave amplitude, the equation for the energy per square meter of the sea surface of the nth wave component is

$$E = \frac{\rho g \zeta_{no}^2}{2} \tag{7.2}$$

The ordinates of the wave spectrum are represented by the symbol $S_\zeta(\omega_n)$ and are given by

$$S_\zeta(\omega_n) = \frac{\zeta_{no}^2}{2\delta\omega} \tag{7.3}$$

where $\delta\omega$ is the fixed interval between frequencies. Therefore, from Eqn. 7.2, the total energy per square meter of the wave system is equal to the total area enclosed by the wave spectrum multiplied by the factor ρg.

The inverse transformation can also be made in order to generate a time history according to Eqn. 7.1 from a given wave spectrum. The amplitude of the nth component sinusoidal wave is given by

$$\zeta_{no} = \sqrt{2S_\zeta(\omega_n)\delta\omega} \tag{7.4}$$

Therefore, the time history of wave elevation is obtained by substituting Eqn. 7.4 into Eqn. 7.1 such that

$$\zeta_w(x,t) = \sum_{n=1}^{N} \sqrt{2S_\zeta(\omega_n)\delta\omega} \cdot \cos(k_n x - \omega_n t + \theta_n) \tag{7.5}$$

Fig. 7.2 provides a visual representation of how an irregular wave profile is derived from a wave spectrum.

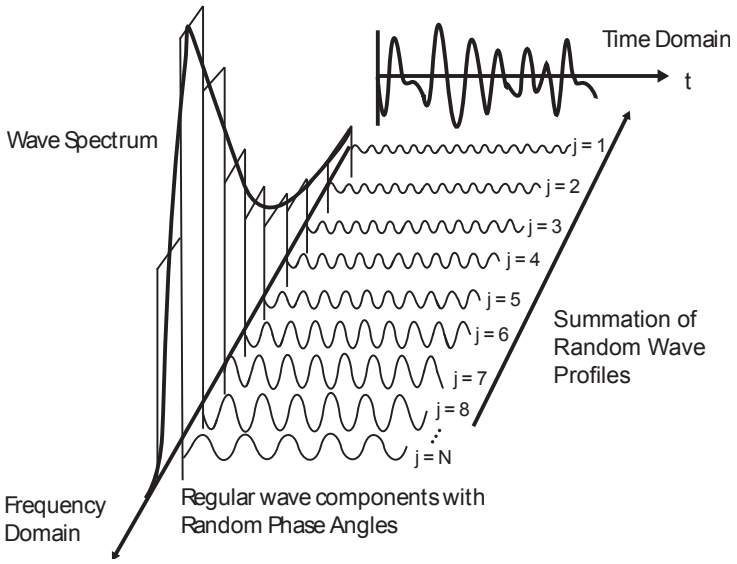

Figure 7.2: The principal of creating an irregular ocean wave time series from the superposition of several regular waves derived from a wave spectrum [69]

The wave spectrum used in the current work is the JONSWAP (Joint North Sea Wave Project) spectrum. The JONSWAP spectrum was established during a joint research project in the North Sea and is presented in the literature by Hasselmann et al. [70]. The data collected from the project indicated that the sea was never fully developed. A fully developed sea exists in conditions where there is sufficient fetch available, and the wind blows at a constant velocity for long enough such that the rate at which energy is absorbed by the waves will eventually be exactly balanced by the rate of energy dissipation. The waves in the JONSWAP spectrum thus continue to grow with distance (or time). The spectral ordinate of the JONSWAP spectrum is defined as

$$S_{J\zeta}(\omega) = \frac{\alpha g^2}{\omega^5} \exp\left[-1.25\frac{\omega_p^4}{\omega^4}\right] \gamma^a \tag{7.6}$$

where

$$a = \exp\left[-\frac{(\omega - \omega_p)^2}{2\omega_p^2\sigma^2}\right]$$

and

$$\sigma = \begin{cases} 0.07 & \text{if } \omega \leq \omega_p \\ 0.09 & \text{if } \omega > \omega_p \end{cases}$$

The parameter γ in Eqn. 7.6 is called the peak-enhancement factor, the effect of which is to increase the peak of the spectrum. The other parameters to define the sea state

are the peak frequency; $\omega_p = 2\pi/T_p$, which is the frequency with the maximum value in the spectrum; T_p, which is the peak period of the sea state; and H_s, the significant wave height which is defined as the average height of the highest one-third wave peaks in a wave spectrum. The parameter α in Eqn. 7.6 is included to take into account the growth of the waves with distance. An example of the JONSWAP spectrum is shown in Fig. 7.3(a), where it is plotted along with a Bretschneider spectrum for comparison. The Bretschneider spectrum is another commonly used spectrum to represent the conditions which occur in the open ocean. It can be seen that the JONSWAP spectrum has a higher peak due to the peak enhancement factor γ associated with the spectral ordinates of the JONSWAP spectrum in Eqn. 7.6.

Statistical methods are used to quantify the response of the device in irregular wave simulations. In order to use these methods, the motion response spectrum must firstly be obtained. The motion response spectrum for the translational motion (surge, sway and heave) is calculated by filtering the wave energy spectrum with the motion transfer function. The translational motion transfer function is defined as the motion amplitude divided by the wave amplitude in the particular degree of freedom for each wave frequency. The filtering procedure is is achieved by multiplying each ordinate of the wave spectrum $S_\zeta(\omega)$ by the square of the translational motion transfer function at the corresponding wave frequency. Note that in order to distinguish the wave spectrum from the motion response spectrum, the ordinates of the motion response spectrum are denoted by S_{ξ_j}, corresponding to the particular degree of freedom ξ_j. The motion response energy spectrum ordinate at each wave frequency for the translational degrees of freedom ($\xi_j,\ j = 1, 2, 3$) of a single body system is given by

$$S_{\xi_j}(\omega) = S_\zeta(\omega) \left(\frac{\xi_j}{\zeta_o}(\omega) \right)^2 \tag{7.7}$$

A similar procedure is followed to calculate the motion response spectra for the angular motion responses (roll, pitch and yaw), except that the transfer functions are normalised by dividing by the wave slope amplitude $k\zeta_o$. Also, the wave slope spectrum $S_\alpha(\omega)$ is used instead of the wave energy spectrum $S_\zeta(\omega)$ for calculating the motion response spectrum in the case of the rotational modes. The wave slope spectrum is given by

$$S_\alpha(\omega) = \frac{\omega^4}{g^2} S_\zeta(\omega) \tag{7.8}$$

An example of a JONSWAP and a Bretschneider wave slope spectrum is illustrated in Fig. 7.3(b), where it can be seen that there is greater energy at the higher frequencies than the corresponding wave energy spectra in Fig. 7.3(a), for the same parameters in the spectrum. This is due to the fact that short high frequency waves are usually very steep even though their amplitudes are small. The motion response energy spectrum for the roll, pitch and yaw degrees of freedom ($\xi_j,\ j = 4, 5, 6$) of a single body system is then given by

$$S_{\xi_j}(\omega) = S_\alpha(\omega) \left(\frac{\xi_j}{k\zeta_o}(\omega) \right)^2 \tag{7.9}$$

where $k = \omega^2/g$ is the wavenumber as defined in Eqn. 3.21. The variance, m_{o_j}, of the response motion in degree of freedom j is obtained by integrating the motion energy spectrum according to

$$m_{o_j} = \int_0^\infty S_{\xi_j}(\omega) d\omega \tag{7.10}$$

The root-mean-square (rms) of the motion in degree of freedom j is then given as

$$\xi_{j_{rms}} = \sqrt{m_{o_j}} \tag{7.11}$$

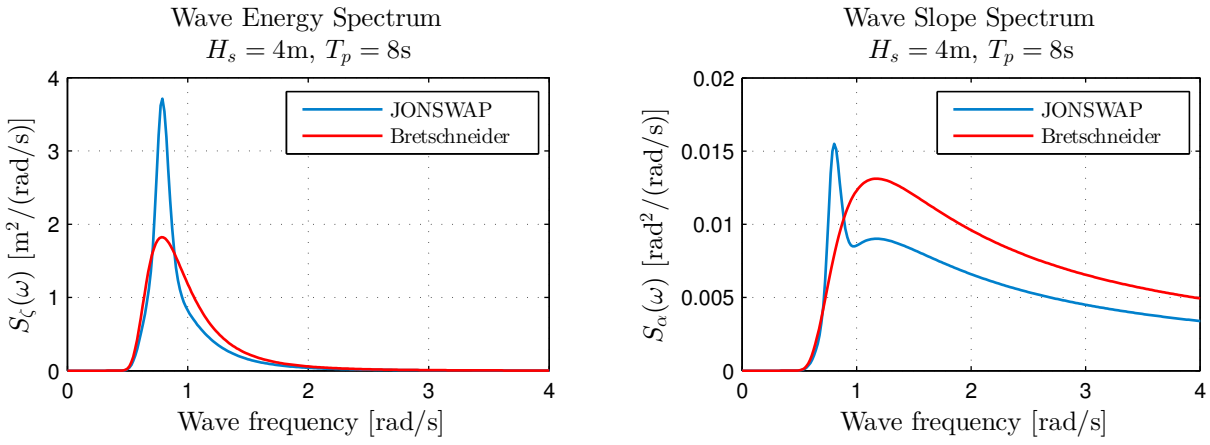

Figure 7.3: (a) JONSWAP and Bretschneider wave energy spectrum (b) JONSWAP and Bretschneider wave slope spectrum

7.3 Simulations in irregular waves

Since there was no experimental data for irregular waves available from the tests at ECN, it was decided to carry out numerical simulations of SML17 in irregular long crested waves using the nonlinear numerical model to investigate the response of the device in such conditions. Three tests were carried out at a significant wave height of $H_s = 0.2$m according to the test conditions outlined in Table 7.1. The tuning factor is shown in the fifth column of Table 7.1, which is defined for irregular waves as the ratio of the peak wave frequency to the roll natural frequency (ω_p/ω_4). This set of tests were chosen as they correspond to a low period wave (test T33), a wave at the parametric resonance tuning factor of 2 (test T34) and a high period wave (test T35).

The time traces for the relative heave, roll and pitch motions for the three tests are presented in Figs. 7.4(a) - (c) respectively. The corresponding wave energy spectra, transfer functions and motion response energy spectra for the same tests are shown in Figs. 7.5 - 7.7. Since only long crested waves are considered in this analysis, there is no direct wave excitation in the roll mode. Since there is no roll excitation, and hence no roll transfer function, only the roll motion response energy spectrum is presented for each test, which is calculated as the spectral density of the roll response.

In Fig. 7.5(a) (test T33), it is seen that the the frequency range of greatest wave energy content ($\omega_p = 5.027$ rad/s) is quite far from the heave natural frequency of 2.199 rad/s. For this reason, a small amount of the wave energy is transferred into first order heave motion, as observed from the relative heave transfer function and relative heave energy spectrum. Also, in Fig. 7.5(b), the frequency range of greatest wave energy content is far from the pitch natural frequency of 1.068 rad/s. Therefore, the pitch transfer function and pitch energy spectrum show almost zero first order motion, with most of the energy occurring at the pitch natural frequency. From Fig. 7.5(c), it is seen that the roll motion for this test shows a significant response, even though the roll is not being directly excited. The tuning factor of 4.7059 for this test is far from the primary region of parametric resonance, however, as the system is being excited by broadband excitation, there will always be some level of parametric excitation at twice the roll natural frequency, which accounts for the roll response in this test.

For test T34, at the parametric resonance tuning factor of 2, the *rms* of the relative heave is over six times greater than that of the previous test (test T33), since the peak of the wave energy spectrum for this test condition (ω_p = 2.137 rad/s) is located around the heave natural frequency of 2.199 rad/s. Therefore, a large amount of the wave energy is transferred to the heave motion, as shown in Fig. 7.6(a).

The corresponding time trace for this test (test T34) in Fig. 7.4(b) reveals evidence of parametric roll occurring, as seen from the sudden bursts of roll motion taking place, in particular at around 1400 seconds, where the roll angle reaches a maximum amplitude of .07 radians. The roll motion energy spectrum for test T34, in Fig. 7.6(c), shows that the *rms* of the roll is over twice the value it was in test T33 at the lower period of 1.25s, whereas the maximum value of the spectral ordinate in the roll motion energy spectrum is over five times greater than what it was in test T33. In Fig. 7.6(b), it can be seen that the pitch motion *rms* is almost the same in this test as it was in test T33, although there is slightly more first order pitch motion taking place in test T34, at a wave peak period of 2.94s. However, most of the energy for the pitch motion is again, at the pitch natural frequency.

In test T35 there is a slight reduction in the relative heave compared to test T34, however, the heave mode is still absorbing a large amount of the wave energy as shown in Fig. 7.7(a), due to the fact that the wave energy peak frequency (ω_p = 1.887 rad/s) is still close to the heave natural frequency. The roll *rms* is half the value it was in test T34, as there is less frequency content at twice the roll natural frequency, and hence less parametric excitation occurring in this test.

The most striking difference between the irregular wave tests and the regular wave tests is in the roll motion. For the three wave periods tested in long crested waves, there is always a steady roll response at the roll natural frequency, with the greatest amplitudes occurring at the wave tuning factor of 2 (test T34). In irregular waves, there is always going to be a significant level of roll response occurring, even though there is no direct wave excitation in the roll mode. As explained above, there will always be frequency content occurring at twice the roll natural frequency due to broadband excitation. This is different from the case in regular waves, where we only saw significant roll response taking place in waves at and around the tuning factors of 1 or 2. For waves outside these

unstable zones, the roll response was almost zero. In the case of the pitch mode, we saw that we were getting predominantly first order pitch response in regular waves for all wave excitation frequencies, except at wave excitation frequencies at and around the tuning factor of 2, where the pitch responded mainly at the pitch natural frequency due to parametric motion. In the case of long crested waves, we see that most of the pitch motion energy is concentrated at the pitch natural frequency, not just at the tuning factor of 2 but also at tuning factors of 4.7059 and 1.7665. Similar to the roll mode, there will always be some level of excitation at twice the pitch natural frequency due to broadband excitation, and hence, there will always be some level of parametric pitch taking place.
A time-frequency analysis of test T34 is shown in Figs. 7.8 to understand how the response spectrum of the different modes evolve over time. The tuning factor for this test is 2, and we can see that the roll motion responds mainly at it's own natural frequency for the duration of the test. For the first 200s, the pitch motion is responding with a low amplitude, at both the wave excitation frequency and the pitch natural frequency. After 200s, the largest pitch response amplitude is at the pitch natural frequency, which is typical of parametric motion. The heave motion in this test is responding at the wave peak frequency ($\omega_p = 2.137$ rad/s) and at the heave natural frequency of 2.199 rad/s.

Test No.	H_s [m]	T_p [s]	ω_p [rad/s]	ω_p/ω_4	B_{PTO} [Ns/m]
T33	0.2	1.25	5.027	4.7059	5000
T34	0.2	2.94	2.137	2	5000
T35	0.2	3.33	1.887	1.7665	5000

Table 7.1: Experimental conditions in long crested waves

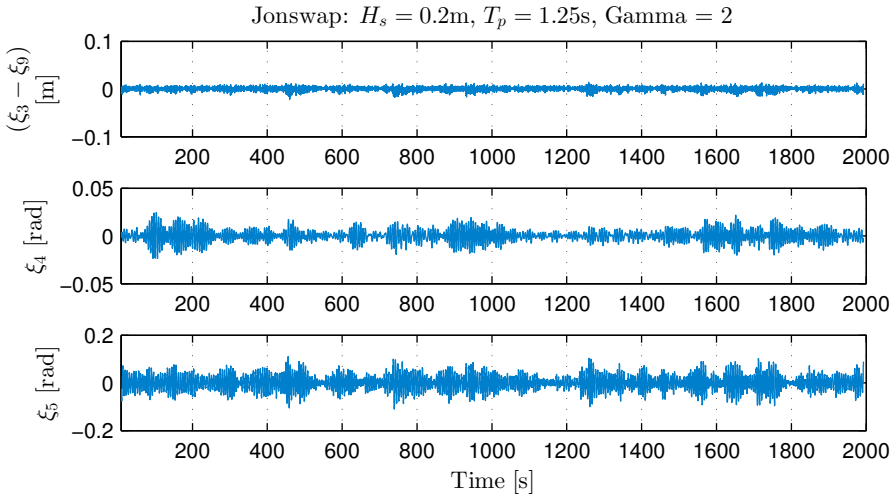

(a) Time series for test T33

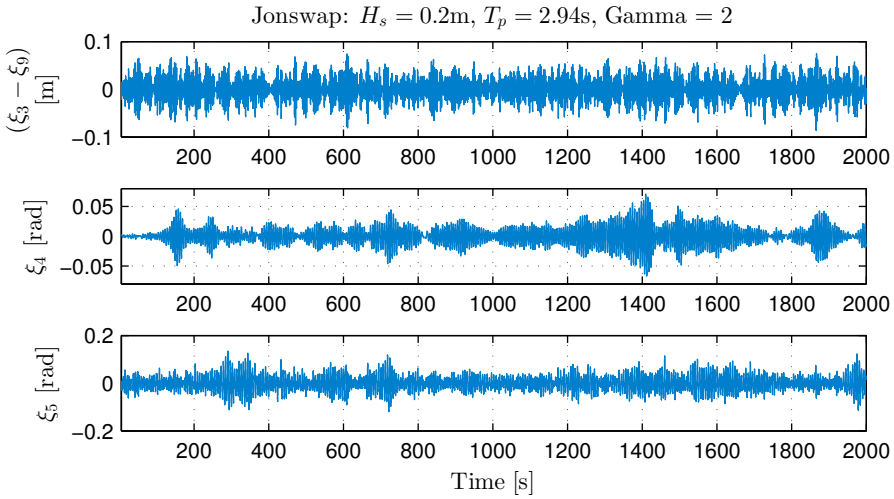

(b) Time series for test T34

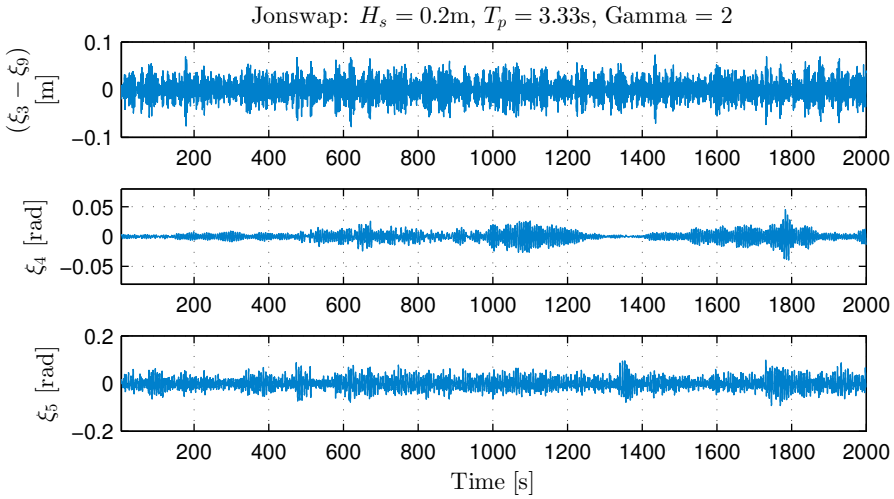

(c) Time series for test T35

Figure 7.4: Time series of relative heave, roll and pitch motion for $H_s = 0.2$m and $B_{PTO} = 5000$ Ns/m (a) $T_p = 1.25$s (b) $T_p = 2.94$s (c) $T_p = 3.33$s

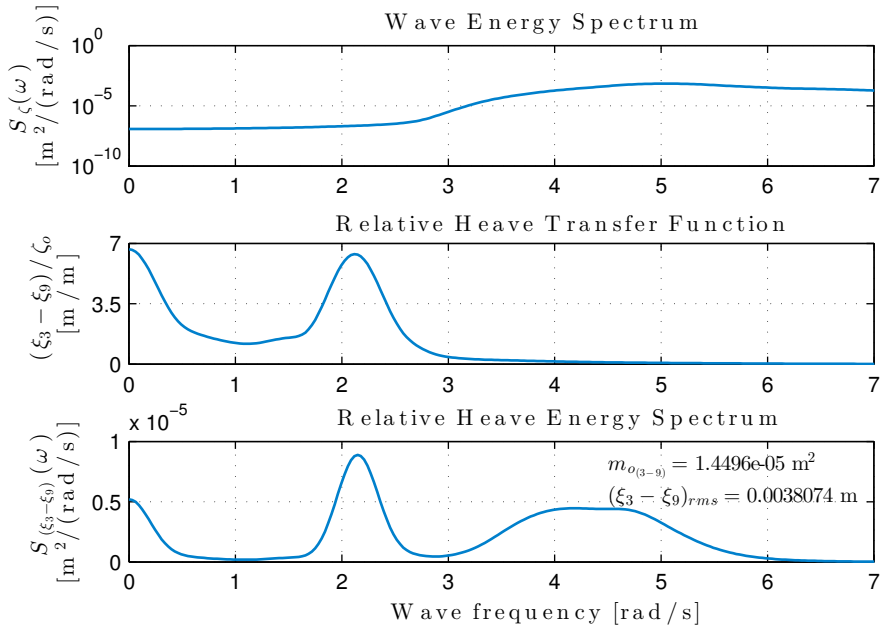

(a) Relative heave spectra for test T33

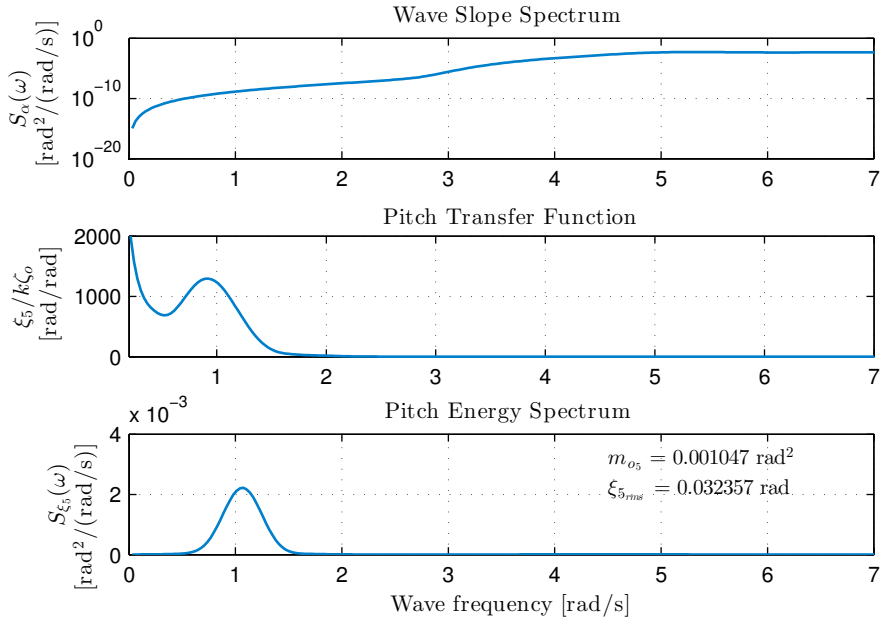

(b) Pitch spectra for test T33

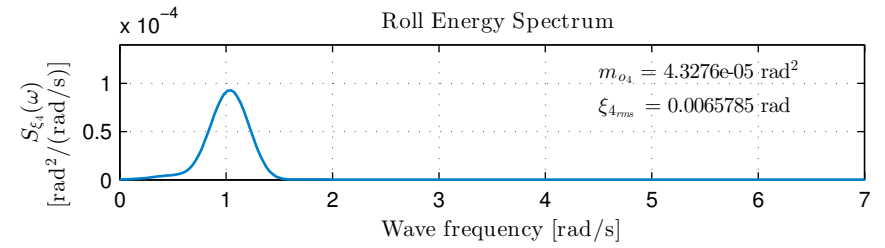

(c) Roll motion spectrum for test T33

Figure 7.5: Calculation of motion energy spectra for (a) relative heave (b) pitch and (c) roll for $H_s = 0.2$m, $T_p = 1.25$s and $B_{PTO} = 5000$ Ns/m

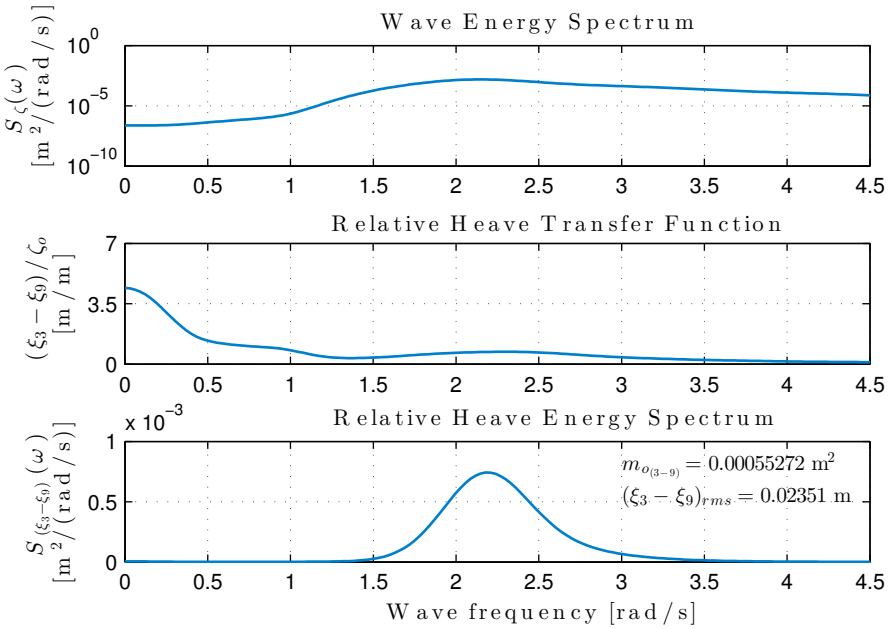

(a) Relative heave spectra for test T34

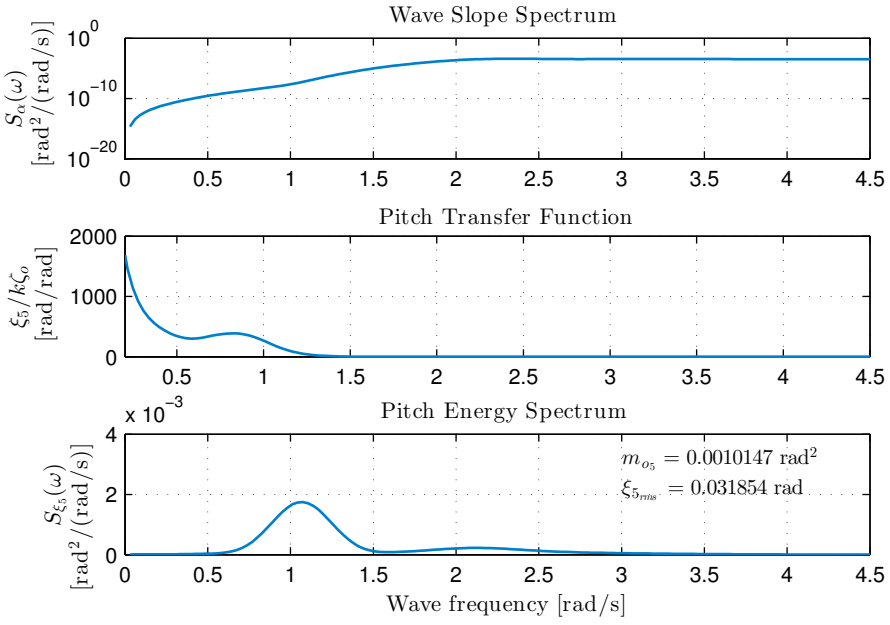

(b) Pitch spectra for test T34

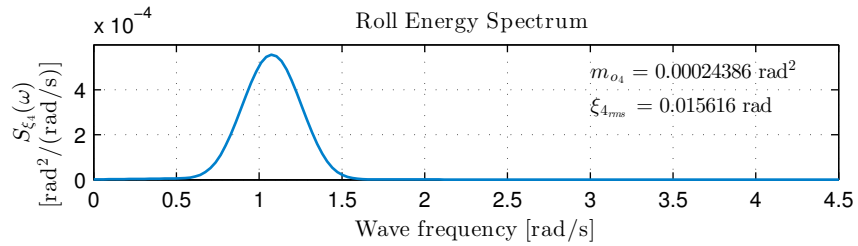

(c) Roll motion spectrum for test T34

Figure 7.6: Calculation of motion energy spectra for (a) relative heave (b) pitch and (c) roll for $H_s = 0.2$m, $T_p = 2.94$s and $B_{PTO} = 5000$ Ns/m

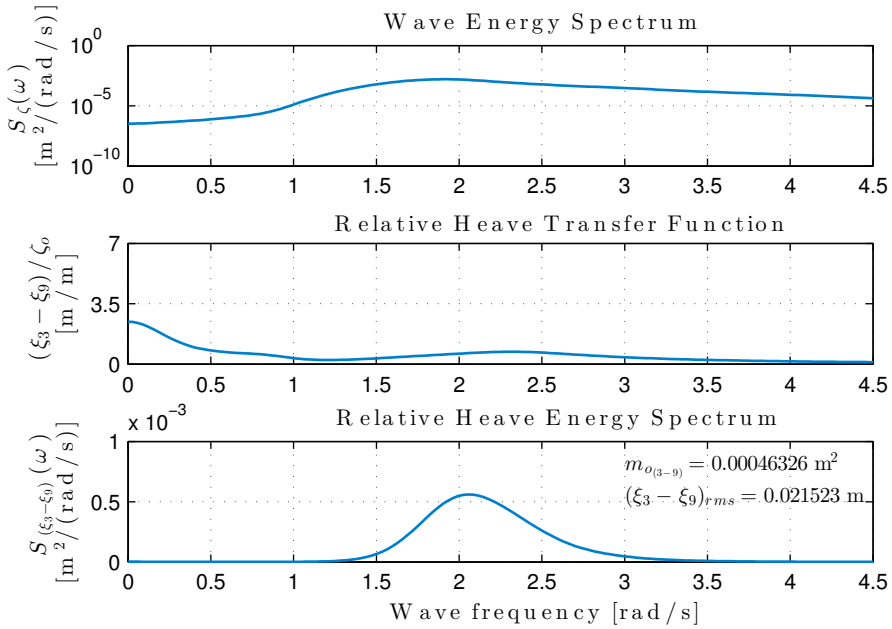

(a) Relative heave spectra for test T35

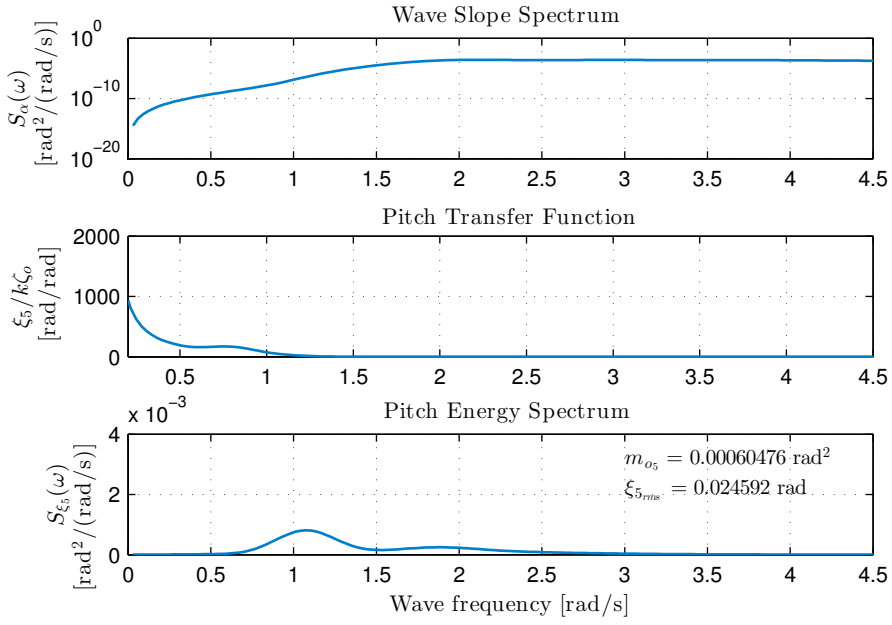

(b) Pitch spectra for test T35

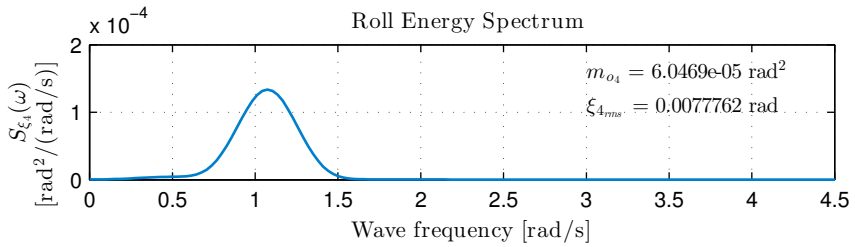

(c) Roll motion spectrum for test T35

Figure 7.7: Calculation of motion energy spectra for (a) relative heave (b) pitch and (c) roll for $H_s = 0.2$m, $T_p = 3.33$s and $B_{PTO} = 5000$ Ns/m

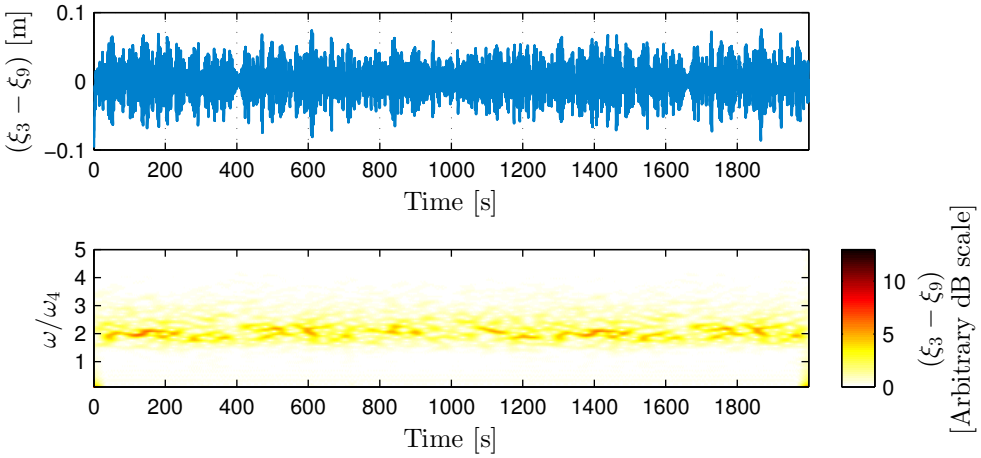

(a) Time-frequency analysis of relative heave motion for test T34

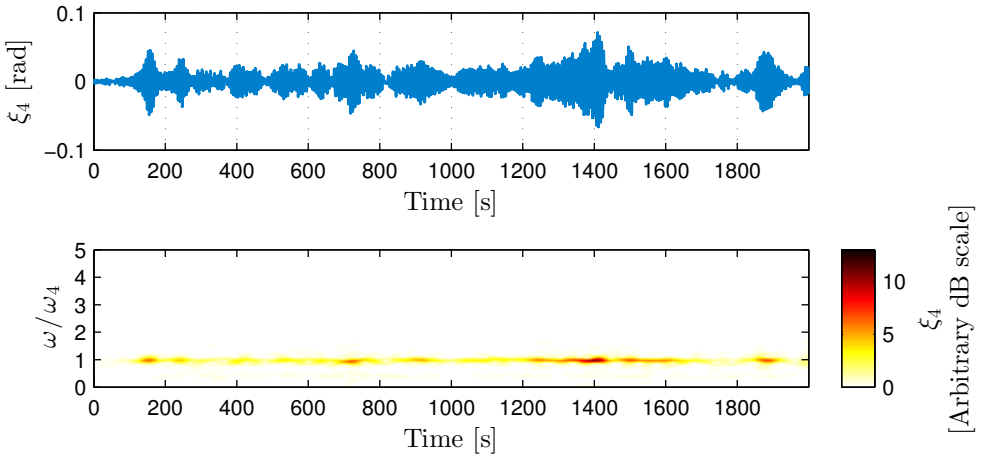

(b) Time-frequency analysis of roll motion for test T34

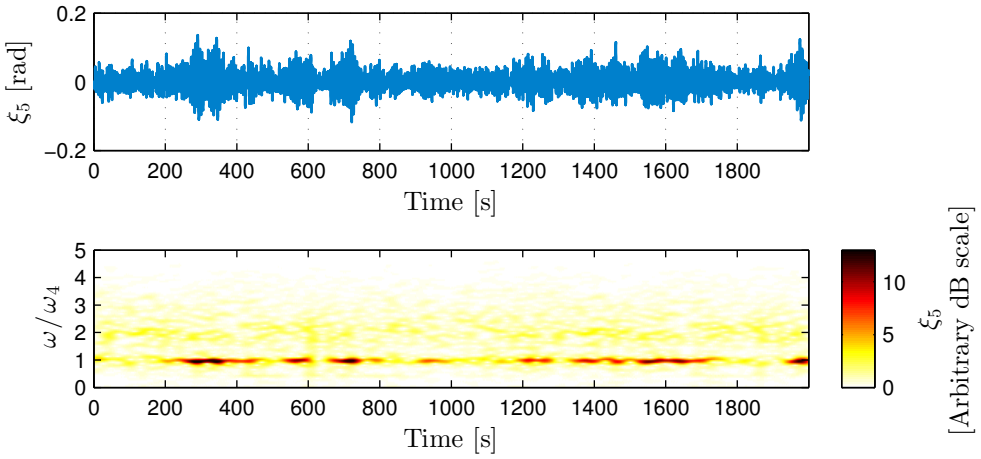

(c) Time-frequency analysis of pitch motion for test T34

Figure 7.8: Time frequency analysis of test T34 for (a) relative heave (b) roll and (c) pitch for $H_s = 0.2$m, $T_p = 2.94$s and $B_{PTO} = 5000$ Ns/m

Chapter 8

Conclusions

An investigation into the dynamic stability of the Wavebob wave energy converter has been carried out in this thesis. The main objective of the study has been to develop a numerical model which has the capabilities of simulating the large amplitude motions of the device in parametric resonance conditions in both regular and irregular longitudinal waves. To achieve this, a time domain fully coupled nonlinear model was further developed which is based on the assumption that the Froude-Krylov excitation forces and hydrostatic restoring forces are the main sources of nonlinearity in the fluid-structure interactions. A numerical benchmark study for the simulation of parametric resonance of the Wavebob has been implemented and validated against experimental results using the nonlinear model. The work carried out in this study has led to the following conclusions:

- The fully coupled nonlinear numerical model which was presented in Chapter 3 shows good capabilities in predicting the amplitudes of response of the Wavebob wave energy converter in regular waves. There was predominantly first order responses when the device was excited at wave excitation frequencies outside the zones of parametric resonance. This was evident in all degrees of freedom except for the roll mode, in which case there was almost zero response. There were some inconsistencies between the numerical model and the experimental results at lower wave frequencies due to the assumption of a linear mooring system and also due to the omission of structural and frictional damping in the model. However, the overall trend of the motion responses obtained from the numerical model showed excellent agreement with that from the experimental tests.

- The Wavebob is prone to parametric resonance in regular waves in conditions where the wave excitation frequency is twice the roll/pitch natural frequency. The nonlinear numerical model benchmark was implemented and validated against experimental results in parametric resonance conditions in regular waves for a range of different wave amplitudes. The results obtained in the relative heave, roll and pitch modes have shown good agreement with the records of the experiments. At parametric resonance, the model was able to predict both the onset and steady state response amplitude of the device, and in particular, the model was able to capture the nonlinear coupling between the heave, roll and pitch modes.

- The analysis of the results of the simulations in parametric resonance conditions reveal that parametric roll occurs once the wave amplitude exceeds a certain threshold. Under such conditions, the device becomes unstable in the roll mode, with the roll oscillations gradually increasing until a steady state amplitude of response is attained—the magnitude of which is determined by the level of nonlinear damping in the system. When parametric roll takes place, the roll mode oscillates at the roll natural frequency. Parametric pitch and heave also occur under such wave conditions. When parametric pitch takes place, the device initially oscillates at the wave excitation frequency, however, as the oscillations grow in amplitude, a shift in frequency takes place whereby the device has it's largest oscillations at the pitch natural frequency. Similar to the roll mode, the pitch also reaches a steady state response amplitude which is determined by the nonlinear damping in the system. There is a strong nonlinear coupling between the relative heave, roll and pitch modes in parametric resonance conditions. The relative heave motion is reduced as the roll and pitch oscillations grow in magnitude due to a nonlinear coupling between the modes. Some of the energy in the heave mode is transferred to the roll and pitch modes until a steady state heave response is attained. The relative heave response is predominantly at the wave excitation frequency, with some level of response also taking place at harmonics of the roll and pitch natural frequency.

- Due to the strong nonlinear coupling between the modes, a fully coupled nonlinear model is required to simulate parametric resonance of a two-body point absorber

wave energy converter. The assumption that the Froude-Krylov excitation force and the hydrostatic restoring forces are the main source of nonlinearity in the fluid-structure interaction—with the radiation-diffraction forces remaining linear—has shown to be sufficient to model parametric resonance. A fully linear model is not capable of simulating parametric roll in longitudinal waves, as in such a model, the roll mode is not externally excited and the surge, heave and pitch modes are uncoupled from the sway, roll and yaw modes.

- Limits of stability have been formulated for the roll and pitch modes for different PTO damping coefficients. The limits of stability show the appearance of unstable areas resembling the first Mathieu type unstable zone. The width of the unstable regions grow not only with wave amplitude but also with an increase in PTO damping coefficient. The device becomes more unstable in the roll and pitch modes as the level of PTO damping increases. The regions of instability in the roll mode tend to bend towards the right for higher wave excitation frequencies, which becomes more pronounced as the PTO damping coefficient is increased. This behaviour is due to nonlinear stiffening of the system which is more significant for higher waves.

- Simulations in irregular long crested waves revealed that there was a significant roll response at the roll natural frequency for all wave excitation frequencies, including excitation frequencies outside the main zones of parametric resonance, even though the roll mode is not directly excited in long crested waves. This is due to the fact that there will always be some level of parametric excitation at twice the roll natural frequency in irregular waves due to broadband excitation. At the tuning factor of 2, there are sudden bursts of roll motion due to parametric roll, however the large roll amplitudes are not sustained as they were in regular waves undergoing parametric resonance.

- The influence of initial conditions in the pitch degree of freedom was investigated in parametric resonance conditions. It was found that the pitch motion converges to a limit cycle regardless of whether the initial pitch angle starts from inside, or outside the limit cycle. This suggests that the device does not display hysteresis and there appears to be no metastable state.

8.1 Future work

From the conclusions drawn, it is apparent that there are several avenues that are open to further research. The following is a list of some of those possibilities:

- It would be of particular interest to implement a nonlinear mooring system into the numerical model. This would be of great value since the mooring can introduce significant nonlinear responses and possibly induce parametric resonance due to internal excitation.

- The numerical modelling of the PTO system could be improved to obtain a more realistic assessment of power absorption of the device. It would be useful to have the option of implementing different PTO systems such as a hydraulic PTO, linear generators etc. to see what the effect of each system has on the overall power output of the device.

- Numerical simulations of the device in short crested irregular seas to obtain a more accurate assessment of the device in real seas.

- Experimental free decay tests of the individual bodies (torus and FNT separated) in a wave tank could be performed in order to construct an improved model of the viscous drag.

- System identification techniques could be applied to the results from the numerical model in order to construct a lumped parameter nonlinear model which could be evaluated with various sea state forcing and compared with the simulated models.

Bibliography

[1] BP. BP energy outlook 2035. Retreived July 17, 2014 from http://www.bp.com/.

[2] International Energy Agency. Redrawing the energy climate map. World energy outlook special report. Technical report, 2013.

[3] European Commission. 2020 by 2020. Europe's climate change opportunity. Technical report, 2008.

[4] Eurostat. Energy, transport & environmental indicators. Retreived on July 21, 2014 from http://epp.eurostat.ec.europa.eu/portal/page/portal/eurostat/home/.

[5] BP. BP sustainability review 2013. Retreived on August 12, 2014 from http://www.bp.com/.

[6] WERATLAS European Wave Energy Atlas. Retreived on May 13, 2014 from http://www.macs.hw.ac.uk/∼denis/wave/weratlas.pdf.

[7] J.P. Kofoed, P. Frigaard, E. Friis-Madsen, and H.C. Sørensen. Prototype testing of the wave energy converter wave dragon. *Renewable Energy*, 31(2):181–189, 2006.

[8] A.H. Clément, P. McCullen, A. Falcão, A. Fiorentino, F. Gardner, K. Hammarlund, G. Lemonis, T. Lewis, K. Nielsen, S. Petroncini, M.T. Pontes, P. Schild, B.O. Sjöström, H.C. Sørensen, and T.W. Thorpe. Wave energy in Europe: current status and perspectives. *Renewable and Sustainable Energy Reviews*, 6:405–431, 2002.

[9] J.M. Leishman and G. Scobie. The development of wave power. A techno economic study. Technical Report East Kilbride, Scotland: National Engineering Laboratory, 1976.

[10] S.H. Salter. Wave power. *Nature*, 249:720–724, 1974.

[11] European Commission. The EU emissions trading system. Retreived on June 15, 2014 from http://www.bp.com/.

[12] WaveNet Thematic Network. Results from the work of the European Thematic Network on wave energy. Retreived on July 15, 2014 from http://cordis.europa.eu/documents/documentlibrary/66682851en6.pdf.

[13] Ocean Energy Systems. Implementing Agreement on Ocean Energy Systems. Annual Report 2012. Technical report.

[14] European Commission. Harnessing the power of the sea. Retreived on July, 18, 2014 from http://ec.europa.eu/.

[15] A Falcão. The shoreline OWC wave power plant at the Azores. In *Proceedings of the 4th European Wave Energy Conference*, Aalborg, Denmark, 2000.

[16] L. Margheritini, D. Vicinanza, and J.P. Kofoed. Hydraulic characteristics of sea wave slot cone generator pilot plant at Kvitsøy. In *Proceedings of the 7th European Wave and Tidal Energy Conference*, Porto, Portugal, 2007.

[17] B. Drew, A.P. Plummer, and M.N. Sahinkaya. A review of wave energy converter technology. Technical report, Department of Mechanical Engineering, University of Bath, 2009.

[18] A. Lewis, S. Estefen, J. Huckerby, W. Musial, T. Pontes, and J. Torres-Martinez. Ocean Energy. IPCC special report on renewable energy sources and climate change mitigation. Technical report, 2011.

[19] J. Falnes and K. Budal. Wave power conversion by point absorbers. *Norwegian Maritime Research*, 6(4), 1978.

[20] J. Falnes. Principles for capture of energy from ocean waves. Phase control and optimum oscillation. Technical report, Department of Physics, Norwegian University of Science and Technolgy, 1997.

[21] Wavebob Ltd. Internal report notes. Technical report, 2010.

[22] P. Lin and P.L-F. Liu. Free surface tracking methods and their applications to wave hydrodynamics. *Advances in Coastal and Ocean Engineering*, 5:213–240, 1999.

[23] E.B. Agamloh, A.K. Wallace, and A. von Jouanne. Application of fluidstructure interaction simulation of an ocean wave energy extraction device. *Renewable Energy*, 33(4):748–757, 2008.

[24] Y. Yu and Y. Li. A RANS simulation of the heave response of a two body floating point wave absorber. In *Proceedings of the 21st International Offshore and Polar Engineering Conference*, Maui, Hawaii, United States, 2011.

[25] P. Schmitt, S. Bourdier, D. Sarkar, E. Renzi, F. Dias, K. Doherty, T. Whittaker, and J. van't Hoff. Hydrodynamic loading on a bottom hinged oscillating wave surge converter. In *Proceedings of the 22nd International Offshore and Polar Engineering Conference*, Rhodes, Greece, 2012.

[26] P. Schmitt, T. Whittaker, D. Clabby, and K. Doherty. The opportunities and limitations of using CFD in the devlopment of wave energy converters. In *Proceddings of the International Conference of Marine & Offshore Renewable Energy*, London, UK, 2012.

[27] C.-H. Lee and J.N. Newman. Computation of wave effects using panel method. In *Numerical models in fluid-structure interaction.*, WIT Press. Preprint, Editor: S. Chakrabarti, WIT Press, Southampton, 2004. (Copyrighted by WIT Press.).

[28] B. Bosma, Z. Zhang, T.K.A. Brekken, H.T. Ozkan-Haller, C. McNatt, and S.C. Yim. Wave energy converter modelling in the frequency domain. A design guide. In *IEEE Energy Conversion Congress and Exposition*, pages 2099–2106, Raleigh, NC, USA, 2012.

[29] G. De Backer, M. Vantorre, C. Beels, J. De Rouck, and P. Frigaard. Power absorption by closely spaced point absorbers in constrained conditions. *IET Renewable Power Generation*, 4(6):579–591, 2010.

[30] J.C. Gilloteaux, G. Ducrozet, A. Babarit, and A.H. Clément. Non-linear model to simulate large amplitude motions: application to wave energy conversion. In *Proceedings of the 22nd International Workshop on Water Waves and Floating Bodies*, pages 97–100, Croatia, 2007.

[31] M. Guerinel, M. Alves, and A. Sarmento. Nonlinear modelling of the dynamics of a free floating body. In *Proceedings of the 9th European Wave and Tidal Energy Conference*, Southampton, UK, 2011.

[32] J. Hals, R. Taghipour, and T. Moan. Dynamics of a force compensated two body wave energy converter in heave with hydraulic power take off subject to phase control. In *Proceedings of the 7th European Wave and Tidal Energy Conference*, Porto, Portugal, 2007.

[33] J.C. Gilloteaux, G. Bacelli, and J. Ringwood. A nonlinear potential model to predict large-amplitudes motions: application to a multi-body wave energy converter. In *10th World Renewable Energy Congress - WRECX. WREC*, pages 934–940, Brighton, UK, 2008.

[34] A. Babarit, H. Mouslim, A.H. Clément, and P. Laporte-Weywada. On the numerical modelling of the nonlinear behaviour of a wave energy converter. In *Proceedings of the 28th International Conference on Offshore Mechanics and Arctic Engineering*, pages 1045–1053, 2009.

[35] Ø.Y. Rogne. *Numerical and experimental investigation of a hinged 5-body wave energy converter.* Ph.D. Thesis. Norweigian University of Science and Technolgy, 2014.

[36] W. Lin and D. Yue. Numerical simulations for large amplitude ship motions in the time domain. In *Proceddings of the 18th Symposium on Naval Hydrodynamics*, USA, 1991.

[37] J.G. Bretl. *A time domain model for wave induced motions coupled to energy extraction.* Ph.D. Thesis. University of Michigan, 2009.

[38] W.E. Cummins. The impulse response function and ship motions. *Schiffstechnik*, 9:101–109, 1962.

[39] R. Taghipour, T. Perez, and T. Moan. Hybrid frequency time domain models for dynamic response analysis of marine structures. *Ocean Engineering*, 35(7):685–705, 2008.

[40] J.C. Gilloteaux. *Mouvements de grande amplitude d'un corps flottant en fluide parfait. Application a la recuperation de l'energie des vagues.* Ph.D. Thesis. École Centrale de Nantes, 2007.

[41] A. Merigaud, J.C. Gilloteaux, and J. Ringwood. A nonlinear extension for linear boundary element methods in wave energy device modelling. In *Proceedings of the ASME 31st International Conference on Ocean, Offshore and Arctic Engineering*, Rio de Janeiro, Brazil, 2012.

[42] S. Rao. *Mechanical vibrations.* Department of Civil Engineering, Aalborg University. (DCE Lecture Notes; No. 24), 2nd edition, 1990.

[43] R. Rand. Lecture notes on nonlinear vibrations. Version 52. Technical report, Department of Theoretical and Applied Mechanics, 2003.

[44] Y.S. Shin, V.L. Belenky, J.R. Paulling, K.M. Weems, and W.M. Lin. Criteria for parametric roll of large containerships in longitudinal seas. *SNAME Transactions*, 112, 2004.

[45] N.A. Perez and C.F. Sanguinetti. Scale model tests of a fishing vessel in roll motion parametric resonance. *Síntesis Tecnológica*, 3(1):33–37, 2006.

[46] W.N. France, M. Levadou, T.W. Treakle, J.R. Paulling, R.K. Mickel, and C. Moore. An investigation of head-sea parametric rolling and its influence on container lashing systems. Technical report, SNAME Annual Meeting. Sname Marine Technology, 2001.

[47] N. Umeda, H. Hashimoto, D. Vassalos, S. Urano, and K. Okou. Nonlinear dynamics on parametric roll resonance with realistic numerical modelling. In *Proceedings of the 8th International Conference on the Stability of Ships and Ocean Vehicles*, Madrid, Spain, 2003.

[48] C.E. Uzunoğlu. *Numerical and experimental study of parametric rolling of a container ship in waves.* Master's Thesis. Universidade Técnica de Lisboa, 2011.

[49] H.A. Haslum and O.M. Faltinsen. Alternative shape of spar platforms for use in hostile areas. *Offshore Technolgy Conference, Houston, USA*, 1999.

[50] Y.P. Hong, D.Y. Lee, Y.H. Choi, S.K. Hong, and S.E. Kim. An experimental study on the extreme motion responses of a spar platform in the heave resonant waves. In *Proceedings of the 15th International Offshore and Polar Engineering Conference*, Seoul, Korea, 2005.

[51] J.B. Rho and H.S. Choi. Heave and pitch motions of a spar platform with damping plate. In *Proceedings of the 12th International Offshore and Polar Engineering Conference*, Kitakyushu, Japan, 2002.

[52] M.A.S. Neves, S.H. Sphaier, B.M. Mattoso, C.A. Rodríguez, A.L. Santos, V.L. Vileti, and F.G.S. Torres. On the occurrence of Mathieu instabilities of vertical cylinders. In *Proceddings of the 27th International Conference on Offshore Mechanics and Arctic Engineering*, Estoril, Portugal, 2008.

[53] Y. Liu, H. Yan, and T.W. Yung. Nonlinear resonant response of deep draft platforms in surface waves. In *Proceddings of the 29th International Conference on Ocean, Offshore and Arctic Engineering*, Shanghai, China, 2010.

[54] B.B. Li, J.P Ou, and B. Teng. Numerical investigation of damping effects on coupled heave and pitch motion of an innovative deep draft multi spar. *Journal of Marine Science and Technology*, 19(2):231–244, 2011.

[55] J.N. Newman. *Marine Hydrodynamics.* The MIT Press, 1977.

[56] J. Falnes. *Ocean Waves and Oscillating Systems.* Cambridge University Press, 2002.

[57] J. Cruz. *Ocean Wave Energy. Current Status and Future Perspectives.* Springer, 2008.

[58] T.L. Anderson, P. Frigaard, and P. Bak. *Lecture Notes for the Course in Water Wave Mechanics.* Addison Wesley, 2011.

[59] R.G. Dean and R.A. Dalrymple. *Water Wave Mechanics for Engineers and Scientists*. World Scientific, 1991.

[60] T.F. Ogilvie. Recent progress towards the understanding and prediction of ship motions. In *Proceddings of the the 6th Symposium on Naval Hydrodynamics*, pages 3–128, Washington D.C.

[61] J. Fitzgerald and L. Bergdahl. Including moorings in the assessment of a generic offshore wave energy converter: A frequency domain approach. *Marine Structures*, 21(1):23–46, 2008.

[62] R. Rainey. The dynamics of tethered platforms. In *Meeting of the Royal Institute of Naval Architects*, pages 59–80.

[63] T.I. Fossen. *Guidance and Control of Ocean vehicles*. Wiley and Sons, 1994.

[64] Territoires d'Innovation. Retreived on May 9, 2014 from http://www.mre-paysdelaloire.com/presentation-2/excellence-in-rd-3/.

[65] S.A. Mavrakos and I.K. Chatjigeorgiou. Second-order hydrodynamic effects on an arrangement of two concentric truncated vertical cylinders. *Marine Structures*, 22(3):545–575, 2009.

[66] J.N. Newman. Progress in wave load computations on offshore structures. In *Proceddings of the 23rd International Conference on Offshore Mechanics and Arctic Engineering*, Canada, 2004.

[67] C.A. Rodríguez and M.A.S. Neves. Nonlinar instabilities of spar platforms in waves. In *Proceddings of the 31st International Conference on Ocean and Arctic Engineering*, Rio de Janeiro, Brazil, 2012.

[68] G. Bulian, A. Francescutto, and C. Lugni. On the nonlinear modelling of parametric rolling in regular and irregular waves. *Journal of International Shipbuilding Progress*, 51(2-3):173–203, 2004.

[69] Y. Goda. *Random Seas and Design of Maritime Structures*. World Scientific Publishing Company Incorporated, 2010.

[70] K. Hasselmann, T.P. Barnett, E. Bouws, H. Carlson, D.E. Cartwright, K. Enke, J.A. Ewing, H. Gienapp, D.E. Hasselmann, P. Kruseman, A. Meerburg, P. Müller, D.J. Olbers, K. Richter, W. Sell, and H. Walden. Measurements of wind-wave growth and swell decay during the Joint North Sea Wave Project (JONSWAP). Technical report, Herausgegeben vom Deutschen Hydrographischen Institut, 1973.

[71] R.A. Adams. *Calculus. A Complete Course.* Addison-Wesley, 2006.

Appendix A

WAMIT output

A.1 Added mass coefficients

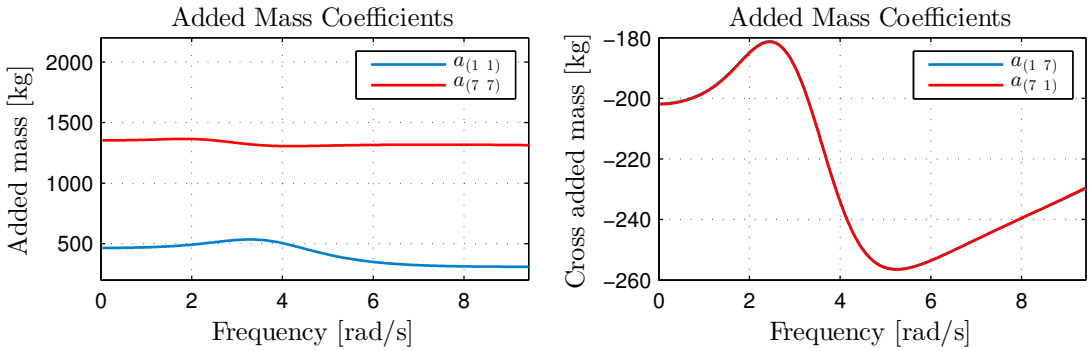

Figure A.1: Surge added mass for (a) torus & FNT (b) interactions of torus & FNT

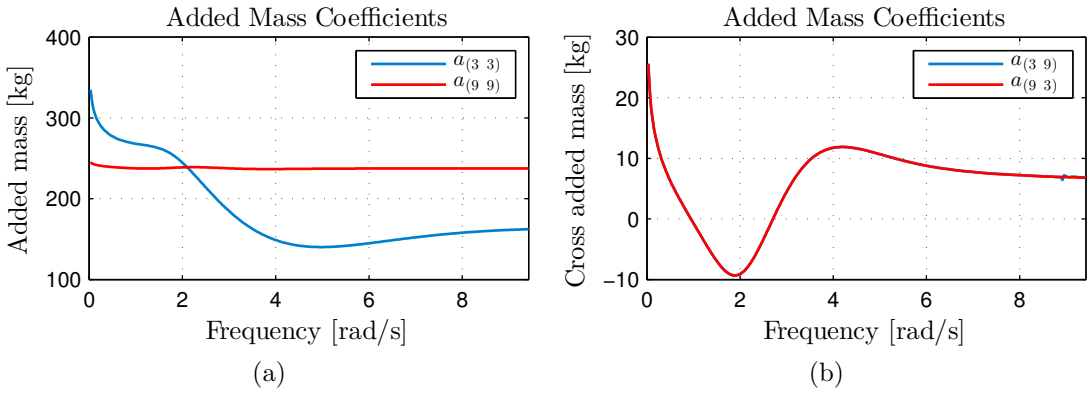

Figure A.2: Heave added mass for (a) torus & FNT (b) interactions of torus & FNT

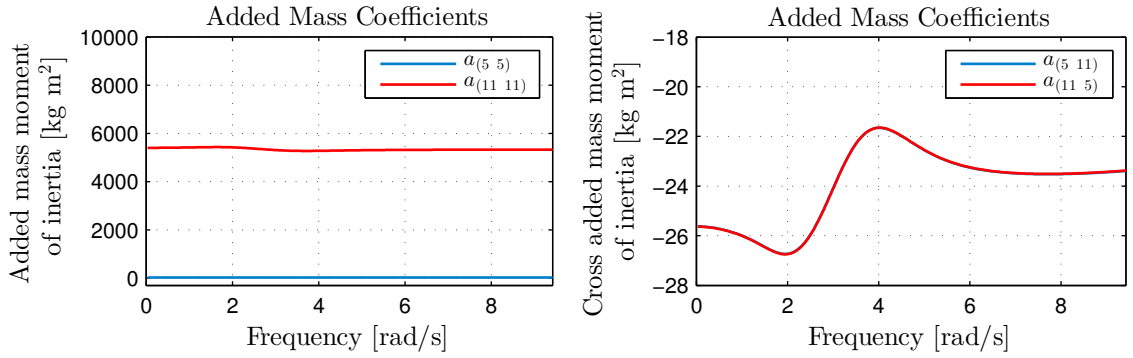

Figure A.3: Pitch added mass for (a) torus & FNT (b) interactions of torus & FNT

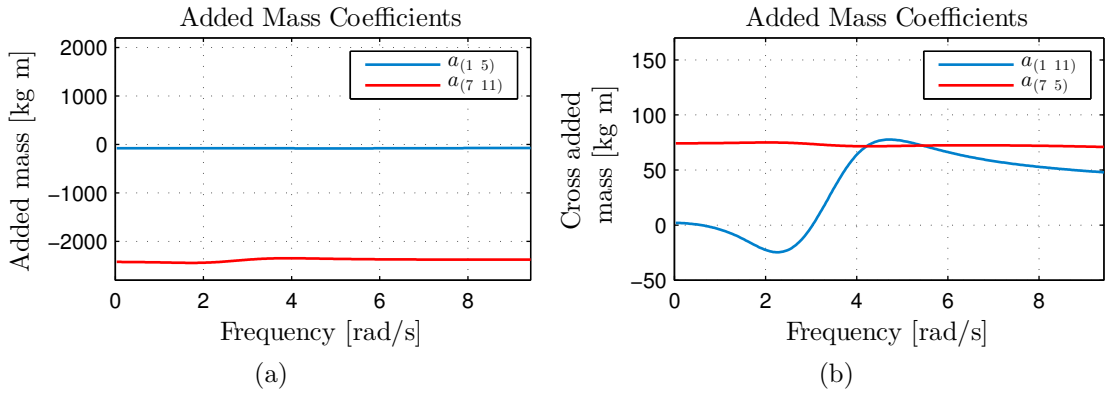

Figure A.4: Surge to pitch added mass interaction for (a) torus & FNT (b) interactions of torus & FNT

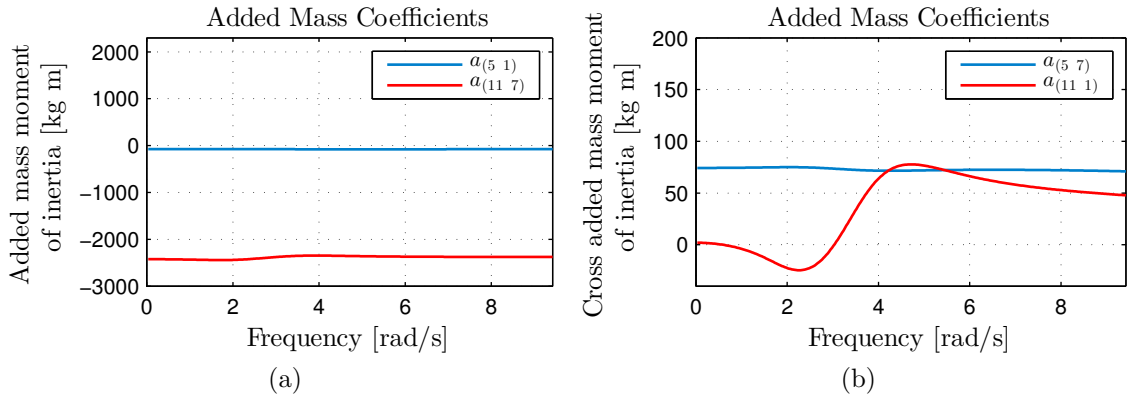

Figure A.5: Pitch to surge added mass interaction for (a) torus & FNT (b) interactions of torus & FNT

A.2 Radiation damping coefficients

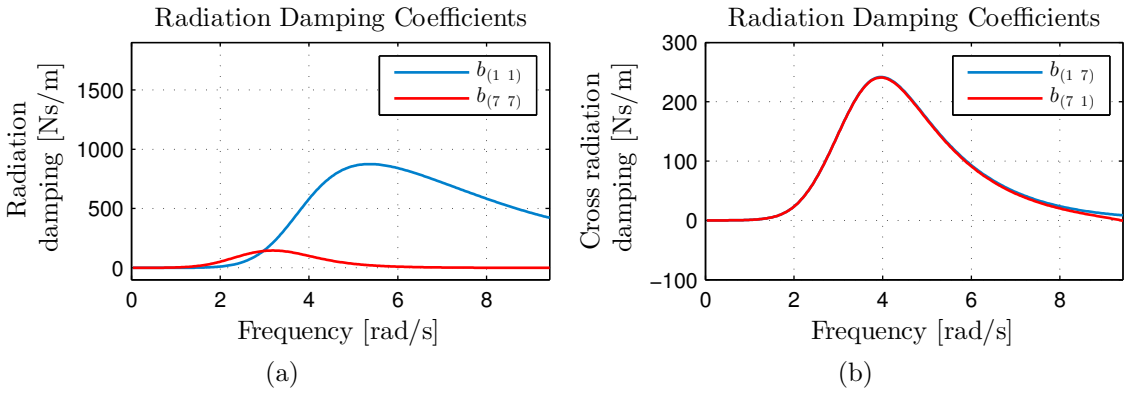

Figure A.6: Surge damping for (a) torus & FNT (b) interactions of torus & FNT

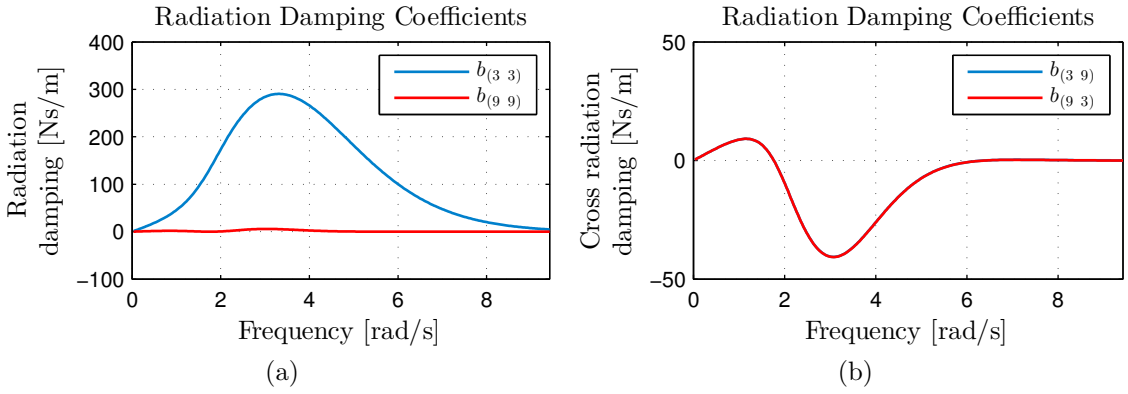

Figure A.7: Heave damping for (a) torus & FNT (b) interactions of torus & FNT

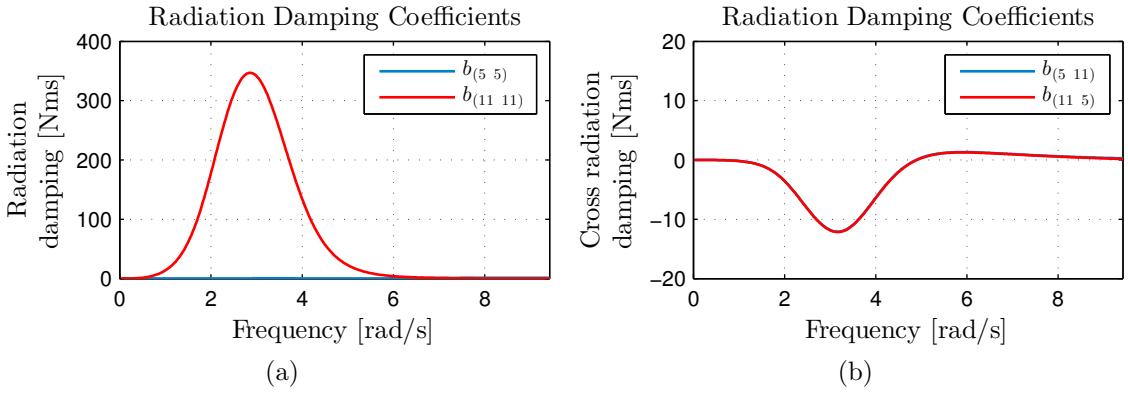

Figure A.8: Pitch damping for (a) torus & FNT (b) interactions of torus & FNT

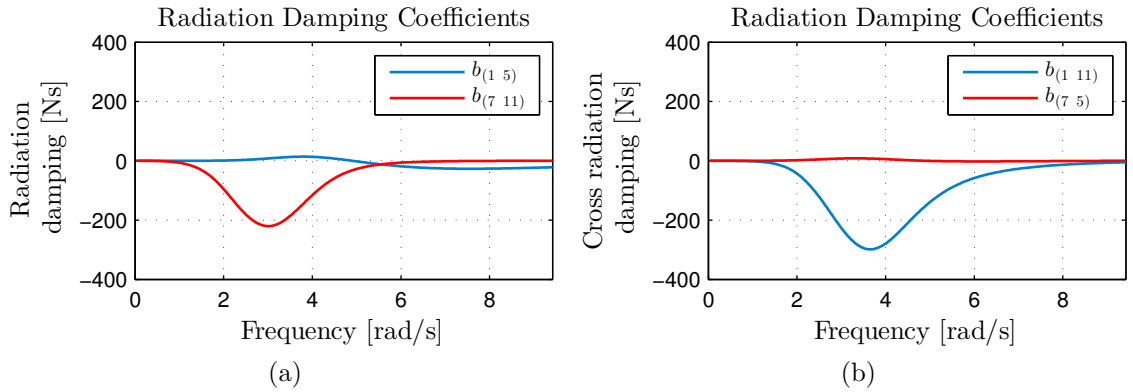

Figure A.9: Surge to pitch damping interaction for (a) torus & FNT (b) interactions of torus & FNT

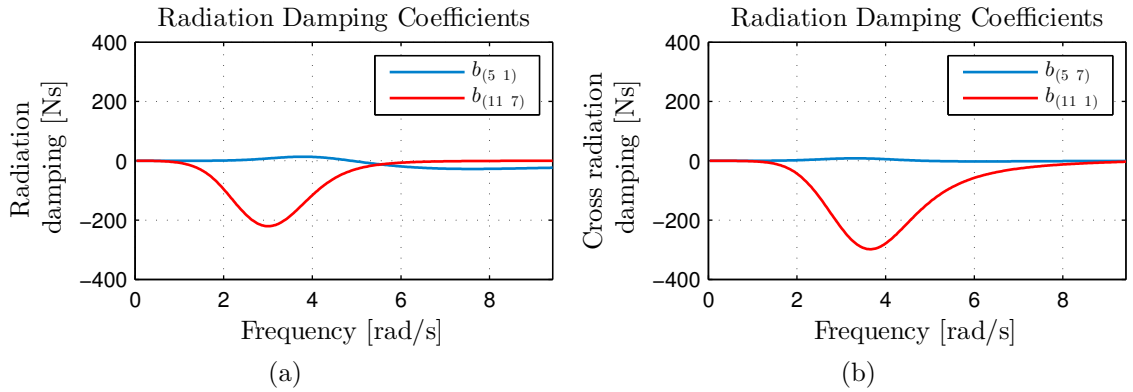

Figure A.10: Pitch to surge damping interaction for (a) torus & FNT (b) interactions of torus & FNT

A.3 Radiation damping impulse response functions

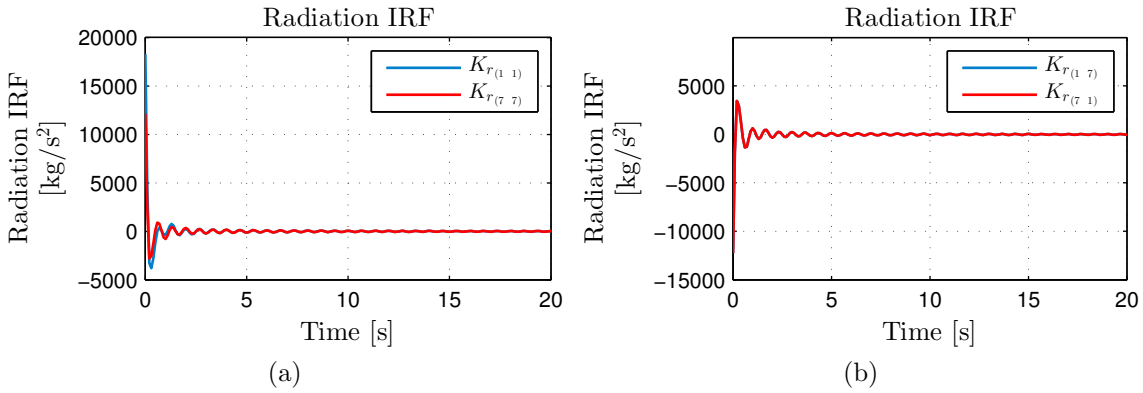

Figure A.11: (a) Surge radiation IRF for (a) torus & FNT (b) interactions of torus & FNT

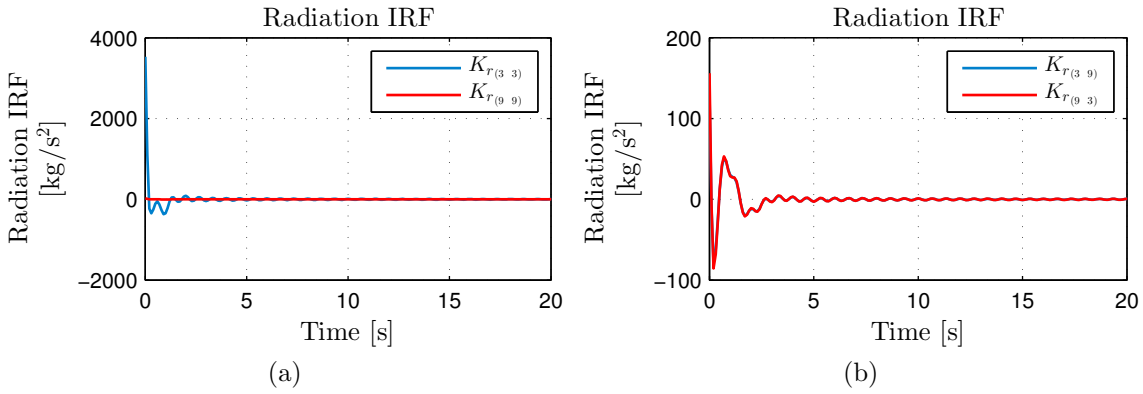

Figure A.12: Heave radiation IRF for (a) torus & FNT (b) interactions of torus & FNT

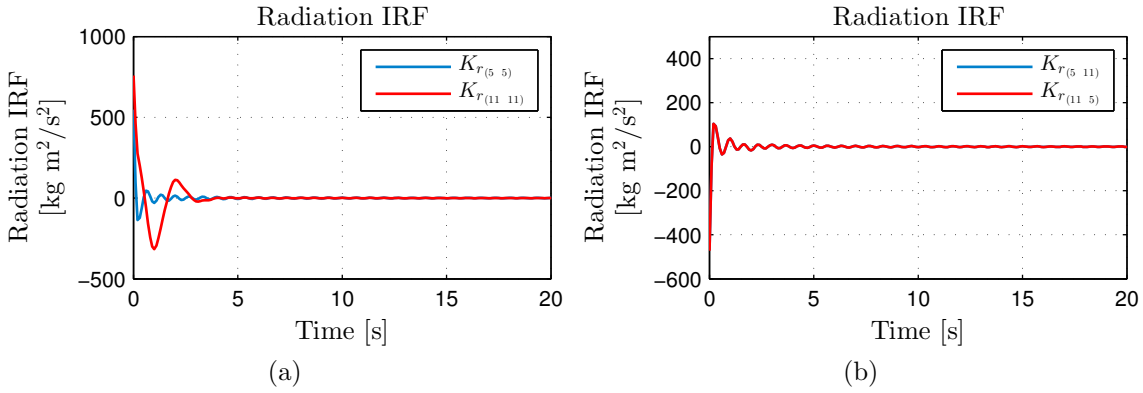

Figure A.13: (a) Pitch radiation IRF for (a) torus & FNT (b) interactions of torus & FNT

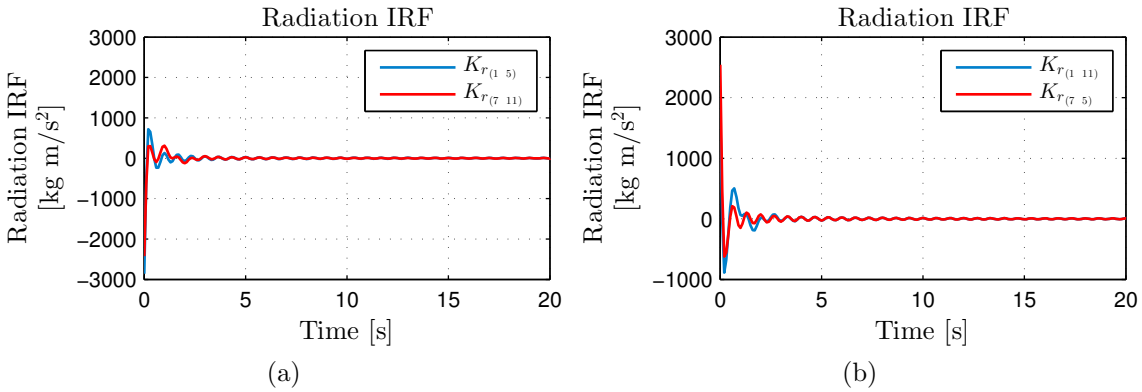

Figure A.14: Surge to pitch radiation IRF interaction for (a) torus & FNT (b) interactions of torus & FNT

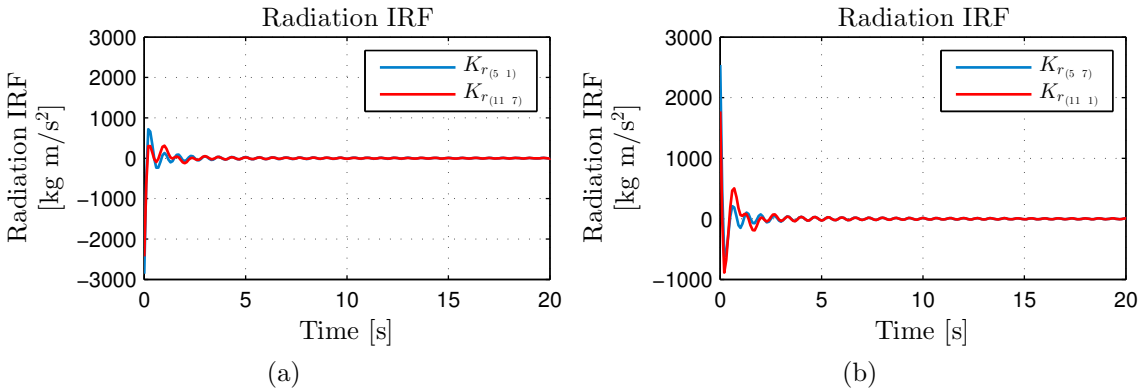

Figure A.15: Pitch to surge radiation IRF interaction for (a) torus & FNT (b) interactions of torus & FNT

A.4 Diffraction coefficients & impulse response functions

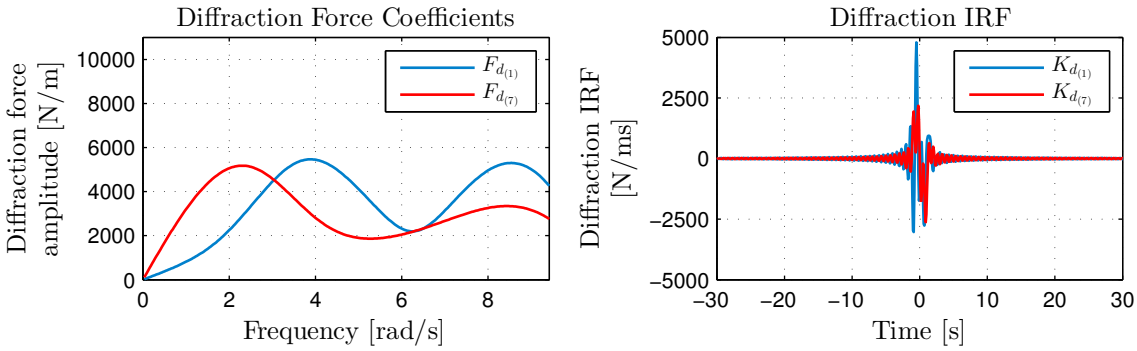

Figure A.16: (a) Surge diffraction coefficients (b) surge diffraction IRF of torus & FNT

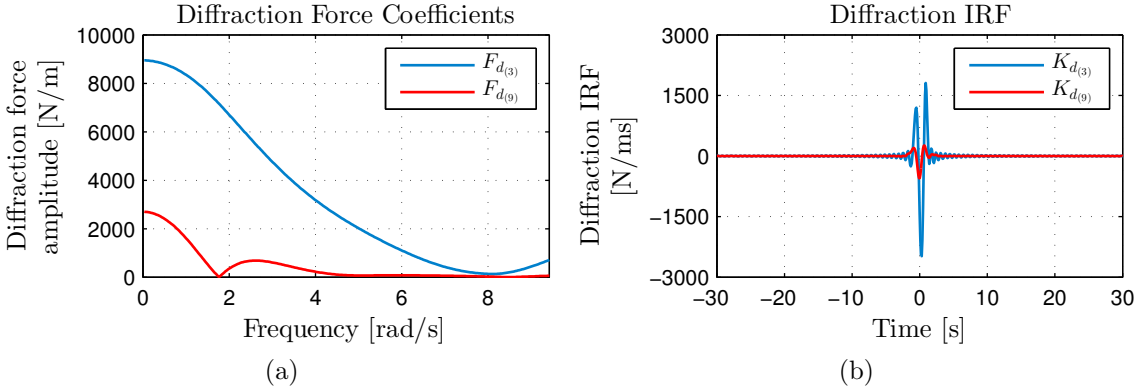

Figure A.17: (a) Heave diffraction coefficients (b) heave diffraction IRF of torus & FNT

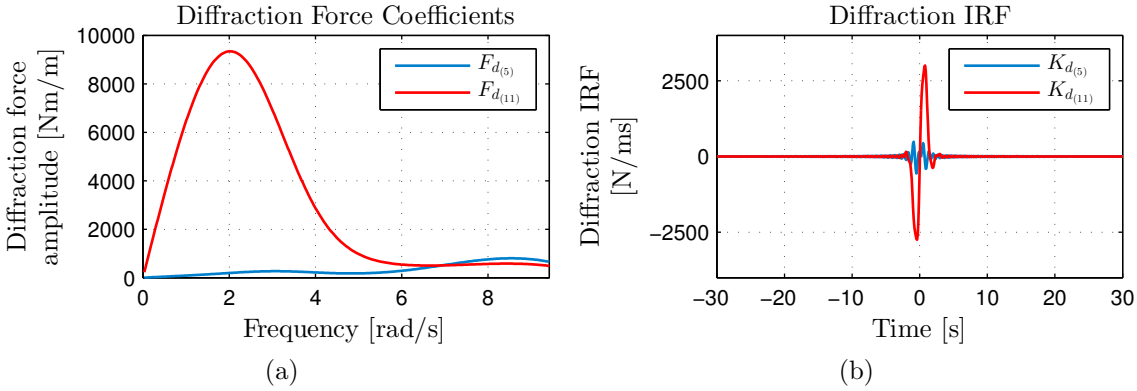

Figure A.18: (a) Pitch diffraction coefficients (b) pitch diffraction IRF of torus & FNT

Appendix B

Convolution

The concept of convolution can be explained by considering a linear system with input $x(t)$, and response $y(t)$ such that

$$x(t) \rightarrow \boxed{\text{Linear System}} \rightarrow y(t) \tag{B.1}$$

Let us assume the following properties of the system:

Linearity

A linear system has the property that its response to the sum of two inputs is the sum of the responses to each input separately. If $x_1 \rightarrow y(t)$ and $x_2(t) \rightarrow y_2(t)$, then

$$x_1(t) + x_2(t) \rightarrow y_1(t) + y_2(t) \tag{B.2}$$

This property is called superposition. This property extends to any number of inputs. Superposition also implies that scaling the input $x(t)$ by a constant a, scales the output as well

$$x(t) \rightarrow y(t) \Leftrightarrow ax(t) \rightarrow ay(t) \tag{B.3}$$

This property is called scaling. These two properties can be combined such that

$$a_1x_1(t) + a_2x_2(t) \rightarrow a_1y_1(t) + a_2y_2(t) \tag{B.4}$$

Time-invariance

A time-invariant system has the property that delaying the input signal by any constant τ delays the output by the same amount, i.e.,

$$x(t) \rightarrow y(t) \Leftrightarrow x(t-\tau) \rightarrow y(t-\tau) \tag{B.5}$$

If we consider the Dirac delta function $\delta(t)$ as input to the system, then the system's response is $h(t)$, i.e.,

$$\delta(t) \rightarrow h(t) \tag{B.6}$$

since $\mathcal{F}[\delta(t)] = 1$, i.e., all frequencies are equally present in the Dirac delta impulse, the system's response $h(t)$ is called the impulse response of the system and characterises transfer properties of the system in the time domain.
Due to time-invariance of the system

$$\delta(t-\tau) \rightarrow h(t-\tau) \tag{B.7}$$

Thus, some general input signal $x(t)$ can be represented using the Dirac delta function as

$$x(t) = \int_0^t x(\tau)\delta(t-\tau)d\tau \tag{B.8}$$

Eqn. B.8 means that the general signal $x(t)$ is an integral linear combination of the Dirac delta impulse $\delta(t-\tau)$. Eqn. B.8 and the linearity of the system imply, that the response to the input signal $x(t)$ is the same integral combination of the impulse responses $h(t-\tau)$

$$y(t) = \int_0^t x(\tau)h(t-\tau)d\tau \tag{B.9}$$

Eqn. B.9 states that once we know the impulse response of a system, we can compute the output of the system for an arbitrary input using the convolution. Eqn. B.9 can also be denoted as

$$y(t) = x(t) * h(t) \tag{B.10}$$

The steps implicitly involved in computing the convolution integral may be demonstrated graphically as shown in Figs. B.1 - B.5. The system input is shown in Fig. B.1(a) and the system impulse response function is shown in Fig. B.1(b). Both the input and the mirrored impulse response function are then expressed in terms of the new variable τ as shown in Figs. B.2(a) and (b) respectively. The mirrored impulse response function is then translated to time t_1 as shown in Fig. B.3(a) while the product of the input and translated impulse response is illustrated in Fig. B.3(b). Note, the area under the graph is shown as shaded in the figure, which is the value of the convolution at t_1. This step is then repeated for time t_2 as shown in Fig. B.4. The total convolution is then given in Fig. B.5 for all values of t.

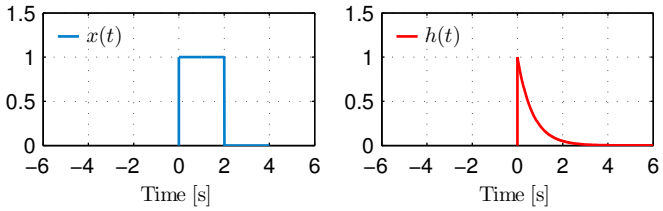

Figure B.1: (a) System input $x(t)$ (b) system impulse response $h(t)$

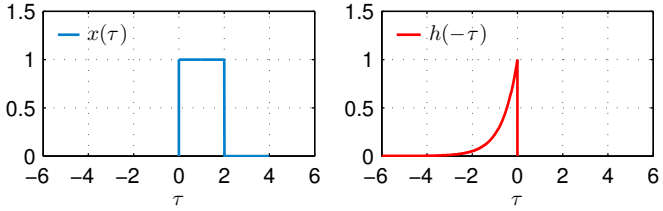

Figure B.2: (a) $x(\tau)$, the system input in terms of τ (b) $h(-\tau)$, the mirrored impulse response in terms of τ

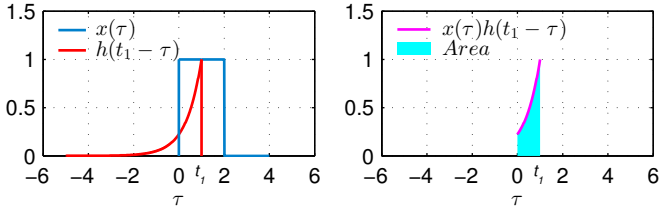

Figure B.3: (a) $x(\tau)$ and $h(t_1 - \tau)$ at time t_1 (b) product of $x(\tau)h(t_1 - \tau)$. Area under graph is shown as shaded

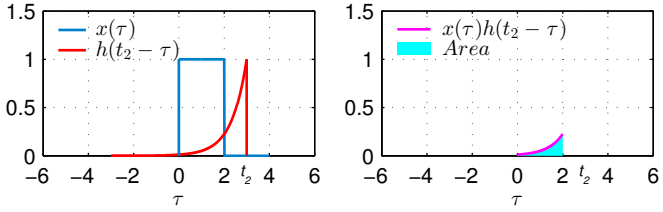

Figure B.4: (a) $x(\tau)$ and $h(t_2 - \tau)$ at time t_2 (b) product of $x(\tau)h(t_2 - \tau)$. Area under graph is shown as shaded

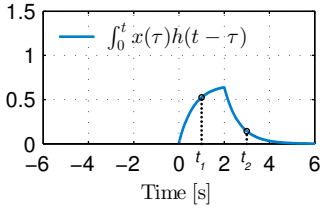

Figure B.5: $y(t)$, the system response

Appendix C

Linear interpolation

Linear interpolation is a method of curve fitting using linear polynomials. The method calculates the values at positions between data points, where the points are simply joined by straight line segments. From Fig. C.1, if the two known points are given by the coordinates (x_0, y_0) and (x_1, y_1), the linear interpolant is the straight line between these points.

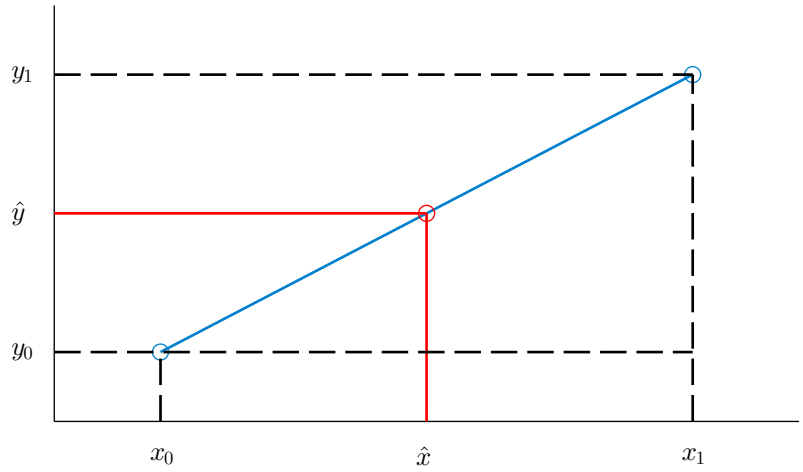

Figure C.1: Given two points (x_0, y_0) and (x_1, y_1), the blue line is the linear interpolant between the two points. The point $f(\hat{x}) = \hat{y}$ may be found by linear interpolation

For a value $\hat{x}$ in the interval (x_0, x_1), the value $f(\hat{x}) = \hat{y}$ along the straight line is found from the method of similar triangles in Fig. C.1 as

$$\frac{\hat{y} - y_0}{\hat{x} - x_0} = \frac{y_1 - y_0}{x_1 - x_0} \tag{C.1}$$

$$\hat{y} = y_0 + \frac{y_1 - y_0}{x_1 - x_0}(\hat{x} - x_0) \tag{C.2}$$

Appendix D

Trapezoidal integration

Trapezoidal integration is used in the current work to approximate the integral

$$\int_a^b f(x)dx \tag{D.1}$$

The explanation for the method has been taken from the work of Adams [71]. Assume that $f(x)$ is continuous on $[a, b]$ and subdivide $[a, b]$ into n sub-intervals of equal length $h = (b - a)/n$ using $n + 1$ points

$$x_0 = a, \quad x_1 = a + h, \quad x_2 = a + 2h, \quad \ldots, \quad x_n = a + nh = b.$$

Assume that the value of $f(x)$ at each of these points is known such that

$$y_0 = f(x_0), \quad y_1 = f(x_1), \quad y_2 = f(x_2), \quad \ldots, \quad y_n = f(x_n).$$

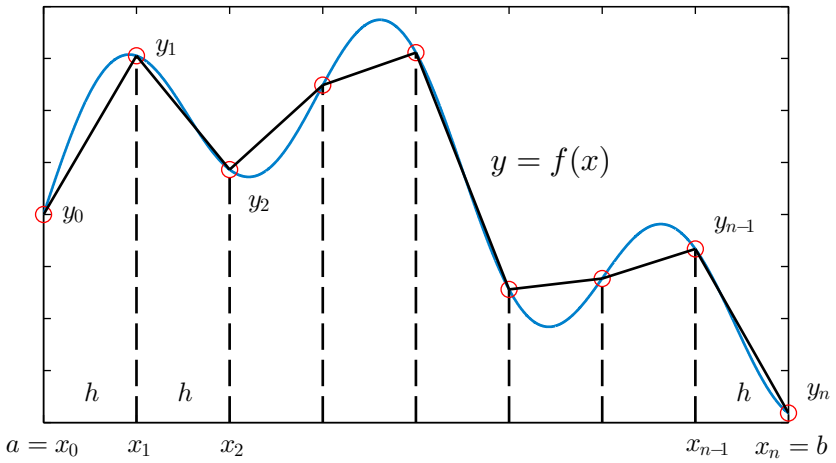

Figure D.1: The area under $y = f(x)$ is approximated by the sum of the areas of n trapezoids

The Trapezoid Rule approximates $\int_a^b f(x)dx$ by using straight line segments between the points (x_{j-1}, y_{j-1}) and (x_j, y_j), $(1 \leq j \leq n)$, to approximate the graph of f, as shown in Fig. D.1, and summing the areas of the resulting n trapezoids. The area of the first trapezoid is h times the average of the parallel sides. This trapezoidal area is used to approximate the integral of f over the first sub-interval $[x_0, x_1]$

$$\int_{x_0}^{x_1} f(x)dx \approx h\frac{y_0 + y_1}{2} \tag{D.2}$$

Thus, the approximate integral of f over any sub-interval is given by

$$\int_{x_{j-1}}^{x_j} f(x)dx \approx h\frac{y_{j-1} + y_j}{2}, \qquad (1 \leq j \leq n) \tag{D.3}$$

The integral can therefore be approximated by the sum of these trapezoidal areas

$$\int_a^b f(x)dx \approx h(\frac{1}{2}y_0 + y_1 + y_2 + y_3 + \ldots + y_{n-1} + \frac{1}{2}y_n) \tag{D.4}$$

which can be also written as

$$\int_a^b f(x)dx \approx \frac{h}{2}\left[f(x_0) + 2\sum_{j=1}^{n-1} f(x_0 + jh) + f(x_n)\right] \tag{D.5}$$

Appendix E

Runge-Kutta fourth order method

The Runge-Kutta fourth order method is a numerical technique used to solve ordinary differential equations. The formula for the fourth order Runge-Kutta method is given below. Consider the problem

$$\begin{aligned} \frac{dy}{dt} &= f(t, y) \\ y(t_o) &= y_o \end{aligned} \tag{E.1}$$

where y is an unknown function of time t which we would like to approximate. dy/dt is the rate at which y changes with respect to time, and it is a function of both t and y. The initial conditions for this example state that the value of y at the initial time t_o is y_o. Defining h to be the step size and $t_i = t_o + ih$, the Runge-Kutta fourth order method can then be written as

$$y_{i+1} = y_i + \frac{h}{6}(k_1 + 2k_2 + 2k_3 + k_4) \tag{E.2}$$

where,

$$\begin{aligned} k_1 &= f(t_i, y_i) \\ k_2 &= f(t_i + \frac{h}{2}, y_i + \frac{1}{2}k_1 h) \\ k_3 &= f(t_i + \frac{h}{2}, y_i + \frac{1}{2}k_2 h) \\ k_4 &= f(t_i + h, y_i + k_3 h) \end{aligned} \tag{E.3}$$

- k_1 is the increment based on the slope at the beginning of the interval, using y;
- k_2 is the increment based on the slope at the midpoint of the interval, using $y+\frac{1}{2}k_1h$;
- k_3 is the increment based on the slope at the midpoint of the interval, using $y+\frac{1}{2}k_2h$;
- k_4 is the increment based on the slope at the end of the interval, using $y + k_3h$.

Appendix F

CD-ROM—FORTRAN code for nonlinear numerical model

The following is the documentation for the list of FORTRAN files on the attached CD-ROM:

Diffraction.f90 File Reference

File Subroutines:

- subroutine KexWAMIT
- subroutine DiffIni
- subroutine ETAxt
- subroutine DiffractionForce

Drag_forces.f90 File Reference

File Subroutines:

- subroutine Drag_forces

force.f90 File Reference

File Subroutines:

- subroutine forces

FroudeKrylov.f90 File Reference

File Subroutines:

- subroutine FroudeKrylov
- subroutine KHydro
- subroutine hydrostatic_Lin

IncidentField.f90 File Reference

File Subroutines:

- subroutine IncidentFieldINIT
- subroutine ETA
- subroutine Pincident
- subroutine Airy
- subroutine Bretschneider
- subroutine Jonswap
- subroutine FreeSurfAnim

Inputdata.f90 File Reference

File Subroutines:

- subroutine INPUTDATA

Intersection.f90 File Reference

File Subroutines:

- subroutine Intersection

IntersectionTools.f90 File Reference

File Subroutines:

- subroutine Selection
- subroutine Rearrangement
- subroutine ParametricFrame

- subroutine InterPoints
- subroutine Intersect2DU
- subroutine Intersect2DV
- subroutine Intersect2D
- subroutine MeshWithFSH
- subroutine PanelareaSimple
- subroutine GRIDSURFIMM
- subroutine PanelareaSimple
- subroutine Tribulle_Vcroiss
- subroutine Tribulle_Ucroiss
- subroutine Tribulle_Vdecroiss
- subroutine Tribulle_Udecroiss
- subroutine AireFacette

main.f90 File Reference

File Subroutines:

- program FK_NUIM

Mooring.f90 File Reference

File Subroutines:

- subroutine MooringForce
- subroutine MooringShow

MoorLin.f90 File Reference

File Subroutines:

- subroutine MooringStiffness
- subroutine MoorLin_anim

Motions.f90 File Reference

File Subroutines:

- subroutine MotionsQuatern
- subroutine MoorLin_anim

Output.f90 File Reference

File Subroutines:

- subroutine Output

PositionUpdating.f90 File Reference

File Subroutines:

- subroutine meshupdate

PTO.f90 File Reference

File Subroutines:

- subroutine PTO_ini
- subroutine PTO_Force

transfinite.f90 File Reference

File Subroutines:

- subroutine TRANSFINITE

Quaternions.f90 File Reference

File Subroutines:

- subroutine Init_Quatern
- subroutine MultiQuatern
- subroutine DerivQuatern
- subroutine ConvertQuatern
- subroutine TOb_CardanYPR
- subroutine Convert_QuaTOcardanYPR

Radiation.f90 File Reference

File Subroutines:

- subroutine RADini
- subroutine InterpolKrad
- subroutine RadiationForce

READmeshinit.f90 File Reference

File Subroutines:

- subroutine READmeshinit

RK4.f90 File Reference

File Subroutines:

- subroutine Interp_RK4

Toolbox.f90 File Reference

File Subroutines:

- subroutine HEADER
- subroutine Initialisation
- subroutine Cross
- subroutine normale
- subroutine rotationPoint
- subroutine rotationNorm
- subroutine inttostr
- subroutine Inertia_Matrix

WB_Shaper.f90 File Reference

File Subroutines:

- subroutine WB_Shaper117th